

AD-784 144

A NUMERICAL METHOD FOR THE SIMULATION  
OF MUZZLE GAS FLOWS WITH FIXED AND  
MOVING BOUNDARIES

R. M. Traci, et al

Science Applications, Incorporated

Prepared for:

Army Ballistic Research Laboratories

June 1974

DISTRIBUTED BY:

**NTIS**

National Technical Information Service  
U. S. DEPARTMENT OF COMMERCE  
5285 Port Royal Road, Springfield Va. 22151

Destroy this report when it is no longer needed.  
Do not return it to the originator.

Secondary distribution of this report by originating  
or sponsoring activity is prohibited.

Additional copies of this report may be obtained  
from the National Technical Information Service,  
U.S. Department of Commerce, Springfield, Virginia  
22151.

ACCESSION for	
NTIS	White Section <input checked="" type="checkbox"/>
DDC	Ed. Section <input type="checkbox"/>
UNANNOUNCED	<input type="checkbox"/>
JUSTIFICATION	
BY	
DISTRIBUTION AVAILABILITY CODES	
Dist.	P. 811. 5-3 OF 8-10-61
A	

The findings in this report are not to be construed as  
an official Department of the Army position, unless  
so designated by other authorized documents.

*The use of trade names or manufacturers' names in this report  
does not constitute endorsement of any commercial product.*

UNCLASSIFIED

SECURITY CLASSIFICATION OF THIS PAGE (When Data Entered)

REPORT DOCUMENTATION PAGE		READ INSTRUCTIONS BEFORE COMPLETING FORM
1. REPORT NUMBER BRL CONTRACT REPORT NO. 161	2. GOVT ACCESSION NO.	3. RECIPIENT'S CATALOG NUMBER <b>AD-784144</b>
4. TITLE (and Subtitle) A NUMERICAL METHOD FOR THE SIMULATION OF MUZZLE GAS FLOWS WITH FIXED AND MOVING BOUNDARIES		5. TYPE OF REPORT & PERIOD COVERED Final 1 Jun 73 - 28 Feb 74
		6. PERFORMING ORG. REPORT NUMBER
7. AUTHOR(s) R.M. Traci, J. L. Farr, C. Y. Liu		8. CONTRACT OR GRANT NUMBER(s) DAAD05-73-C-0547
9. PERFORMING ORGANIZATION NAME AND ADDRESS Science Applications, Inc. 101 Continental Bldg., Suite 301 El Segundo, California 90245		10. PROGRAM ELEMENT, PROJECT, TASK AREA & WORK UNIT NUMBERS 62604A 1J562604A607
11. CONTROLLING OFFICE NAME AND ADDRESS U.S. Army Ballistic Research Laboratories Aberdeen Proving Ground, Maryland 21005		12. REPORT DATE June 1974
		13. NUMBER OF PAGES - 106
14. MONITORING AGENCY NAME & ADDRESS (if different from Controlling Office)		15. SECURITY CLASS. (of this report) UNCLASSIFIED
		15a. DECLASSIFICATION/DOWNGRADING SCHEDULE
16. DISTRIBUTION STATEMENT (of this Report)  Approved for public release; distribution unlimited.		
17. DISTRIBUTION STATEMENT (of the abstract entered in Block 20, if different from Report)		
18. SUPPLEMENTARY NOTES		
19. KEY WORDS (Continue on reverse side if necessary and identify by block number) Muzzle Gas Flow Unsteady Gas Dynamics Numerical Analysis  K. produced by NATIONAL TECHNICAL INFORMATION SERVICE U.S. Department of Commerce Springfield, VA 22151		
20. ABSTRACT (Continue on reverse side if necessary and identify by block number) A numerical technique for the simulation of the time dependent, axisymmetric flow of muzzle gases exiting a gun barrel with the attendant flow of ambient air is described. The technique is based on modifications to the OIL Eulerian hydrodynamics computer program to include treatment of arbitrary fixed and moving solid boundaries. This capability permits the inclusion of complex muzzle device geometry and a moving projectile in the Eulerian finite difference mesh.		

DD FORM 1473  
1 JAN 73

EDITION OF 1 NOV 65 IS OBSOLETE

UNCLASSIFIED

SECURITY CLASSIFICATION OF THIS PAGE (When Data Entered)

UNCLASSIFIED

SECURITY CLASSIFICATION OF THIS PAGE(When Data Entered)

20. The computer program generated during the study is called SAMS (Small Arms Muzzle Simulator). Calculations, performed with the program, are presented for a blunt projectile impulsively started from rest, and for M-16 muzzle gas flowfields. The muzzle blast calculations demonstrate the capability for calculating the complex interaction of the muzzle gases with a moving projectile and fixed boundaries. Computer generated plots are presented which show details of the expansion of the muzzle gases, generation of advancing shock wave in ambient air, blunt body shock in front of projectile and interaction of muzzle gases and air shock with the projectile.

ia

UNCLASSIFIED

SECURITY CLASSIFICATION OF THIS PAGE(When Data Entered)

## FOREWORD

The computer program development study described in this report was performed by the Los Angeles Division of Science Applications, Inc. for the U. S. Army Ballistic Research Laboratory under Contract DAAD05-73-C-0547 entitled, "Small Arms Muzzle Gas Flow Simulation."

R. M. Traci was the principal investigator for the study and J. L. Farr contributed to the development of the numerical solution method and performed the computer program modifications. Consultant C. Y. Liu contributed to the development of the numerical technique, and Consultant W. E. Johnson aided in computer program modifications. The BRL technical monitor for the study was C. K. Zoltani.

## TABLE OF CONTENTS

	<u>Page</u>
1.0 INTRODUCTION	1
2.0 DESCRIPTION OF MUZZLE BLAST FLOWFIELD	4
3.0 NUMERICAL SOLUTION METHOD	7
3.1 Conservation Equations for Inviscid, Compressible Fluid Mechanics and Solution Methodology	7
3.2 Fluid-in-Cell Finite Difference Approximation	10
3.3 Treatment of Irregular Solid Boundaries	17
3.3.1 Fixed Boundaries	17
3.3.2 Arbitrary Moving Boundaries	24
3.4 Stability and Accuracy Consideration	29
4.0 SPECIFICS OF METHOD FOR MUZZLE BLAST PROBLEM	32
4.1 Equation of State	32
4.2 Muzzle Flow and Farfield Boundary Conditions	33
4.3 Dynamics of Projectile Motion	36
5.0 TEST CASE RESULTS	38
5.1 Blunt Projectile Impulsively Started from Rest	38
5.2 M-16 Muzzle Blast Flowfield	46
5.3 M-16 with Muzzle Device	64

	<u>Page</u>
6.0 CONCLUSIONS AND RECOMMENDATIONS	81
7.0 REFERENCES	83
APPENDIX A: GEOMETRICAL DESCRIPTION OF PARTIAL CELLS	85
APPENDIX B: M-16 MUZZLE FLOW TIME HISTORIES	93
DISTRIBUTION LIST	95

## LIST OF FIGURES

	<u>Page</u>
FIGURE 1. SCHEMATIC OF MUZZLE BLAST FLOWFIELD	4
FIGURE 2. SCHEMATIC OF LOCAL CELL STRUCTURE	11
FIGURE 3. NUMBERING SYSTEM FOR CELL BOUNDARIES	13
FIGURE 4. SCHEMATIC OF BOUNDARY CELLS	19
FIGURE 5. PARTIAL CELLS FOR A GENERAL CURVED SURFACE	20
FIGURE 6. SCHEMATIC OF MOVING SOLID BOUNDARY	25
FIGURE 7. SCHEMATIC OF NUMERICAL SOLUTION DOMAIN	34
FIGURE 8. SCHEMATIC OF CYLINDRICAL PROJECTILE ACCELERATED IMPULSIVELY TO 1500 M/SEC	39
FIGURE 9. STAGNATION PRESSURE vs TIME	42
FIGURE 10. STAGNATION TEMPERATURE vs TIME	43
FIGURE 11. STAGNATION DENSITY vs TIME	44
FIGURE 12. COMPARISON OF THEORETICAL TO NUMERICAL RESULTS FOR RADIAL VELOCITY ON FRONT FACE OF BODY	45
FIGURE 13. SCHEMATIC OF M-16 MUZZLE BLAST CALCULATION	46



	<u>Page</u>
FIGURE 14. VELOCITY VECTOR PLOT: M-16 RIFLE	50
FIGURE 15. VELOCITY VECTOR PLOT: M-16 RIFLE	51
FIGURE 16. VELOCITY VECTOR PLOT: M-16 RIFLE	52
FIGURE 17. VELOCITY VECTOR PLOT: M-16 RIFLE	53
FIGURE 18. VELOCITY VECTOR PLOT: M-16 RIFLE	54
FIGURE 19. PRESSURE CONTOUR PLOT: M-16 RIFLE	55
FIGURE 20. PRESSURE CONTOUR PLOT: M-16 RIFLE	56
FIGURE 21. PRESSURE CONTOUR PLOT: M-16 RIFLE	57
FIGURE 22. PRESSURE CONTOUR PLOT: M-16 RIFLE	58
FIGURE 23. PRESSURE CONTOUR PLOT: M-16 RIFLE	59
FIGURE 24. DENSITY CONTOUR PLOT: M-16 RIFLE	60
FIGURE 25. TEMPERATURE CONTOUR PLOT: M-16 RIFLE	61
FIGURE 26. DENSITY CONTOUR PLOT: M-16 RIFLE	62
FIGURE 27. TEMPERATURE CONTOUR PLOT: M-16 RIFLE	63
FIGURE 28. SCHEMATIC OF M-16 WITH MUZZLE DEVICE	64
FIGURE 29. VELOCITY VECTOR PLOT: M-16 WITH MUZZLE DEVICE	67

		<u>Page</u>
FIGURE 30.	VELOCITY VECTOR PLOT: M-16 WITH MUZZLE DEVICE	68
FIGURE 31.	VELOCITY VECTOR PLOT: M-16 WITH MUZZLE DEVICE	69
FIGURE 32.	VELOCITY VECTOR PLOT: M-16 WITH MUZZLE DEVICE	70
FIGURE 33.	VELOCITY VECTOR PLOT: M-16 WITH MUZZLE DEVICE	71
FIGURE 34.	PRESSURE CONTOUR PLOT: M-16 WITH MUZZLE DEVICE	72
FIGURE 35.	PRESSURE CONTOUR PLOT: M-16 WITH MUZZLE DEVICE	73
FIGURE 36.	PRESSURE CONTOUR PLOT: M-16 WITH MUZZLE DEVICE	74
FIGURE 37.	PRESSURE CONTOUR PLOT: M-16 WITH MUZZLE DEVICE	75
FIGURE 38.	PRESSURE CONTOUR PLOT: M-16 WITH MUZZLE DEVICE	76
FIGURE 39.	DENSITY CONTOUR PLOT: M-16 WITH MUZZLE DEVICE	77
FIGURE 40.	TEMPERATURE CONTOUR PLOT: M-16 WITH MUZZLE DEVICE	78
FIGURE 41.	DENSITY CONTOUR PLOT: M-16 WITH MUZZLE DEVICE	79

	<u>Page</u>
FIGURE 42. TEMPERATURE CONTOUR PLOT: M-16 WITH MUZZLE DEVICE	80
FIGURE A.1. SCHEMATIC OF PARTIAL CELL	85
FIGURE A.2. INDEXING OF PARTIAL CELL BOUNDARY POINTS	86
FIGURE A.3. DEFINITION OF CELL INTERSECTION	87
FIGURE A.4. DEFINITION OF NORMAL TO SOLID SURFACE	90

#### LIST OF TABLES

	<u>Page</u>
TABLE A.1. COMPUTATION OF CELL INTERSECTIONS	91
TABLE A.2. COMPUTATION OF PARTIAL CELL PARAMETERS	92

## NOMENCLATURE

$a$		= Sound speed
$A, \hat{A}$		= Fractional area of cell side
$B, \tilde{B}$		= Representation of general flow quantity
$E$		= Specific total energy
$F$		= Fraction of cell volume
$I, \tilde{I}$		= Specific internal energy
$IB, IIN, JB$		= Grid locations of muzzle exit
$IMAX, JMAX$		= Maximum radial, axial grid lines
$i, j, k$		= Finite difference cell indices
$P$		= Pressure
$M, M_P$		= Increment in mass across cell sides, projectile mass
$\hat{n}$		= Unit normal vector
$N$		= Normal coordinate
$r, z$		= Radial and axial coordinates
$S$		= Surface area
$T$		= Tangential coordinate
$u, \tilde{u}, U, \tilde{U}, \bar{u}$		= Radial velocities
$v, \tilde{v}, V, \bar{v}$		= Axial velocities
$V$		= Volume
$V_P$		= Projectile axial velocity
$\beta$		= Covolume
$\Delta$		= Increment in length, time, etc.

$\epsilon$	=	Truncation error or unit vector
$\gamma$	=	Ratio of specific heats
$\rho$	=	Density
$\theta'$	=	Angle of normal to solid boundary

### Subscripts

$i, j, k$	Refer to finite difference cell
$M$	Refers to muzzle exit flow properties
$P$	Refers to projectile
$q$	Refers to beads defining solid boundary

### Superscripts

$n$	Refers to time level $t^n$
-----	----------------------------

## 1.0 INTRODUCTION

In this report, a numerical technique is described for simulating the time dependent, axisymmetric flow of muzzle gases exiting a gun barrel. The transient projectile boundary is included in the flowfield in a dynamically coupled manner and the attendant motion of ambient air, due to projectile motion and muzzle jet expansion, is described. The present technique is based on a generalization of the fluid-in-cell differencing technique of Rich<sup>1</sup> as incorporated in the OIL code developed by Johnson<sup>2</sup>. The modifications include a method for treating arbitrary fixed and moving solid boundaries within the Eulerian finite difference grid. The method is developed in general for application to solid boundaries moving or deforming in an arbitrary manner but is specifically applied in this study to treat the rigid body motion of a projectile exiting a gun barrel. This is consistent with the goal of the study, which was to develop a computational tool for those interested in studying the muzzle gas flow through complex muzzle devices. The computer program generated during the study is called SAMS (Small Arms Muzzle Simulator) and it is described in detail in a separate users manual<sup>3</sup>.

Transitional ballistics is concerned with the flow of muzzle gases through a muzzle device and the interaction of that flow with the projectile. The description of this flow regime has become more important with the trend in modern gun design to higher muzzle velocities, more powerful shell loadings and shorter barrels. The muzzle device, needed to reduce recoil, flash, noise or projectile dispersion, has become an integral part of weapon design. The complete description of muzzle gas flow through a muzzle device of complex geometry requires the solution of the partial differential equations of unsteady gas dynamics with transient boundaries. The flowfield is complicated by a wealth of fluid mechanical phenomena including shocks, contact surfaces, jets and nonequilibrium flow. Because of this inherent complexity, numerical solution techniques are clearly indicated.

Many finite difference techniques have been developed for the solution of fluid dynamics problems<sup>4,5</sup>, which use different approaches to the finite difference approximation of the fluid conservation equations. The techniques are all characterized by forward differencing in time and are loosely termed time dependent methods and nearly all

fall into one of two basic categories, depending upon whether they are written in terms of Lagrangian or Eulerian coordinates. In Lagrangian methods, the finite difference grid moves with the fluid, becoming distorted as the unsteady flowfield develops. These methods have been successfully applied to fluid mechanics problems in which the fluid does not become excessively distorted such as the interior ballistics problem and shock tube problems. The advantage of the approach is that fluid interfaces and contact surfaces can be accurately defined. The great disadvantage is that if the fluid is distorted such as in jets, shear layers or vortices, the finite difference grid requires almost continuous rezoning to keep it from literally tying itself into knots. In Eulerian methods, the finite difference grid is fixed in the solution space, and the fluid essentially flows through the grid. The advantage of this approach is that all manner of fluid mechanical phenomena can be treated without difficulty. The calculations are stable through large deformations and are typically quite efficient in terms of computer time requirements. The basic disadvantage of this method is that the regions of the solution which require high density zoning for accuracy are not always known a priori and in fact may change with time.

The muzzle blast problem, as formulated in this study, has elements of both Lagrangian and Eulerian characteristics. For example, the flow out of the muzzle device is best treated in a coordinate system fixed to the muzzle whereas a detailed description of the flow around the projectile requires coordinates moving with the projectile. Thus both Lagrangian and Eulerian approaches would require some degree of modification for application to the muzzle blast problem. A recent development in numerical techniques, which is worth mentioning in this regard, combines the features of both techniques and is known as the Arbitrary-Lagrangian-Eulerian (ALE) technique<sup>6,7</sup>. In this method, the finite difference mesh may move with the fluid, be held fixed, or move in any other prescribed way. The value of such a capability for application to the muzzle blast problem with both fixed and moving boundaries is clear.

Although each of the above techniques could in principle be applied to the muzzle blast problem, the approach used in this study is to modify an Eulerian technique to account for the motion of solid boundaries within the finite difference grid. The basic technique is embodied in OIL code which can be described as a continuous

fluid Eulerian code. It is written in fixed Eulerian (rectangular or axisymmetric) coordinates and uses a fluid-in-cell differencing technique. This technique is a generalization of the successful particle-in-cell technique, which provides for continuous fluid transport across cell boundaries. The differencing method is classified as a control volume approach<sup>4</sup> and conserves mass, momentum and energy within the solution space.

In the present study, the OIL code is modified to permit the calculation of flows about arbitrary fixed or moving solid boundaries. Such calculations require the treatment of "partial cells" which result when general solid boundaries are introduced in the rectangular finite difference grid. The treatment of partial cells is based on a method proposed by Rich<sup>1</sup> and implemented for fixed boundaries by Gentry, Martin and Daly<sup>6</sup>. The method presented herein, is a further extension of the formulation to account for arbitrary motion of the boundary. As applied to the muzzle blast problem the method thus provides for the prescription of a muzzle boundary of rather general shape as well as moving projectile boundary.

Although the numerical method has general application to flows about fixed or moving boundaries, its application in this study is directed at the muzzle blast problem. Thus the computer program developed during the study is tailored specifically for this problem. This is consistent with the goal of the study which was to develop a computational tool that is relatively easy to utilize in the muzzle design process. Thus particular emphasis was placed on the ease with which a problem could be set up and on stable and efficient operation.

Details of the numerical method and its application to the muzzle blast problem are given in the following sections. A brief description of the muzzle blast flowfield and the resulting requirements placed on the numerical technique is given in Section 2.0. In Section 3.0, a detailed description of the numerical method, including comment on stability and accuracy considerations, is presented. In Section 4.0 the specifics of the method for the muzzle blast problem are described and Section 5.0 presents calculated results. Finally, conclusions and recommendations are presented in Section 6.0.



## 2.0 DESCRIPTION OF MUZZLE BLAST FLOWFIELD

As noted in the introduction, the muzzle blast flowfield is a complex, inherently unsteady and multi-dimensional flowfield which includes numerous fluid mechanical phenomena. The problem provides a severe test of any numerical simulation technique, due to the wide range of flow conditions which exist as the transient flowfield develops. The detailed simulation of the problem would, however, considerably aid attempts to alleviate undesirable weapon characteristics such as recoil, noise, flash and projectile dispersion. Devices to suppress such characteristics are termed muzzle devices and have been designed almost exclusively by trial and error experimental programs. By way of introduction to the numerical technique and test cases presented in subsequent sections, some background on muzzle gas flow problems is presented in this section. This section includes a qualitative description of the transient flowfield and some insight into the phenomena of interest.

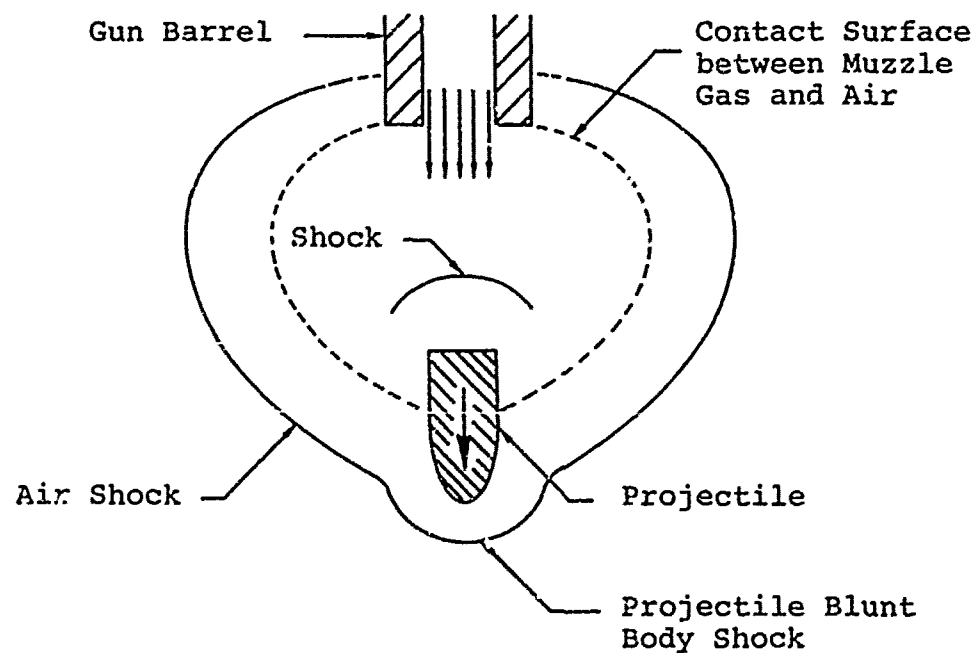


FIGURE 1. SCHEMATIC OF MUZZLE BLAST FLOWFIELD

A schematic description of the muzzle blast flow-field is given in Figure 1 above.

The muzzle gases, which accelerate the projectile down the barrel, consist of the high temperature ( $\sim 2500^{\circ}\text{K}$ ) and pressure ( $\sim 500$  atm) products of propellant combustion. As the projectile leaves the muzzle these gases are permitted to vent to the surrounding air, thus initiating a complex sequence of events which equilibrate the muzzle gas properties with the ambient. The presence of the high pressure jet of muzzle gas is communicated to the ambient by an outward rushing shock wave which outruns the projectile but decays rapidly in intensity and velocity. This weakening "blast wave" is the source of much of the far-field sound resulting from the firing sequence. In the meantime, the muzzle gases continue to expand and accelerate into the shock processed air between the projectile and barrel, and around the projectile. It is clear that while the projectile is in, or in close proximity to, the muzzle device, the moving projectile boundary will have an important effect on the flow in the device. In fact, the projectile is the obstruction which causes the muzzle gas to expand radially if permitted by muzzle geometry. The jet of muzzle gases expands around the projectile, so that the projectile is initially flying backwards relative to the muzzle gases. Thus the projectile is still accelerating relative to the barrel, but the muzzle gases begin to decelerate so that the projectile then penetrates, in turn, the gas cloud and the shock wave as it proceeds on to the target. The scenario described above all happens on a time scale of the order of 100 microseconds.

Various muzzle devices are used to tailor the muzzle gas flow. Recoil forces can be significantly decreased by venting the muzzle gases radially away from the barrel before the projectile exists. The tendency of a weapon to climb can be reduced at the same time by directing the muzzle gases upward. It is also believed that projectile dispersion can be reduced somewhat by tailoring the geometry of the flow deflector. As noted above, the projectile is initially flying in an unstable attitude (backwards) through the muzzle gas cloud. Deflecting the flow away from the axis would decrease the flow density and velocity through which the projectile is passing, thereby decreasing the intensity and duration of the unstable forces on the projectile. This could be especially important for multiple flechette projectiles which are considerably less stable in a reverse flow than normal projectiles.

Other undesirable characteristics of the muzzle flow are noise and muzzle flash. A source of noise other than the initial air shock wave and the supersonic projectile shock system ("ballistic crack") are the fluctuations in the shear layers of the muzzle jet as it exits the muzzle. Muzzle geometry can significantly affect the nature (intensity and directionality) of such sources of farfield noise by decreasing the magnitude of flow pressure and velocity before the gas is vented from the device. Muzzle flash is caused by the high temperature, nonequilibrium nature of the gas as it exits the muzzle. Again muzzle geometry can be chosen so as to expand the gas to a temperature below propellant ignition temperature before permitting it to exit from the device. One method to accomplish this would be to define the device geometry in such a way that cool ambient air is entrained by the jet of muzzle gases.

All of the undesirable weapon characteristics mentioned above are strongly dependent upon muzzle device geometry. To be useful in any systematic study of devices to reduce or eliminate such characteristics, a numerical simulation technique must necessarily account for complex muzzle geometry and a moving projectile boundary. Projectile geometry could also be important to the dispersion caused by the flow of muzzle gases over the projectile and could be studied in the same manner. The numerical technique and computer program developed in the present study thus emphasize geometry considerations to facilitate such studies.

The numerical technique for simulating the complex flowfield described above must be stable through wide variations in flow velocity from supersonic to stagnation and in flow densities from many times ambient in the muzzle jet to considerably below ambient in the expansion following the air shock. This coupled with the need for defining complex muzzle geometry indicated that an Eulerian differencing technique would be most appropriate. The development of the technique used in this study is given in the following sections.

### 3.0 NUMERICAL SOLUTION METHOD

The main complexity in the numerical calculation of muzzle blast flowfields, described above, involves the treatment of the irregular solid boundaries defining the muzzle device and moving projectile. The importance of the computational treatment of boundary conditions in any finite difference technique cannot be overstated, as the treatment can affect not only the accuracy but the stability of the numerical technique<sup>4</sup>. Thus the main thrust of the present effort, and its primary accomplishment, is in the area of a finite difference approximation to irregular fixed and moving solid boundaries. The numerical technique is described in detail in this section.

Sections 3.1 and 3.2 below summarize the relevant conservation equations and the fluid-in-cell differencing technique used in the OIL program. Modifications for fixed and moving solid boundaries are given in Section 3.3 and a discussion of the stability and accuracy of the overall numerical technique is presented in Section 3.4.

#### 3.1 Conservation Equations for Inviscid, Compressible Fluid Mechanics and Solution Methodology

In the treatment of the muzzle blast problem in this report, the flowfield generated by the muzzle gases is considered within the context of inviscid, unsteady gas dynamics of a single fluid with real gas equation of state. Assuming axisymmetric flow, the governing differential equations are written in cylindrical (r, z) coordinates as:

$$\frac{\partial \rho}{\partial t} + \frac{1}{r} \frac{\partial (\rho u r)}{\partial r} + \frac{\partial (\rho v)}{\partial z} = 0 \quad (1)$$

$$\frac{\partial u}{\partial t} + u \frac{\partial u}{\partial r} + v \frac{\partial u}{\partial z} = - \frac{1}{\rho} \frac{\partial P}{\partial z} \quad (2)$$

$$\frac{\partial v}{\partial t} + u \frac{\partial v}{\partial r} + v \frac{\partial v}{\partial z} = - \frac{1}{\rho} \frac{\partial P}{\partial z}$$

$$\frac{\partial E}{\partial t} + u \frac{\partial E}{\partial r} + v \frac{\partial E}{\partial z} = - \frac{1}{\rho} \left\{ \frac{1}{r} \frac{\partial (rPu)}{\partial r} + \frac{\partial (Pv)}{\partial z} \right\} \quad (3)$$

where  $\rho$ ,  $P$ ,  $E$  are the fluid density, pressure and total energy respectively and  $u$ ,  $v$  are the velocity components in the radial,  $r$ , and axial,  $z$ , coordinate directions respectively, and  $t$  is time. The total energy of the fluid is defined in the usual manner:

$$E = \frac{1}{2}(u^2+v^2) + I \quad (4)$$

where  $I$  is the specific internal energy. To effectively close the above system of equations, a fluid equation of state is appended to define the pressure as:

$$P = P(\rho, I) \quad (5)$$

As noted earlier, the fluid-in-cell differencing technique for approximating the above equations uses a control volume approach, so that it is useful in describing the solution method to refer to the control volume form of the conservation equations which are written as

$$\frac{\partial}{\partial t} \int_V \rho dV = - \int_S \rho \vec{u} \cdot \hat{n} dS \quad (6)$$

$$\frac{\partial}{\partial t} \int_V \rho u dV = - \int_S \rho \vec{u} (\vec{u} \cdot \hat{n}) dS - \int_S P \hat{n} dS \quad (7)$$

$$\frac{\partial}{\partial t} \int_V \rho E dV = - \int_S \rho E (\vec{u} \cdot \hat{n}) dS - \int_S P (\vec{u} \cdot \hat{n}) dS \quad (8)$$

where  $V$  is an arbitrary volume in the fluid with surface area  $S$  and  $\hat{n}$  is the unit outward normal on the surface.

In the finite difference approximation to the conservation equations, presented in the next section, the integration volumes are the cells of the finite difference mesh. The control volume equations are thus helpful in understanding the treatment of the transport or convective terms in the numerical technique.

The method for solving the above system of equations is briefly summarized here by way of introduction to the finite difference approximations presented in the next section. The calculations necessary to advance the solutions one step in time,  $\Delta t$ , are separated into two distinct phases. The first phase consists of an explicit Lagrangian calculation for a fluid particle defined by a computational cell in which fluid properties ( $\rho$ ,  $u$ ,  $v$ ,  $E$ ) are assumed uniform. Neglecting convection terms, the axisymmetric form of the conservation equations are:

$$\frac{\partial u}{\partial t} = - \frac{1}{\rho} \frac{\partial P}{\partial r} \quad (9)$$

$$\frac{\partial v}{\partial t} = - \frac{1}{\rho} \frac{\partial P}{\partial z} \quad (10)$$

$$\frac{\partial E}{\partial t} = - \frac{1}{\rho} \left\{ \frac{1}{r} \frac{\partial (rP^2)}{\partial r} + \frac{\partial (Pv)}{\partial z} \right\} \quad (11)$$

An alternate form of the energy equation which is used is:

$$\frac{\partial I}{\partial t} = - \frac{P}{\rho} \left\{ \frac{\partial v}{\partial z} + \frac{1}{r} \frac{\partial (ru)}{\partial r} \right\} \quad (12)$$

These equations are used in phase one to update  $u$ ,  $v$ , and  $I$  to an intermediate state. At this stage in a Lagrangian technique the grid points defining a finite difference

cell (or fluid particle) would be moved to their advanced time positions and new cell densities would be calculated. In an Eulerian method as used here, however, the grid points remain fixed in space so that the transport terms must be accounted for. Thus in phase two of the calculation, mass, momentum and energy are transported across the fixed, cell boundaries thereby completing the process of updating flow quantities to time  $t + \Delta t$ . The control volume form of the conservation equations, neglecting pressure terms which were accounted for in phase one, is most appropriate in this phase. Each cell is considered as a control volume and transport to or from adjacent cells is accounted for. In some sense, this phase is equivalent to rezoning the Lagrangian cells, or in other words moving the Lagrangian cell boundaries back to their positions at the beginning of the cycle. This is used to advantage in the arbitrary Lagrangian-Eulerian technique, in which cell boundaries are moved in a general manner.

The separation of the computational cycle into a Lagrangian phase and a convective or rezone phase originated in the particle-in-cell numerical method<sup>9</sup>, and has been used in many hydrodynamic computer codes, besides the OIL code. The rationale behind the separation into phases is basically that the equations of motion are inherently Lagrangian and are quite straightforward extension of Newtonian dynamics to a continuum. The technique thus separates the physics of the problem from the mathematical complexity of the transformation to Eulerian coordinates. In addition to this conceptual simplification, the separation of Lagrangian effects from transport effects has the important benefit of permitting a finite difference scheme which "globally" conserves mass, momentum, and energy. For example, energy is conserved throughout the finite difference grid as a result of this separation into phases plus the proper choice of time centering in the Lagrangian phase. The finite difference approximation to the conservation equations used in each cycle are now summarized in the next section.

### 3.2 Fluid-in-Cell Finite Difference Approximation

The fluid-in-cell differencing technique, used in the OIL program, is described in detail by Rich<sup>1</sup>, Gentry, et al.<sup>8</sup>, and Johnson<sup>2</sup>. The finite difference forms used in the method are summarized in this section and the reader is referred to the above references for a more detailed description.

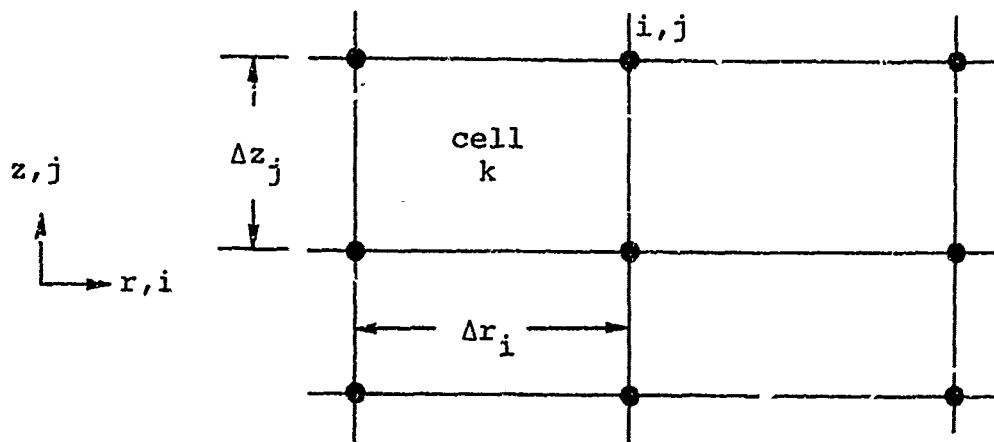


FIGURE 2. SCHEMATIC OF LOCAL CELL STRUCTURE

In the finite difference approximation to the continuum conservation equations, the region of fluid under consideration is covered by a fixed grid of rectangular cells with cell indices and mesh spacing as indicated in Figure 2. The index  $k$  is related in a straightforward manner to  $i$  and  $j$  and denotes the cell number. Arbitrary cell-spacing, in both  $r$  (radius) and  $z$  (axial) directions, is used to permit concentration of cells in regions of the flow in which a high degree of resolution is desired. For the purposes of differencing, all flow quantities ( $\rho, P, I, u, v$ ) are defined at cell centers. An unsteady calculation is initiated by defining flow properties in each cell at an initial time  $t = 0$ . The flow quantities are then updated in a cyclic manner to later times using the finite difference analog to the fluid conservation equations. Considering the fluid state at some time  $t$ , the equations used to update all fluid quantities to an advanced time  $t + \Delta t$  are now described.

It is recalled that the cycle begins with a pure Lagrangian calculation (phase one) in which the convective terms in the Eulerian form of the equations of motion are neglected. The differential form of the equations in the cylindrical coordinates of interest were given in the previous section for the two components of momentum ( $r, z$ ) (Equations 9 and 10, respectively) and for



internal energy (Equation 12). Time derivatives are approximated in the usual explicit form, for example:

$$\left(\frac{\partial u}{\partial t}\right)_{i,j} = \frac{\tilde{u}_{i,j} - u_{i,j}^n}{\Delta t} \quad (13)$$

A tilde ( $\sim$ ) on all flow quantities denotes the value at the end of phase one and superscript  $n$  denotes the value at time  $t$ . The pressure gradients are approximated by a leapfrog differencing scheme in which the pressure on cell boundaries is taken as the simple average of the pressure in the cell and its neighbor. The resulting finite difference equations for updating flow quantities in phase one are written as:

$$\tilde{u}_{i,j} = u_{i,j}^n + \frac{\Delta t}{\rho_{i,j}^n} \left\{ \frac{P_{i-1,j}^n - P_{i+1,j}^n}{2\Delta r_i} \right\} \quad (14)$$

$$\tilde{v}_{i,j} = v_{i,j}^n + \frac{\Delta t}{\rho_{i,j}^n} \left\{ \frac{P_{i,j-1}^n - P_{i,j+1}^n}{2\Delta z_j} \right\} \quad (15)$$

and

$$\tilde{I}_{i,j} = I_{i,j}^n - \frac{P_{i,j}^n \Delta t}{\rho_{i,j}^n} \left\{ \frac{\bar{v}_{i,j+1} - \bar{v}_{i,j-1}}{2\Delta z_j} \right. \\ \left. + \frac{1}{r_i} \left( \frac{\bar{u}_{i+1,j} r_{i+1} - \bar{u}_{i-1,j} r_{i-1}}{2\Delta r_i} \right) \right\} \quad (16)$$

where

$$\bar{u}_{i,j} = \frac{1}{2}(u_{i,j}^v + u_{i,j}^n)$$

(17)

$$\bar{v}_{i,j} = \frac{1}{2}(v_{i,j}^v + v_{i,j}^n)$$

The use of the average velocities  $\bar{u}$  and  $\bar{v}$  in the internal energy equation is required for energy conservation in the finite difference analog. Rich<sup>1</sup> gives a detailed explanation for their use which will not be repeated here. It is noted that density is not updated in phase one since the mass in a cell (fluid particle) is assumed constant in the Lagrangian sense.

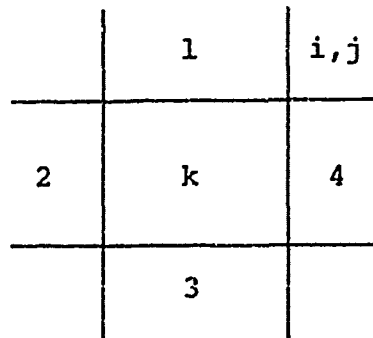


FIGURE 3. NUMBERING SYSTEM FOR CELL BOUNDARIES

The density and other flow properties are next updated to the advanced time  $t + \Delta t$  in phase two which accounts for the transport of mass, momentum and energy across cell boundaries, neglected in phase one. The numbering system for cell boundaries is given in Figure 3 and used in the following discussion. The control volume form of the conservation equations (Equations 6, 7 and 8) is applied to each cell and flow of mass, momentum and energy across cell boundaries is accounted for. The finite difference approximation to the continuity equation is:

$$\rho_{i,j}^{n+1} = \rho_{i,j}^n + \frac{1}{V_{i,j}} \left\{ -\Delta M_1^n + \Delta M_2^n + \Delta M_3^n - \Delta M_4^n \right\} \quad (18)$$

where  $V_{i,j}$  is the cell volume and  $\Delta M_i$  is the increment in mass which flows across cell side  $i$  during the time  $\Delta t$ . The mass flow across side 2, for example, is approximated using donor cell differencing by:

$$\Delta M_2^n = \begin{cases} 2\pi r_{i-1} \Delta z_j \rho_{i-1,j}^n \bar{U}_2 \Delta t, & \text{for } \frac{\tilde{u}_{i-1,j} + \tilde{u}_{i,j}}{2} > 0 \\ 2\pi r_{i-1} \Delta z_j \rho_{i,j}^n \bar{U}_2 \Delta t, & \text{for } \frac{\tilde{u}_{i-1,j} + \tilde{u}_{i,j}}{2} < 0 \end{cases} \quad (19)$$

It is noted that the density, in this expression, is taken as the value in the donor cell and that  $\bar{U}_2$  is a weighted velocity for fluid flowing from the donor cell. This velocity is determined by a Taylor series expansion about the cell boundary, assuming that the fluid moves a distance  $\Delta = \bar{U}_2 \Delta t$  in the time increment  $\Delta t$ . The expansion is:

$$\bar{U}_2 = \frac{1}{2}(\tilde{u}_{i,j} + \tilde{u}_{i-1,j}) + \Delta \left( \frac{\tilde{u}_{i,j} - \tilde{u}_{i-1,j}}{\Delta r_{i-1}} \right) + \dots$$

where

$$\Delta = \bar{U}_2 \Delta t$$

Solving this expression for  $\tilde{u}_2$  gives:

$$\tilde{u}_2 = \frac{1}{2} \frac{\tilde{u}_{i,j} + \tilde{u}_{i-1,j}}{(\tilde{u}_{i,j} - \tilde{u}_{i-1,j}) \frac{\Delta t}{\Delta r_{i-1}} + 1} \quad (20)$$

The use of this weighted velocity (of which Equation 20 is just one of many approximations that could be used) is an essential ingredient to the donor cell differencing scheme and has been found by Rich<sup>1</sup> to have superior diffusive properties.

The increments in mass flow on the other sides of the cell are determined in an equivalent manner.

Transport of momentum and total energy are treated in the same way and the result is:

$$B_{i,j}^{n+1} = B_{i,j}^n + \frac{1}{\rho_{i,j}^{n+1} v_{i,j}} \left\{ -B_1 \Delta M_1^n + B_2 \Delta M_2^n + B_3 \Delta M_3^n - B_4 \Delta M_4^n \right\} \quad (21)$$

where B denotes u, v or E. It is noted that the  $B_i$  ( $i = 1, 2, 3, 4$ ) are also determined by the respective flow quantity in the donor cell. The process for updating all quantities to an advanced time ( $t + \Delta t$ ) is completed by calculating the specific internal energy and pressure in each cell as follows:

$$I_{i,j}^{n+1} = E_{i,j}^{n+1} - \frac{1}{2} (u^2 + v^2)_{i,j}^{n+1} \quad (22)$$

and from the equation of state:

$$P_{i,j}^{n+1} = P(\rho_{i,j}^{n+1}, I_{i,j}^{n+1}) \quad (23)$$

The solution method described in this section has been determined by many years of numerical experimentation. Details of the approximations such as the donor cell (or upstream) differencing and the velocity weighting of mass flux across cell boundaries are found to be necessary to the stability and accuracy of the scheme. The scheme is conservative for the rectangular mesh systems used, as described by Rich<sup>1</sup> and Johnson<sup>2</sup>. The difference approximations used are first order accurate with regard to time increment and mesh spacing, and could be improved in a number of ways. However, the method described here has been used successfully, and with good comparison to experimental or alternate numerical results, on a wide range of fluid mechanics problems. The treatment of boundary conditions, essential to the muzzle blast problem, is described in the next section. This treatment is consistent with the basic scheme discussed here.

### 3.3 Treatment of Irregular Solid Boundaries

The main modification to the OIL code, made during this study, was to add the capability of defining fixed and moving boundaries of arbitrary shape within the finite difference solution field. This modification is of prime importance to the muzzle blast problem because of the professed desire of predicting the velocity and pressure field in and around the muzzle device and projectile. The treatment of boundary conditions is generally the most important and often the most difficult aspect of any numerical technique for fluid mechanics problems. The most accurate and straightforward treatment of solid boundaries is to use an orthogonal coordinate system which matches the boundary contour<sup>4</sup>. This would be impossible for the muzzle blast problem, however, due to the existence of closed contours (projectile or baffles, etc.) in the flowfield. The method described here is to overlay the boundary surface on the rectangular grid geometry. A special accounting is thus made of the "partial cells" on the boundary in terms of both their geometry and dynamic boundary condition. The method is based upon the work of Rich<sup>1</sup> for fixed boundaries (Section 3.3.1) and is generalized here to account for arbitrary boundary motion in Section 3.3.2.

#### 3.3.1 Fixed Boundaries

The OIL code is written for rectangular cell geometry with general grid spacing. It was originally developed for the calculation of hypervelocity impact and intense explosions, so that no provision is made for general boundaries in the grid. Later versions of the OIL code account for fluid interfaces within the grid<sup>10,11</sup>, permitting the calculation of multi-fluid problems. The treatment used for such interfaces is however inappropriate for the treatment of solid/fluid boundaries within the context of inviscid fluid mechanics. The physical boundary condition for inviscid flow (slip boundary condition) over a solid boundary is that the normal velocity of the fluid at the boundary equals the normal velocity of the boundary. For fixed boundaries this means that the flow velocity normal to the boundary must equal zero.

The difference equations given in the previous section are valid only for interior cells not on a boundary and must therefore be modified to account for the zero

normal velocity boundary condition. In the simple case in which the solid boundaries fall on grid lines the desired boundary condition can be obtained by the use of fictitious cells inside the solid boundary. For example, consider a cell (i,j) which is adjacent to a solid boundary which falls on the i grid line or right hand side of the cell. A fictitious cell (i+1,j) is used whose flow conditions are completely determined by the conditions in cell (i,j). That is, in the normal "reflective" boundary condition sense, the flow properties (density, pressure, internal energy) in the fictitious cell must be equal to the corresponding flow properties in cell (i,j) at all times. Also, the normal velocity (u in this example) in the cell (i+1,j) is the negative of the normal velocity in cell (i,j) and the tangential velocity (v) is at all times equal in both cells. Thus at the end of phase one set:

$$\rho_{i+1,j}^n = \rho_{i,j}^n, \quad \tilde{p}_{i+1,j} = \tilde{p}_{i,j}, \quad \tilde{y}_{i+1,j} = \tilde{y}_{i,j} \quad (24)$$

$$\tilde{u}_{i+1,j} = -\tilde{u}_{i,j}, \quad \tilde{v}_{i+1,j} = \tilde{v}_{i,j}$$

and at the end of phase two set:

$$\rho_{i+1,j}^{n+1} = \rho_{i,j}^{n+1}, \quad p_{i+1,j}^{n+1} = p_{i,j}^{n+1}, \quad \tilde{y}_{i+1,j}^{n+1} = \tilde{y}_{i,j}^{n+1} \quad (25)$$

$$u_{i+1,j}^{n+1} = -u_{i,j}^{n+1}, \quad v_{i+1,j}^{n+1} = v_{i,j}^{n+1}$$

Solid boundaries on other sides of the grid are treated in a similar manner. If the solid boundary has a corner, as shown in Figure 4 below, the properties of the fictitious cell (i+1,j) are assigned values depending upon whether the cell (i,j) or (i+1,j+1) is being considered. The above prescription essentially fixes the gradients

of all flow quantities equal to zero at the surface as well as setting the normal velocity equal to zero. In a mathematical sense this overdetermines the problem. It could be improved by extrapolating flow quantities to the boundary based on more cells than just the boundary cell but the method used here is consistent with the first order differencing scheme and hoped for increases in accuracy based on an extrapolation procedure are seldom realized in practice.

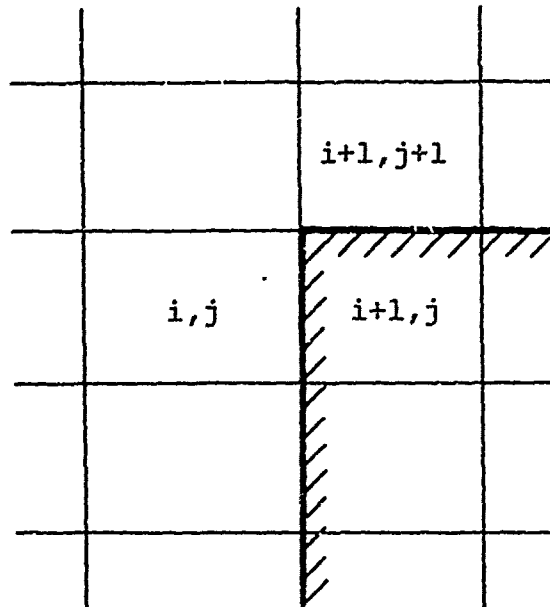


FIGURE 4. SCHEMATIC OF BOUNDARY CELLS

The method described above for solid boundaries on grid lines is used in the present study for defining the straight portion of the gun barrel "upstream" of the muzzle device. A more complicated method is required for a general body surface such as a muzzle device boundary. Consider a general curved surface, as shown in Figure 5, defined by a series of points ("beads") connected by straight line segments. The partial cells, generated by cuts across grid lines, are characterized by five quantities:  $F_{i,j}$ ,  $(A_1)_{i,j}$ ,  $(A_2)_{i,j}$ ,  $(A_3)_{i,j}$ ,  $(A_4)_{i,j}$ .  $F_{i,j}$  is the fractional volume of the partial cell and  $(A_k)_{i,j}$  ( $k = 1, 2, 3, 4$ ) are the fractional areas open to the flow for cell sides as denoted in Figure 5. These quantities are defined in a purely geometrical fashion based on bead



location and the local grid dimensions. The details of the method for defining partial cell geometry, for a general fixed or moving boundary, are given in Appendix A.

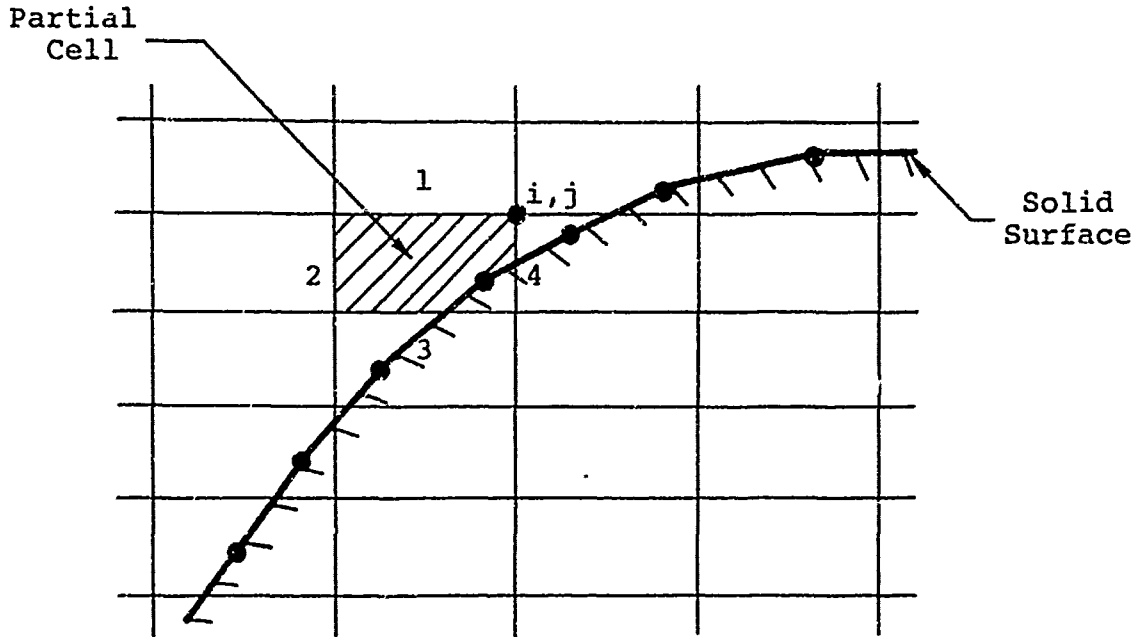


FIGURE 5. PARTIAL CELLS FOR A GENERAL CURVED SURFACE

The Lagrangian equations used in phase one to update  $u$ ,  $v$  and  $I$  are rewritten to take account of the geometry of the partial cells as follows:

$$\tilde{u}_{i,j} = u_{i,j}^n + \frac{\Delta t \hat{A}_{2-4}}{\rho_{i,j}^n F_{i,j}} \left\{ \frac{p_{i-1,j}^n - p_{i+1,j}^n}{2\Delta x_i} \right\} \quad (26)$$

$$\tilde{v}_{i,j} = v_{i,j}^n + \frac{\Delta t \hat{A}_{1-3}}{\rho_{i,j}^n F_{i,j}} \left\{ \frac{p_{i,j-1}^n - p_{i,j+1}^n}{2\Delta z_j} \right\} \quad (27)$$

and

$$\begin{aligned} \bar{I}_{i,j} = I_{i,j}^n - \frac{P_{i,j}^n \Delta t}{\rho_{i,j}^n F_{i,j}} \left\{ \hat{A}_{1-3} \left( \frac{\bar{v}_{i,j+1} - \bar{v}_{i,j-1}}{2\Delta z_j} \right) \right. \\ \left. + \frac{\hat{A}_{2-4}}{r_i} \left( \frac{\bar{u}_{i+1,j} r_{i+1} - \bar{u}_{i-1,j} r_{i-1}}{2\Delta r_i} \right) \right\} \end{aligned} \quad (28)$$

where

$$\hat{A}_{1-3} = \max [A_1, A_3]_{i,j} \quad (29)$$

$$\hat{A}_{2-4} = \max [A_2, A_4]_{i,j}$$

where the subscripts on the fractional areas refer to the cell sides as numbered in Figure 5 above, and  $\bar{u}$  and  $\bar{v}$  are as defined in the previous section. In general, the above equations refer to quantities in fictitious cells within the solid boundary. When this occurs the reflection principle described earlier, based on the cell under consideration, is used. That is, if a cell side is completely closed ( $A_i = 0$ ), the flow properties in the fictitious cell within the boundary are determined by the reflection principle. For example, if  $A_4 = 0$ , take:

$$\rho_{i+1,j} = \rho_{i,j}, \quad P_{i+1,j} = P_{i,j}, \quad I_{i+1,j} = I_{i,j} \quad (30)$$

$$u_{i+1,j} = -u_{i,j}, \quad v_{i+1,j} = v_{i,j}$$

Some comment is required on the degree of approximation of the partial cell geometry inherent in Equations (26) through (28). For simplicity, consider just the axial momentum equation. Using the Lagrangian form of the control volume momentum equations (Equation 7 with no transport terms), it can be shown that the axial momentum equation to first order can be written as:

$$\tilde{v}_{i,j} = v_{i,j}^n + \frac{\Delta t}{\rho_{i,j}^n F_{i,j} \Delta z_j} \left\{ A_3 \frac{(P_{i,j-1}^n + P_{i,j}^n)}{2} + (A_1 - A_3) P_S - A_1 \frac{(P_{i,j+1}^n + P_{i,j}^n)}{2} \right\}$$

where  $P_S$  is the fluid pressure along the solid boundary. Many approximations to  $P_S$  could be used which are accurate to the same order as the basic differencing scheme. Equation (27) results from the assumption that  $P_S$  equals the pressure on the cell side with minimum opening to the flow. This is the simplest approximation possible and in fact was used with some success by Rich<sup>1</sup>, which is the basic reason for using it in this study. Another possible approximation would be to assume that  $P_S = P_{i,j}$  in the normal reflective boundary condition sense. A potentially more accurate approximation would be to use the momentum equation normal to the solid surface with a one sided difference approximation for the pressure gradient normal to the wall, to determine  $P_S$ . Unfortunately these alternative techniques were not examined in the present study but will hopefully be the subject of future research.

As noted above, the finite difference approximations given here are just one of many alternative forms which are consistent with the first order accuracy of the general difference scheme. The approximation could be improved in a number of ways, one of which would be to extrapolate flow quantities into the fictitious boundary cells as mentioned earlier. A more important improvement would be to explicitly account for the shifting center of mass of the partial cells in the Lagrangian phase of the calculation. Improvements such as these would require extensive numerical experimentation to verify the hoped for increase in accuracy and were beyond the scope of this initial study.

The treatment of transport terms for partial cells in phase two of the calculation are a straightforward extension of the general expressions to account for the partial cell geometry. The partial cell equivalents of the mass, momentum and energy equations (Equations 18 and 21) in phase two are:

$$\rho_{i,j}^{n+1} = \rho_{i,j}^n + \frac{1}{F_{i,j} V_{i,j}} \left\{ - A_1 \Delta M_1^n + A_2 \Delta M_2^n \right. \\ \left. + A_3 \Delta M_3^n - A_4 \Delta M_4^n \right\} \quad (31)$$

and

$$B_{i,j}^{n+1} = B_{i,j}^n + \frac{1}{\rho_{i,j}^{n+1} F_{i,j} V_{i,j}} \left\{ - B_1 A_1 \Delta M_1^n + B_2 A_2 \Delta M_2^n \right. \\ \left. + B_3 A_3 \Delta M_3^n - B_4 A_4 \Delta M_4^n \right\} \quad (32)$$

where, as before, B denotes u, v or E,  $V_{i,j}$  is the rectangular cell volume and subscript k ( $k = 1, 2, 3, 4$ ) refers to the (i,j) cell sides as given in Figure 5. The mass transport, velocity weighting scheme and donor cell differencing scheme are the same as given in the previous section.

It is reiterated that the treatment of fixed boundaries described in this section is consistent with the

first order accuracy of the basic fluid-in-cell scheme. Improvements to the method, such as an accurate definition of boundary cell center of mass and interpolation on the center of mass to determine quantities on the cell boundaries will hopefully be considered in continued research on the method. It should be mentioned that the less exact method given here, however, is at least as accurate as the donor cell or upwind differencing required for stability of the method. Thus, it is not clear that such improvements would lead to a more accurate scheme.

### 3.3.2 Arbitrary Moving Boundaries

The treatment of moving boundaries within the Eulerian grid is the essential contribution of the present code development effort. This permits the inclusion of the projectile in the flowfield which, as noted earlier, is important to the overall development of the muzzle gas flow. The treatment given here is a generalization of that just given for fixed boundaries with provision for general time dependent motion of the boundary. Although the technique is developed for general motion, it is specialized where applicable for the rigid body motion of the projectile.

Consider a partial cell, occupied at a time  $t$  by a solid boundary which is moving in a general manner. The boundary motion is defined by the motion of a point  $q$   $[(U_q(t), V_q(t))]$  on its surface, as shown schematically in Figure 6. As in the case of the fixed boundaries, the moving boundary is defined by straight line segments joining a sequence of beads moving with its surface. The position of the beads in the finite difference grid  $[r_q(t), z_q(t)]$  at any instant determines the geometrical factors  $[F_{i,j}, A_i (i = 1, 2, 3, 4)]$  for the partial cells all along the solid boundary. Again the details of the calculation of these factors is given in Appendix A. The angle ( $\theta'$ ) of the local normal to the boundary is an additional factor, not used for fixed boundaries, but which is needed for the dynamics of moving boundaries. For present purposes, this angle is defined in an approximate manner as the angle between the  $z$  axis and the normal to the line segment joining the points at which the boundary cuts the cell sides, as shown in Figure 6.

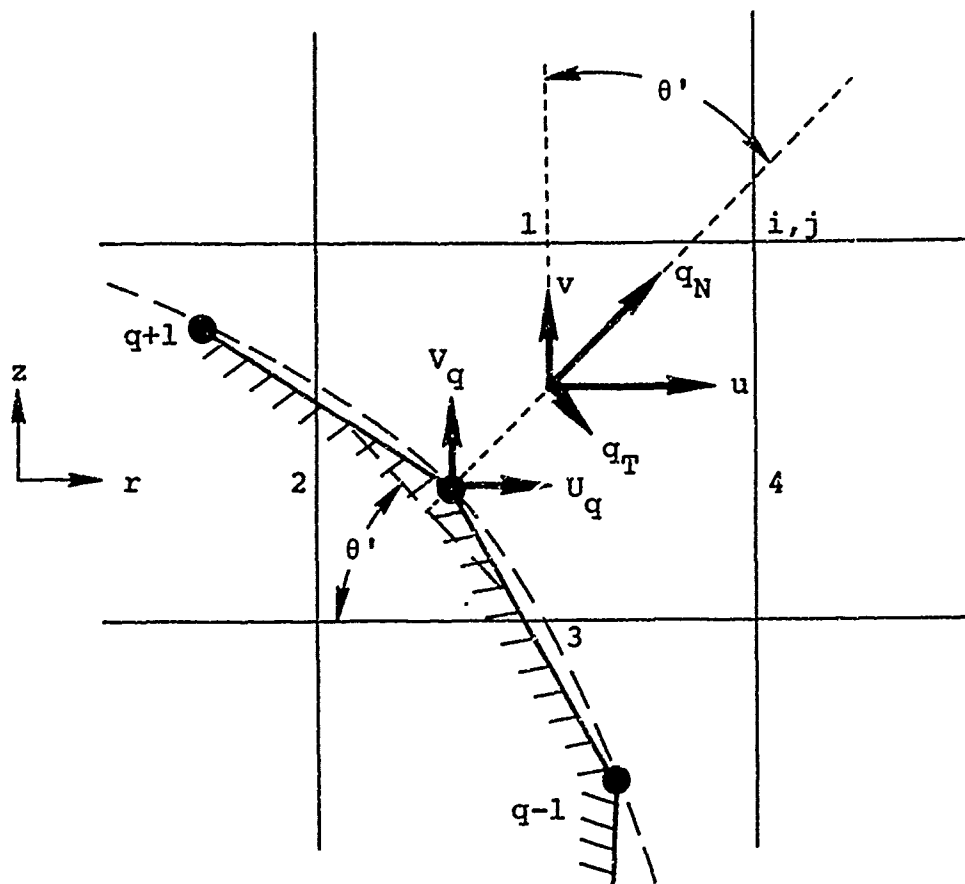


FIGURE 6. SCHEMATIC OF MOVING SOLID BOUNDARY

Within the framework of inviscid fluid mechanics, the normal velocity of the fluid at the boundary ( $q_N$ ) must equal the normal velocity of the boundary at any instant. The tangential fluid velocity, however, is free to slip with respect to the surface. The numerical treatment of the dynamics of the fluid in the partial cell must therefore account for this behavior. In the following discussion, a coordinate system fixed to the local normal and tangent line to the surface, as shown in Figure 6, is considered. It is recalled that in phase one of the fluid-in-cell differencing technique, the fluid within a computational cell is considered as a fluid particle and the Lagrangian equations of motion are solved. For coordinates normal to and tangent to the solid boundary these equations are given by:

$$\frac{\partial q_N}{\partial t} = - \frac{1}{\rho} \frac{\partial P}{\partial N}, \quad \frac{\partial q_T}{\partial t} = - \frac{1}{\rho} \frac{\partial P}{\partial T} \quad (33)$$

where N and T are the normal and tangential coordinates respectively.

The treatment for the partial cells on the moving boundary used here is to assume that the normal velocity of the fluid in the cell is equal to the normal velocity of the boundary or:

$$\left( \tilde{q}_N \right)_{i,j} = U_q^n \sin \theta'_{i,j} + V_q^n \cos \theta'_{i,j} \quad (34)$$

where  $i, j$  refers to the partial boundary cell,  $U_q, V_q$  (see Figure 6) are the velocity of the boundary bead at time  $t$  and the tilde ( $\tilde{\phantom{x}}$ ) refers to values at the intermediate state after phase one. It is noted that this is equivalent to prescribing the reflection boundary condition normal to the surface or:

$$\left( \frac{\partial P}{\partial N} \right)_{i,j} = \left( \frac{\partial q_N}{\partial t} \right)_{i,j} = 0 \quad (35)$$

Phase one is completed by updating the tangential flow velocity in the partial cell based on a finite difference approximation to the tangential equation of motion. This involves approximating the tangential pressure gradient by resolving the radial and axial pressure gradients into the tangential direction. The radial and axial pressure gradients are calculated in the same manner as for fixed boundary partial cells as used in Equations (26) and (27) above. The resulting finite difference approximation to the tangential pressure gradient is:

$$\begin{aligned} \left(\frac{\partial P}{\partial T}\right)_{i,j}^n &= \frac{1}{F_{i,j}} \left\{ \hat{A}_{2-4} \cos \theta'_{i,j} \left( \frac{P_{i-1,j}^n - P_{i+1,j}^n}{2\Delta r_i} \right) \right. \\ &\quad \left. - \hat{A}_{1-3} \sin \theta'_{i,j} \left( \frac{P_{i,j-1}^n - P_{i,j+1}^n}{2\Delta z_j} \right) \right\} \end{aligned} \quad (36)$$

where as before

$$\hat{A}_{1-3} = \max [A_1, A_3]_{i,j} \quad (37)$$

$$\hat{A}_{2-4} = \max [A_2, A_4]_{i,j}$$

and cell sides are as numbered in Figure 6. Also the pressures in fictitious cells completely within the solid boundary are set equal to the pressure in the cell (i,j) as prescribed by the reflection boundary condition. Based on this form of the tangential pressure gradient, the tangential flow velocity is updated to the intermediate stage as follows:

$$\left(\tilde{q}_T\right)_{i,j} = \left(q_T\right)_{i,j}^n + \frac{\Delta t}{\rho_{i,j}} \left(\frac{\partial P}{\partial T}\right)_{i,j}^n \quad (38)$$

The axial and radial velocities in the partial cell are found simply by resolving  $\tilde{q}_N$  and  $\tilde{q}_T$  in the respective directions as follows:

$$\tilde{u}_{i,j} = \left(\tilde{q}_N\right)_{i,j} \sin \theta'_{i,j} + \left(\tilde{q}_T\right)_{i,j} \cos \theta'_{i,j} \quad (39)$$



$$\tilde{v}_{i,j} = \left( \tilde{q}_N \right)_{i,j} \cos \theta'_{i,j} - \left( \tilde{q}_T \right)_{i,j} \sin \theta'_{i,j} \quad (40)$$

Phase one is then completed by updating the internal energy in the partial cell to the intermediate state using the same equation as used for fixed boundary cells (Equation 28). The computational cycle is again completed by treating mass, momentum and energy transport in phase two. In this phase the solid boundary is considered fixed so that the treatment of the transport terms is identical to that described above for the fixed boundary cells.

For application to the projectile boundary, in the muzzle blast calculation, the method described here is considerably simplified since for rigid body, axisymmetric motion;

$$U_q(t) = 0, \quad V_q(t) = V_p(t) \quad (41)$$

for all beads on the projectile boundary.  $V_p$  is the projectile velocity whose time history is determined by the rigid body projectile dynamics based on the integrated pressure forces on the projectile surface. This is described in Section 4.3 below.

As with the treatment of fixed boundaries, the numerical treatment of moving boundaries given in this section is one of numerous alternative techniques which could be devised. In fact, in the present study, one alternate technique was examined. In the method, the Lagrangian equation of motion normal to the solid boundary was solved for the pressure in the boundary cell. However, when applied in the test case of an impulsively accelerated projectile (Section 5.1), the method led to unacceptable pressure oscillations in the early stages of the calculation. Thus it was decided to use the method described above, in which the pressure is not updated in phase one but is calculated at the end of phase two as in a normal cell. The relatively good results calculated for the same test case using the present method lend some justification to its use. The test cases described in Section 5 indicate that the method given here is quite stable and of acceptable accuracy, at least for one dimensional rigid body boundary motion.

### 3.4 Stability and Accuracy Considerations

The finite difference scheme given above is first order accurate in both mesh spacing ( $\Delta r$ ,  $\Delta z$ ) and time increment ( $\Delta t$ ). This means that the truncation errors, introduced as a result of the approximation, are linearly proportional to  $\Delta r$ ,  $\Delta z$  and  $\Delta t$ . Both accuracy and stability of the numerical scheme are closely related, and are affected by the functional form of the truncation errors. In a time dependent calculation, numerical instabilities can be unbounded, which are catastrophic, or may take the form of bounded oscillations in flow quantities. The latter clearly affect the accuracy of the solution and although they may be within acceptable bounds, they are annoying. The overall accuracy of the time dependent solution depends, in addition to stability considerations, upon the manner in which errors accumulate or cancel with time. This is not subject to analysis, however, so that a final determination of solution accuracy must necessarily depend upon comparisons to experiment or exact solutions.

Rich<sup>1</sup> and others have analyzed the nature of the truncation errors implicit in the fluid-in-cell differencing technique, and have shown that they take the form of viscous diffusion. For example in the axial momentum equation the leading order truncation error is of the form:

$$\epsilon = \frac{1}{2} \frac{1}{r} \frac{\partial}{\partial r} \left( \rho u r \Delta r \frac{\partial v}{\partial r} \right) + \frac{1}{2} \frac{\partial}{\partial z} \left( \rho v \Delta z \frac{\partial v}{\partial z} \right) \quad (42)$$

The corresponding terms in the radial momentum and energy equations are similar. It is noted that the truncation error is akin to a viscous diffusion with a non-isotropic "numerical viscosity" which depends on the local flow velocity, density and mesh spacing. The diffusive nature of the truncation error terms is in fact essential to the success of the fluid-in-cell technique. These terms effectively stabilize the difference equations to small perturbations introduced by boundary conditions. They also serve the important function of smoothing out discontinuities such as shock fronts, thus permitting the calculation of these important phenomena without special treatment.

The effective numerical viscosity is seen to be small in regions of the flowfield with low density or velocity. This is the reason that oscillations develop in stagnation regions (velocity  $\sim 0$ ) or in the rapid expansion following a strong shock, as noted by other investigators. These oscillations can be reduced by the introduction of an "artificial viscosity" in the form of a viscous stress. The various forms possible are discussed in standard works which describe time dependent methods<sup>4</sup>. No such artificial viscosity is used in the present study, since it is believed that stable muzzle blast calculations can be performed without it. Thus the additional inaccuracies resulting from an artificial viscosity are avoided.

The basic stability consideration in the present numerical technique is the Courant condition. All explicit difference methods are subject to the restrictions that the "domain of dependence" of the finite difference approximation be such as to include the domain of dependence of the physical process being modeled. In the present form it requires that a signal cannot travel more than one cell width during a time step  $\Delta t$ . For a given finite difference grid this places a restriction on the maximum allowable time step. In this study the form of the Courant condition used is:

$$\Delta t < \min_{i,j} \left( \frac{\min(\Delta x_i, \Delta z_j)}{a_{i,j} + \sqrt{u_{i,j}^2 + v_{i,j}^2}} \right) \quad (43)$$

where  $a$  is the sound speed and all cells in the grid are tested. This is the most restrictive form of the Courant condition and is valid for both subsonic and supersonic flow speeds. The restriction on  $\Delta t$  also satisfies the requirement that an Eulerian cell cannot be emptied during one time step. It is noted in passing that the Courant condition is the basic factor, apart from the efficiency of the overall scheme, which determines the computer time required to perform an unsteady calculation to a certain physical time. For the muzzle blast problem, the region in and around the muzzle is of most interest and will therefore be the region in which small cells are to be concentrated for accurate resolution. This region of the

flow is the most restrictive in terms of the Courant condition since flow velocity and temperature (therefore sound speed) are greatest there. Thus the design of an efficient grid for the muzzle blast problem will, as usual, require a trade-off between solution accuracy and computer time.

As a final remark it is noted that the numerical treatment of boundary conditions can have an important effect on computational stability. This is an area which is difficult to examine analytically so that it is generally studied by numerical experimentation. In a qualitative sense improper treatment of boundaries can generate spurious signals which can be transmitted throughout the grid thereby affecting solution accuracy and possibly stability, if the signals become concentrated in low speed regions of the flow. In the muzzle blast problem the solid muzzle boundaries and the farfield boundaries are important in this regard. The effect of solid boundaries is discussed with regard to the test case results given in Section 5.0. The treatment of farfield boundaries to eliminate spurious signals which could be reflected back into the flowfield is discussed in Section 4.0 below. A more explicit way in which boundaries can affect stability is by way of the reduced cell dimensions of partial boundary cells. Partial cells which are much smaller than their full-sized counterparts should thus be avoided if possible when setting up the grid and defining bead locations.

#### 4.0 SPECIFICS OF METHOD FOR MUZZLE BLAST PROBLEM

The numerical method described above has somewhat general application to fluid mechanic problems with fixed and moving solid boundaries. However, calculations performed to date with the computer program, SAMS, have been relevant to the muzzle blast problem. Some specifics of the method for application to the muzzle blast problem are presented in this section. The items discussed include: muzzle gas equation of state in Section 4.1, specification of the time history and transient boundary condition defining flow out of the barrel and treatment of farfield boundaries in Section 4.2, and coupling of projectile motion to the flowfield in Section 4.3.

##### 4.1 Equation of State

The SAMS code, as presently configured, allows only one equation of state. This is somewhat of a limitation for the muzzle blast problem since two different gases are involved; the high temperature and high density combustion products which make up the muzzle jet and the ambient air. Fortunately, both gases have similar molecular weights and can be expected to follow a perfect gas law at low fluid densities. Since the flow of muzzle gases in and around the muzzle device and projectile, is of most interest to this study, it was decided to use an equation of state characteristic of the muzzle gas. The effect which this has on the accuracy of the flow of ambient air driven by the muzzle jet is commented on below.

The equation of state used in this study is the Nobel-Abel equation of state which for our purposes can be written in the form:

$$P = \frac{(\gamma-1) \rho I}{(1-\beta\rho)} \quad (44)$$

where  $\gamma$  is the ratio of specific heats and  $\beta$  is the covolume. The values of  $\gamma$  and  $\beta$  which are typical of the muzzle gases and therefore used here are:

$$\gamma = 1.24$$

(45)

$$\beta = 0.001 \text{ m}^3/\text{kg}$$

It is noted that Equation (44) is the perfect gas law with a correction for Vander Waal's forces. The equation should be quite accurate for the muzzle gases. Two types of errors are introduced in applying this equation of state to the ambient air. The first is minor and concerns the effect of the covolume correction. For the strongest air shocks expected,  $\rho$  will be considerably less than  $10 \text{ kg/m}^3$ . Thus the covolume correction with  $\beta = 0.001 \text{ m}^3/\text{kg}$  will introduce an error of less than 1.0 percent. A more appropriate value for the ratio of specific heats for air is  $\gamma = 1.4$ , so that a more serious error is introduced by using the effective  $\gamma$  of 1.24 for air. Thus the pressure jump and velocity of the shock wave in the ambient air and the projectile blunt body shock will be considerably lower than they should be.

Since the prime objective of this study was to develop and verify the numerical technique, no attempt was made to develop an equation of state which more accurately modeled both the muzzle gases and ambient air. A more accurate treatment could be accomplished in a number of ways. For example, the single Nobel-Abel equation of state could be retained but with a varying  $\gamma$ . This could be made quite accurate by defining  $\gamma$  in such a manner that it matches the value for air at low density or internal energy and matches values typical of the muzzle gases at high densities and internal energies. An alternate, and potentially more accurate, technique would be to use the tracer particles which define the contact surface between the muzzle gases and air, to differentiate between regions of the flowfield in which the muzzle gas or air equation of state is to be used. Variations of such a technique are used in later versions of the OIL code (DØRF<sup>10</sup>, HELP<sup>11</sup>) to permit multi-fluid calculations.

#### 4.2 Muzzle Flow and Farfield Boundary Conditions

In addition to the solid boundary condition discussed in Section 3.3, two additional types of boundary

conditions occur in the muzzle blast problem. They occur in many flow problems and are generally known as continuous inflow and outflow boundary conditions, respectively. The inflow boundary is needed to define the flow of muzzle gases into the solution field at some location inside the gun barrel, upstream of the muzzle device. Also outflow boundary conditions are defined on the far boundaries of the finite difference grid. The numerical treatment of both boundaries are discussed in this section.

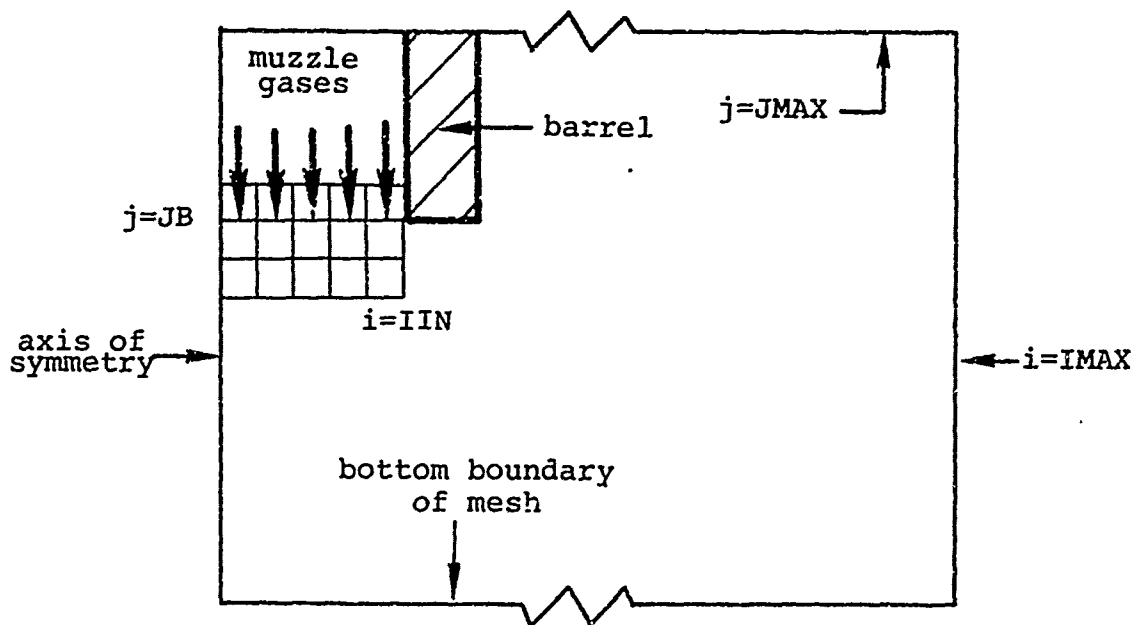


FIGURE 7. SCHEMATIC OF NUMERICAL SOLUTION DOMAIN

The muzzle gas flow out of the gun barrel is treated as a transient boundary condition fixed at the muzzle exit ( $j=JB$ ) as shown in Figure 7 above. This boundary condition is treated in a relatively straightforward manner by defining the flow properties in fictitious cells based on curve-fits to experimental data or independent calculations of the flow out of the muzzle. Thus, set

$$P_{i,JB+1}^n = P_M(t^n), \rho_{i,JB+1}^n = \rho_M(t^n), I_{i,JB+1}^n = I_M(t^n) \quad (46)$$

$$u_{i,JB+1}^n = 0, v_{i,JB+1}^n = V_M(t^n)$$

for  $0 < i \leq IIN$

The properties in the fictitious cells are updated in this manner in phase one of the computational cycle and used in the appropriate finite difference forms. They are also used in phase two to determine the transport of mass, momentum and energy through the top boundary of the cells at  $j = JB$ ,  $0 < i \leq IIN$ , in the usual donor cell form. The time dependent properties ( $P_M$ ,  $\rho_M$ , etc.) for an M-16 rifle are given in Appendix B and used in the manner described here for the test case calculation presented in Section 5.0.

An alternate, and more exact, method for treating the muzzle flow properties, would be to include the inside of gun barrel in the finite difference grid. Initial conditions ( $t = 0$ ) for the gas inside the barrel could be defined very accurately by an internal ballistics solution. The muzzle blast calculation would then be initiated when the projectile moves to permit the gas to vent. This would result in an expansion wave which would proceed upstream through the column of gas in the barrel. The finite difference grid inside the barrel could be quite coarse in comparison to the grid just outside the barrel. In this method, the flow inside the barrel would be coupled to the resulting muzzle blast flowfield so that no approximation (other than finite difference) would be involved. On the time scale of transitional ballistics ( $t < 100$  microseconds) the muzzle flow properties vary but a few percent so that either of the above methods should be quite accurate for the purpose of this study.

The other boundary condition needed in the muzzle blast computation, involves the far boundaries of the finite difference grid as shown in Figure 7. The



axis of symmetry ( $r = 0$ ) is treated as a reflective boundary as already discussed. The other boundaries of the grid ( $j = 0$ ,  $j = JMAX$  and  $i = IMAX$ ) must also be treated in some sense. It is noted that the interaction of the flow with grid boundaries is almost always a problem in finite difference calculations. If the boundary is not treated in a physical manner, spurious signals can be generated which may destroy a time dependent calculation. The most difficult type of interaction to treat is the passage of a shock through the boundary which unfortunately could occur in the muzzle blast problem. Ideally the boundary would completely absorb (or transmit) the shock but in practice this is difficult to accomplish since the flow outside the grid clearly depends in a complex manner on the flow inside the grid. With this problem in mind, it is a good idea to place the far boundaries far enough away from the flow region of interest (muzzle) so that the calculation either terminates before the shock reaches the boundary or before any reflected signals can interact with the flow regions of interest. This can be accomplished by stretching the grid.

In any event the method presently used for these boundaries is known as the "transmittive" or continuous "outflow" boundary condition". The method simply involves defining flow properties in fictitious cells outside the boundary to be equal to the flow properties in the adjacent active cells inside the boundary. This is done at all stages of the calculation. This treatment in essence fixes the flow gradients equal to zero at the grid boundaries, and clearly can be accurate only very far from any active region of the flowfield.

#### 4.3 Dynamics of Projectile Motion

As noted in an earlier section, the projectile is initially accelerating with respect to the muzzle due to the high muzzle gas pressure at its base. At later times it decelerates as the muzzle gas expands around the projectile thereby decreasing the base pressure. In this study, the response of the projectile to the time varying pressure forces, exerted on its surface, is treated. Since the calculation is inviscid, only pressure forces are relevant. Also the calculation is axisymmetric, so that only the axial motion of the projectile need be considered.

The projectile equation of motion in the axial direction is simply:

$$M_p \frac{dv_p}{dt} = \int_{A_p} P(\hat{e}_z \cdot \hat{n}) dA \quad (47)$$

where  $M_p$ ,  $V_p$  are the mass and velocity of the projectile respectively and  $\hat{e}_z$  is the unit vector in the axial direction and  $\hat{n}$  is the unit normal to the projectile surface element  $dA$ . The finite difference approximation to Equation (47) is used to update the projectile velocity to the advanced time  $t^{n+1}$  starting with its initial muzzle velocity at time  $t = 0$ . Summing the pressure forces in each of the partial cells on the projectile boundary, results in the following finite difference form:

$$v_p^{n+1} = v_p^n + \frac{\Delta t}{M_p} \sum_{k_p} P_{i,j} \pi (r_{i+1}^2 - r_i^2) \quad (48)$$

where the summation is over all the boundary cells with index  $k_p$ .

Over a time scale typical of transitional ballistics ( $t < 100$  microseconds) the change in projectile velocity is negligible. In calculations performed to date, the change has been less than 1 m/sec. As a result, the SAMS code has a constant projectile velocity option which eliminates the need for performing the calculation described here.

## 5.0 TEST CASE RESULTS

As has been stated a number of times in this report, the main innovation in the numerical technique presented here is the treatment of fixed or moving solid boundaries in an Eulerian grid. It is well known that boundary conditions are often crucial to any finite difference technique for fluid mechanics problems. This is especially true of the muzzle blast problem since so many of the interesting phenomena are a result of flow interaction with fixed or moving boundaries. Thus the first test case, presented in Section 5.1, was performed to verify the accuracy and stability of the treatment of moving boundaries. The complete computer program capability is exercised in the typical muzzle blast test cases presented in Sections 5.2 and 5.3. These calculations simulate the muzzle gas flow of an M-16 rifle with and without a simple muzzle device

### 5.1 Blunt Projectile Impulsively Started From Rest

This test case involves the calculation of the flow around a flat-faced cylindrical projectile accelerated impulsively to 1500 m/sec in an ideal gas ( $\gamma = 1.3$ ) at rest. The calculation was performed by passing the rigid boundary defining the projectile surface through a fixed Eulerian grid. The purpose of the calculation was to check out the logic, accuracy and stability of the partial cell technique described above for moving solid boundaries.

A schematic, describing the geometry and parameters for this test case, is presented in Figure 8 below. The cylinder has a radius of 0.5 cm and length of 0.5 cm and its velocity is taken as 1500 m/sec. The ambient gas is considered ideal with  $\gamma = 1.3$ . For these conditions the projectile Mach number is  $M_\infty = 5.0$ . The finite difference grid was made up of zones with dimensions  $\Delta x = \Delta y = 0.1$  cm, and its extent was 1.5 cm in radius by 2.0 cm in the axial direction. The maximum allowable time step was determined by the Courant condition with Courant number = 0.25. No hint of numerical instability was evident in the calculated results, indicating that a larger Courant number could have been used with success.

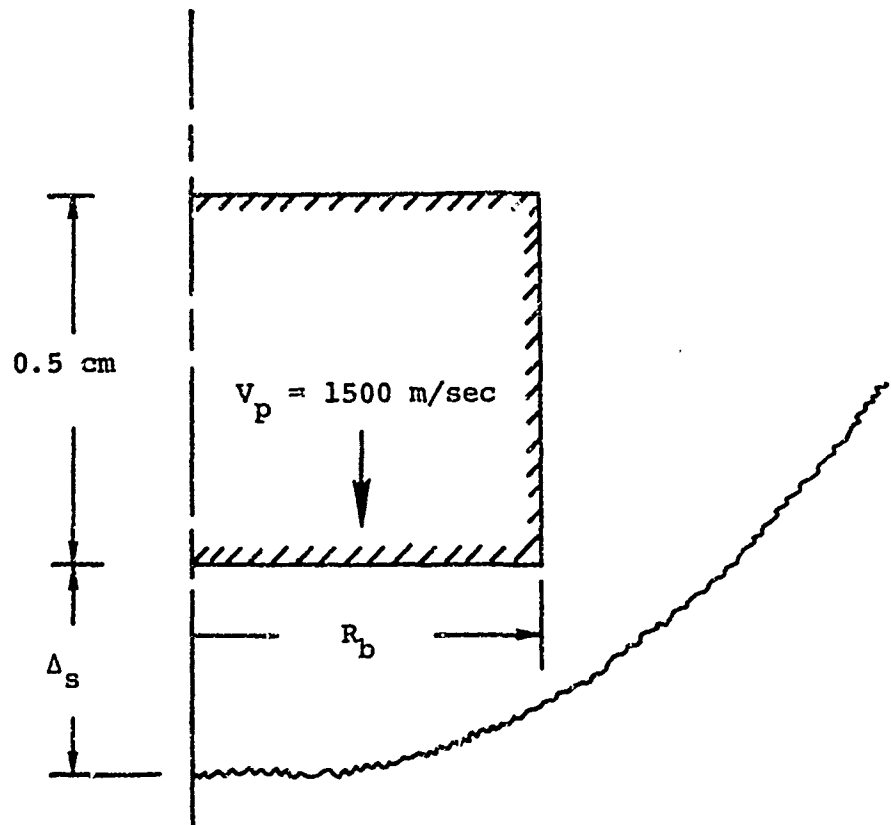


FIGURE 8. SCHEMATIC OF CYLINDRICAL PROJECTILE  
ACCELERATED IMPULSIVELY TO 1500 M/SEC

The figures given at the end of this section compare the calculated results to theoretical and experimental results. The theoretical stagnation conditions for  $M_\infty = 5.0$ ,  $\gamma = 1.3$ ,  $T_{\text{ambient}} = 292\text{K}$  and  $P_{\text{ambient}} = 0.824$  bars are:

$$P_s = 26.2 \text{ bars}$$

$$T_s = 1420^\circ \text{ K}$$

$$\rho_s = 8 \text{ kg/m}^3$$

Theoretically, the axis of the cylinder should reach these conditions at steady state. Figures 9, 10, 11 given below, give the time history of the pressure, temperature and density respectively, of the finite difference zone on the axis, just ahead of the projectile. These results are shown compared to the theoretical stagnation conditions and the comparison is judged good considering the crudeness of the mesh. The over-prediction of temperature is consistent with the dissipative nature of the higher order terms resulting from the discretization process.

Experimental results for shock stand-off distance<sup>13</sup> for a flat-faced cylinder at  $M_\infty = 5$  indicate that:

$$\frac{\Delta_s}{D_b} = \frac{\Delta_s}{2R_b} = 0.3 \quad (49)$$

Thus for the 1 cm diameter projectile of this test case  $\Delta_s = 0.3$  cm. The numerical results are consistent with this experimental result. If the shock is defined by the maximum pressure or density gradient, the numerical results predict a shock in the third finite difference zone in front of the projectile or  $\Delta_s|_{\text{numerical}} = 0.25$ . This compares to the numerical result within the accuracy of the finite difference mesh.

One final check on the computed results can be obtained by comparing the radial velocity on the face of the cylinder with theoretical predictions. The constant density shock layer solution of Probstein<sup>14</sup> predicts a radial velocity distribution given by:

$$\frac{U}{U_\infty} = \frac{4}{3\pi} \left( \frac{\rho_\infty}{\rho_s} \right)^{1/2} \left( \frac{1}{1 + \frac{\Delta_s}{R_b}} \right) \frac{r}{R_b} \quad (50)$$

where  $U_\infty$  or  $V_p$  is the velocity of projectile,  $\rho_s$  and  $\rho_\infty$  are the stagnation density and ambient density, respectively.

$\Delta_s$  is the shock stand-off distance and  $r$ ,  $R_b$  are the radius and body radius, respectively. This solution compares favorably with experiment for  $r/R_b \leq 0.5$ . Comparison of the numerical results (at  $t = 7$  microseconds) with this theoretical radial velocity distribution are shown in Figure 12 below. The comparison is again judged to be quite good. The fact that the numerical result is below the theoretical indicates that the calculation may not have reached steady state.

This test case is a relatively severe test of the numerical treatment of moving boundaries. The comparison of results with experiment and theory is good and within the accuracy of the relatively crude finite difference mesh. The mesh was chosen as typical of the mesh size used in the region of the projectile in a complete muzzle blast calculation considering practical usage of computer storage and computational time. No hint of numerical instability or bounded oscillations was evident in the calculation. The only anomaly was the nonuniformity of the time history of flow pressure and density in the partial boundary cells as shown in Figures 9 and 11. This is not serious, however, and it is believed that finer zoning would result in smoother results.

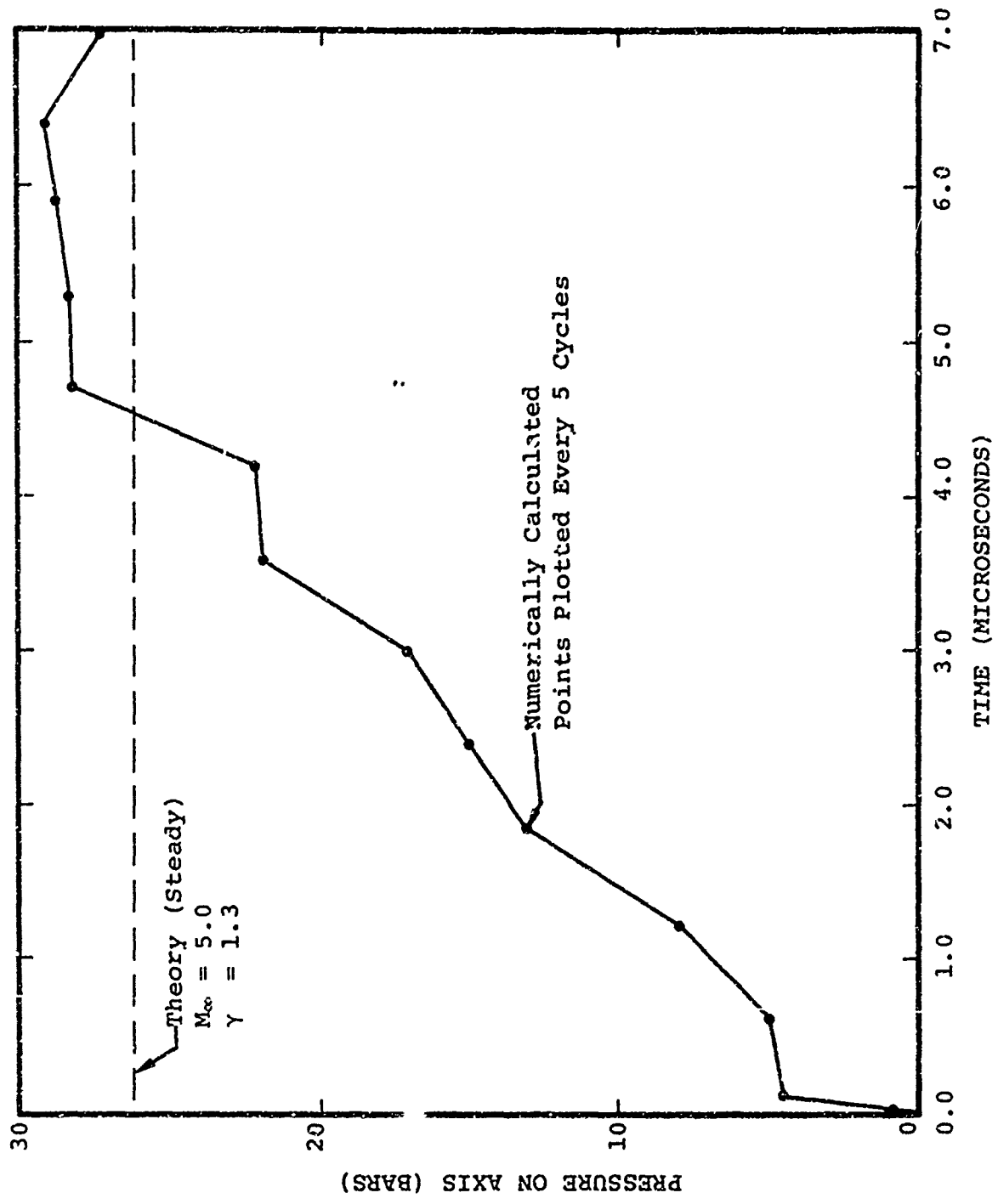


FIGURE 9. STAGNATION PRESSURE VS TIME

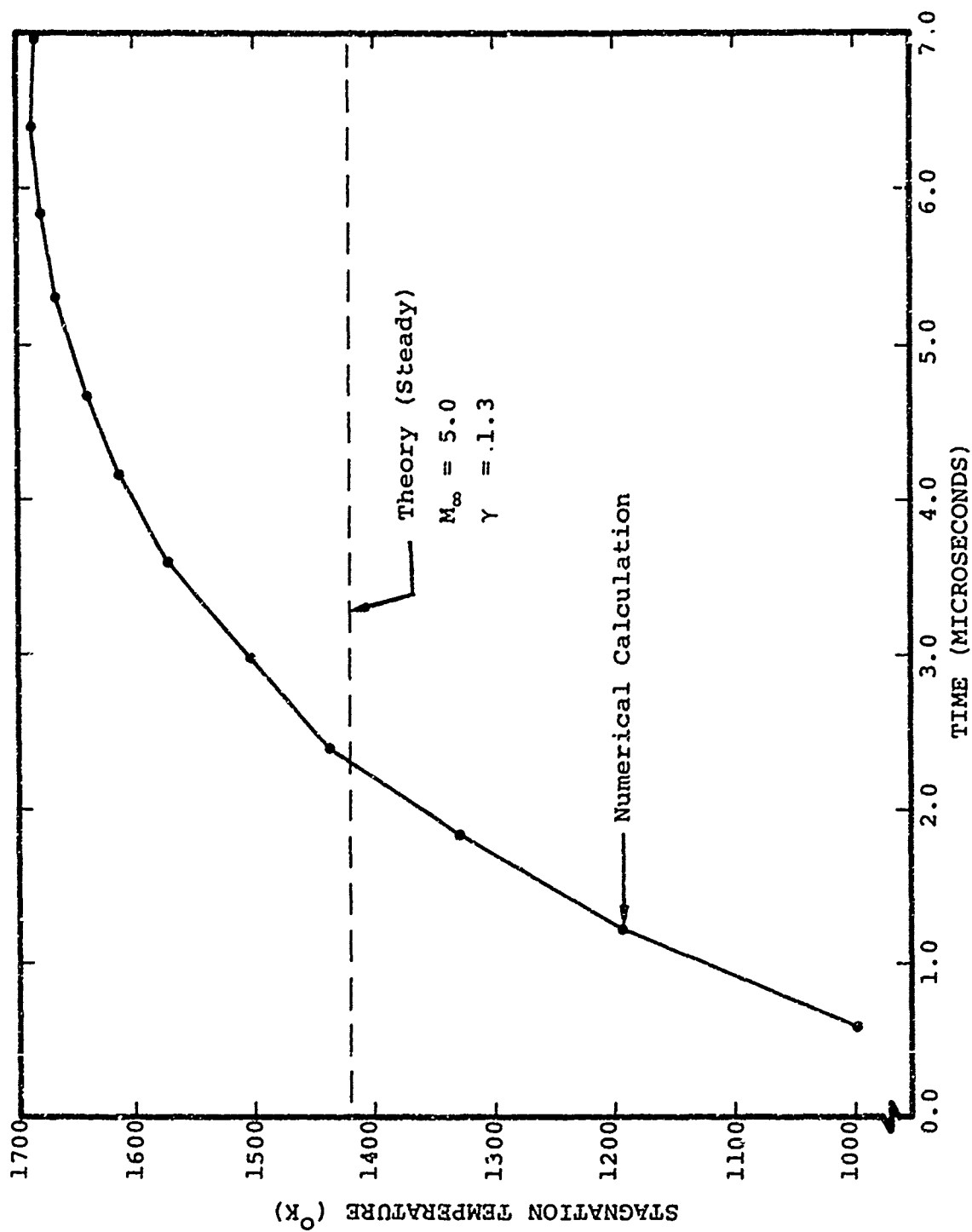


FIGURE 10. STAGNATION TEMPERATURE VS TIME



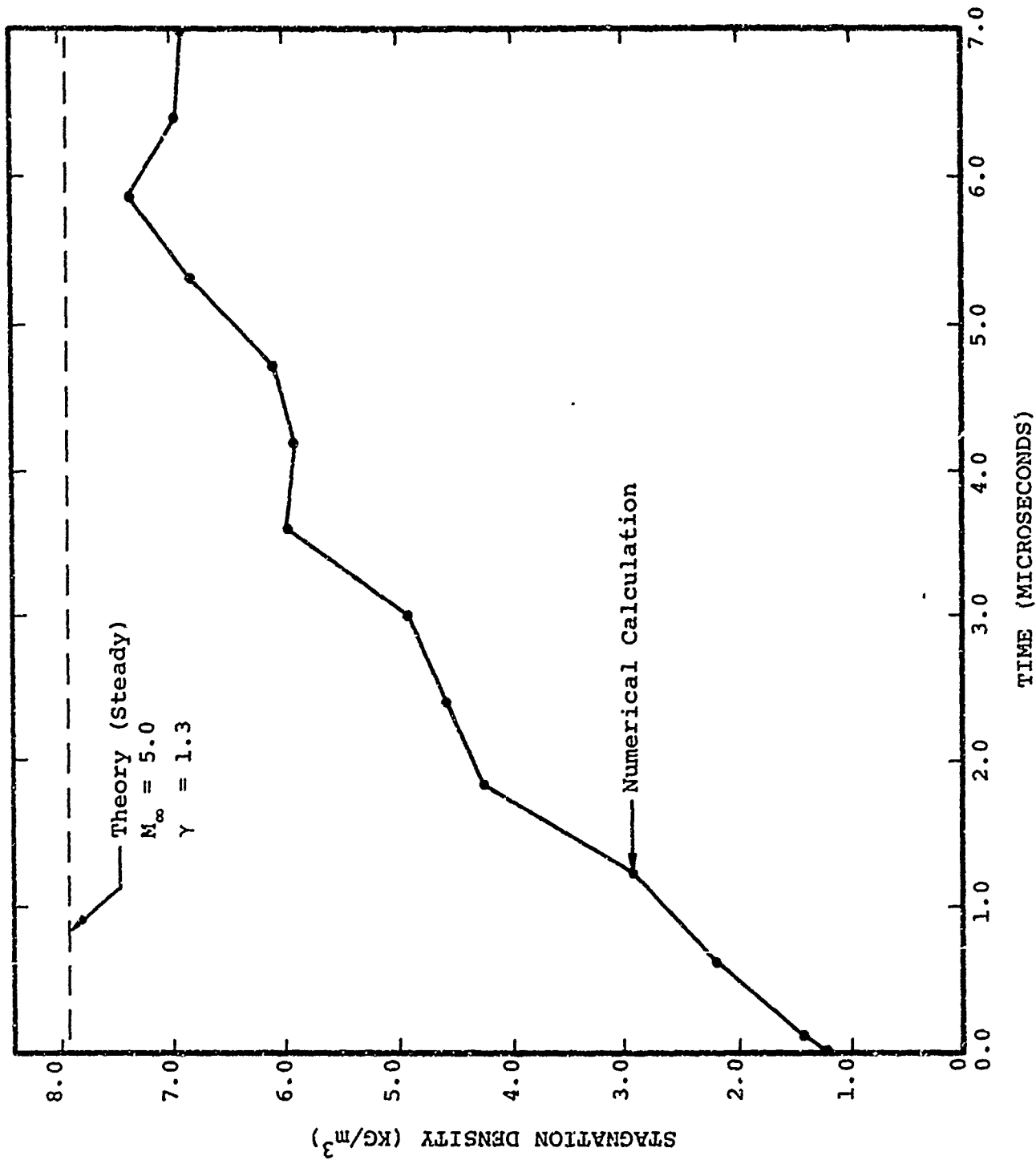


FIGURE 11. STAGNATION DENSITY VS TIME

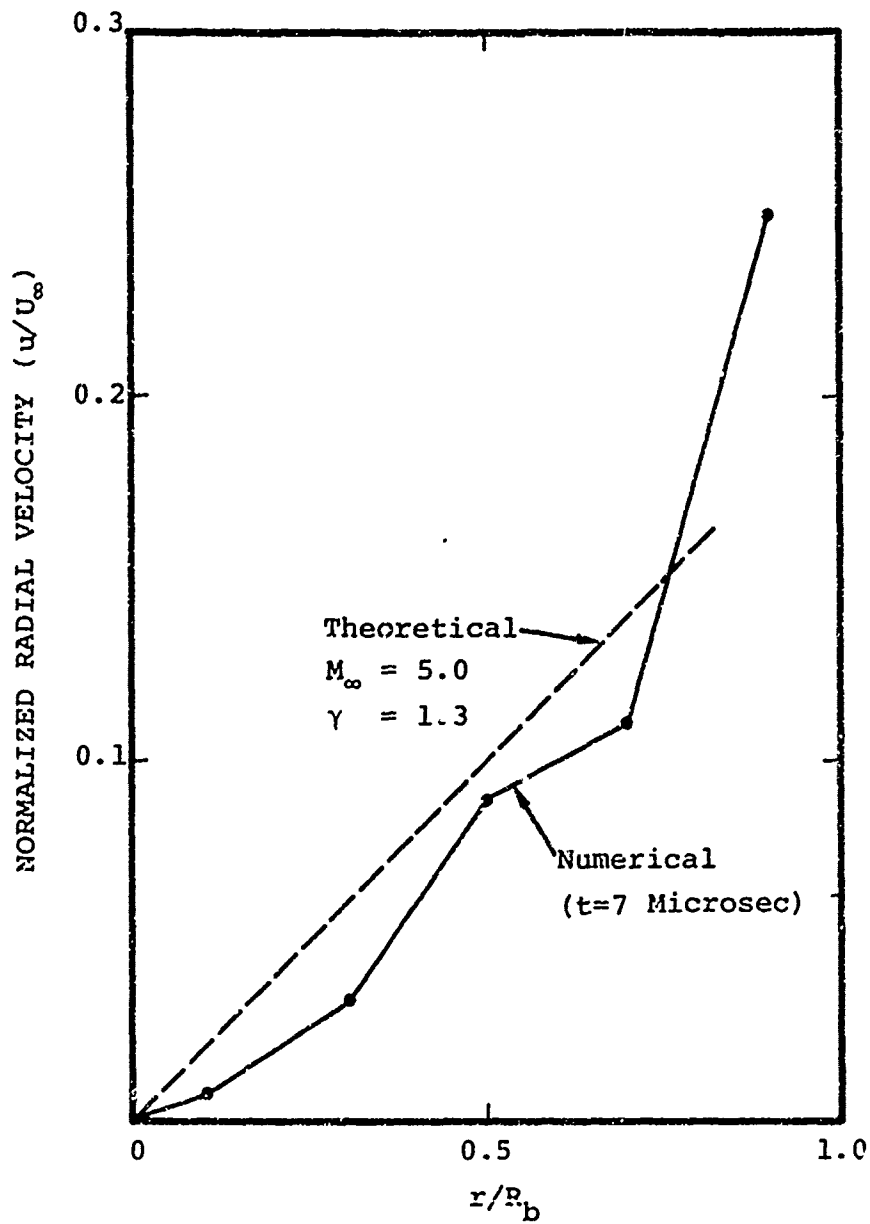


FIGURE 12. COMPARISON OF THEORETICAL TO NUMERICAL RESULTS FOR RADIAL VELOCITY DISTRIBUTION ON FRONT FACE OF BODY

## 5.2 M-16 Muzzle Blast Flowfield

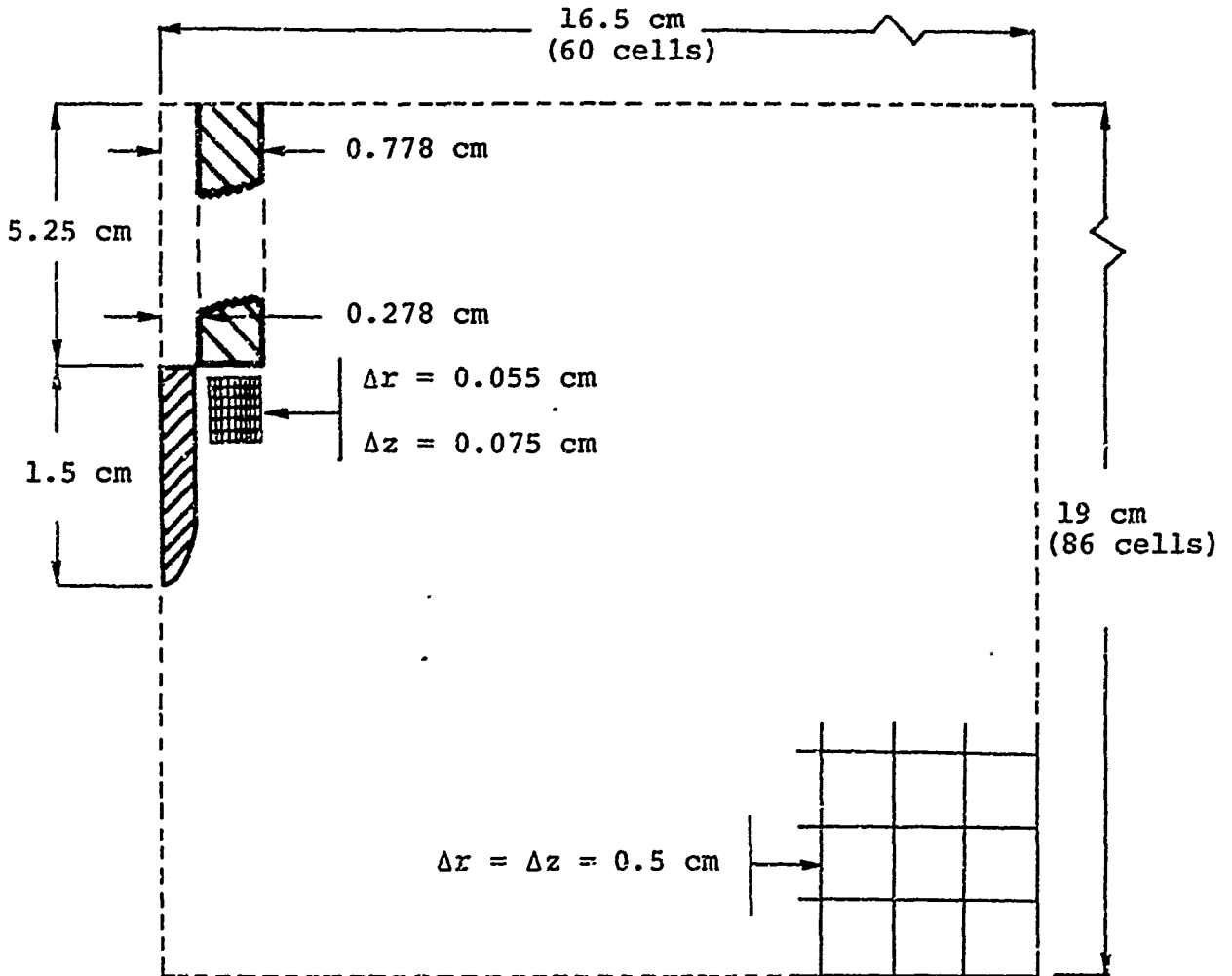


FIGURE 13. SCHEMATIC OF M-16 MUZZLE BLAST CALCULATION

The SAMS code was used to calculate the muzzle blast flowfield of an M-16 rifle and the calculated results are presented in this section. The muzzle and projectile geometry and finite difference grid design are

shown schematically in Figure 13. The muzzle consists of a cylinder with an inside diameter of 0.556 cm (5.56 mm bore) and outside diameter of 1.556 cm. The Nobel-Abel equation of state, described earlier, was used for both the muzzle gas and ambient air and the transient flow properties at the muzzle exit were determined from an independent calculation of Celmins<sup>1,2</sup> (see Appendix B). Based on these flow properties, a projectile muzzle velocity of 1210 m/sec was used and was assumed constant throughout the calculation. The finite difference grid was varied in a continuous manner from  $\Delta r = 0.055$  cm,  $\Delta z = 0.075$  cm near the muzzle exit to  $\Delta r = \Delta z = 0.5$  cm near the boundaries of the grid. The projectile was defined by a sequence of "beads," with its base initially ( $t = 0$ ) at the muzzle exit. Finally the integration time step was determined from the Courant condition with a Courant number of 0.3.

Computer generated plots of the calculated results are presented in Figures 14 through 27 at the end of this section. Figures 14 through 18 are velocity vector plots of the flowfield at increments of about 5 microseconds ( $\mu$  sec) (every 100 cycles) from  $t = 5.91 \mu$  sec (cycle 100) to  $t = 25.18 \mu$  sec (cycle 500). Figures 19 through 23 are pressure contour plots for the same times as the velocity vector plots. Pressure contours of 2, 10 and 100 bars are plotted. Finally, Figures 24 and 25 are density contour and temperature contour plots respectively at  $t = 10.93 \mu$  sec (cycle 200) and Figures 26 and 27 are corresponding plots at  $t = 25.18 \mu$  sec (cycle 500). Contours of 0.5, 2.0, 5.0 and 10.0 kg/m<sup>3</sup> are plotted in the density plots and contours of 500, 1,000, 2,000 and 3,000°K are given in the temperature plots.

The figures clearly show the development of all the expected phenomena. The advancing shock wave in the ambient air which weakens to a compression wave as it diffracts around the gun barrel is shown most clearly in the pressure contour plots (Figures 19 through 23). The transient development of the centered expansion wave originating at the corner of the gun barrel is also shown in the pressure plots. The relatively sharp pressure rise through the shock and its decay to a level below ambient with subsequent rise in the muzzle jet can also be seen. This behavior is characteristic of a spherical blast wave and is predicted by the calculation. Also note the development of the projectile blunt body shock and its interaction with the air shock.

The development of the jet of muzzle gas, shown in both velocity vector and pressure plots is seen to be characteristic of an under-expanded jet. It is noted that the jet soon reaches a "quasi-steady" state in the region around the exit. This is evidenced by the stable position of the 10 bar pressure contour from 5.91  $\mu$  sec on, and the stable position of the 2 bar contour from 20  $\mu$  sec on. The relatively steady muzzle jet flow is also shown in the density and temperature contour plots (Figures 24 through 27).

Two phenomena shown in the results are of particular note. The first is the separation of the flow at the corner of the muzzle face as shown in the velocity vector plots from 10.93  $\mu$  sec to 25.18  $\mu$  sec (Figures 15 through 18). The resulting recirculating flow region and mixing layer which extends from the corner and perpendicular to the barrel are clearly indicated. The flow separation is a physically real phenomena, not to be expected in an inviscid calculation, and is due to the numerical viscosity in the finite difference scheme. The second result of note is the shock wave in the muzzle jet at the base of the projectile. It is most clearly shown in the pressure, density and temperature plots at  $t = 10.9 \mu$  sec (Figures 20, 24 and 25 respectively). This is due to the expansion of the muzzle jet to a supersonic velocity relative to the projectile, and provides additional evidence that the numerical treatment of moving solid boundaries, developed in this study, is accurate.

The results presented here are physically reasonable in every way and are indicative of the quality of results which can be obtained with the SAMS code. Although no error estimates or extensive experimental comparisons have been performed, the results are believed to be accurate. All flow quantities are smoothly varying from cell to cell and no hint of numerical oscillation or instability is indicated with one exception. The exception is the existence of bounded oscillations in flow quantities in an isolated region of the flow on the low velocity side of the mixing layer described above. The oscillations are evident in the pressure plots, starting at cycle 300 (Figure 21) and extending to the end of the calculation. They do not destroy the calculation and remain in that region of the flow. It is noted that they occur in a low velocity ( $< 200$  m/sec) and low density ( $< 0.5$  kg/m<sup>3</sup>) region of the flow. It is recalled that the numerical viscosity in the finite difference scheme becomes ineffective for low velocities and low densities so that the oscillations could be due to the lack of numerical smoothing. It is important to point out that the

oscillations occur in the low velocity region of the mixing layer. It is well known that a mixing layer separating a low velocity from a high velocity flow is unconditionally unstable<sup>15</sup>, developing in turn vortex oscillations and ultimately turbulence. Thus the oscillations could be a result of the attempt of the inviscid theory to model a real physical phenomena. It is believed that the introduction of an artificial viscosity into the numerical technique would damp out the oscillations but this was not attempted in this study. An artificial viscosity could have adverse effects on other regions of the flow so that its use should be accompanied by extensive numerical experimentation.

One final comment which is of interest is that the calculation described in this section was performed in less than 16 minutes of CPU time on a CDC 6600. This indicates that muzzle blast calculations can be performed with computer program SAMS with a relatively modest investment in computer time.

VELOCITY VECTOR PLOT  
PROB. NO. 1.0  
CYCLE 100  
TIME  $5.91 \times 10^{-8}$  SEC

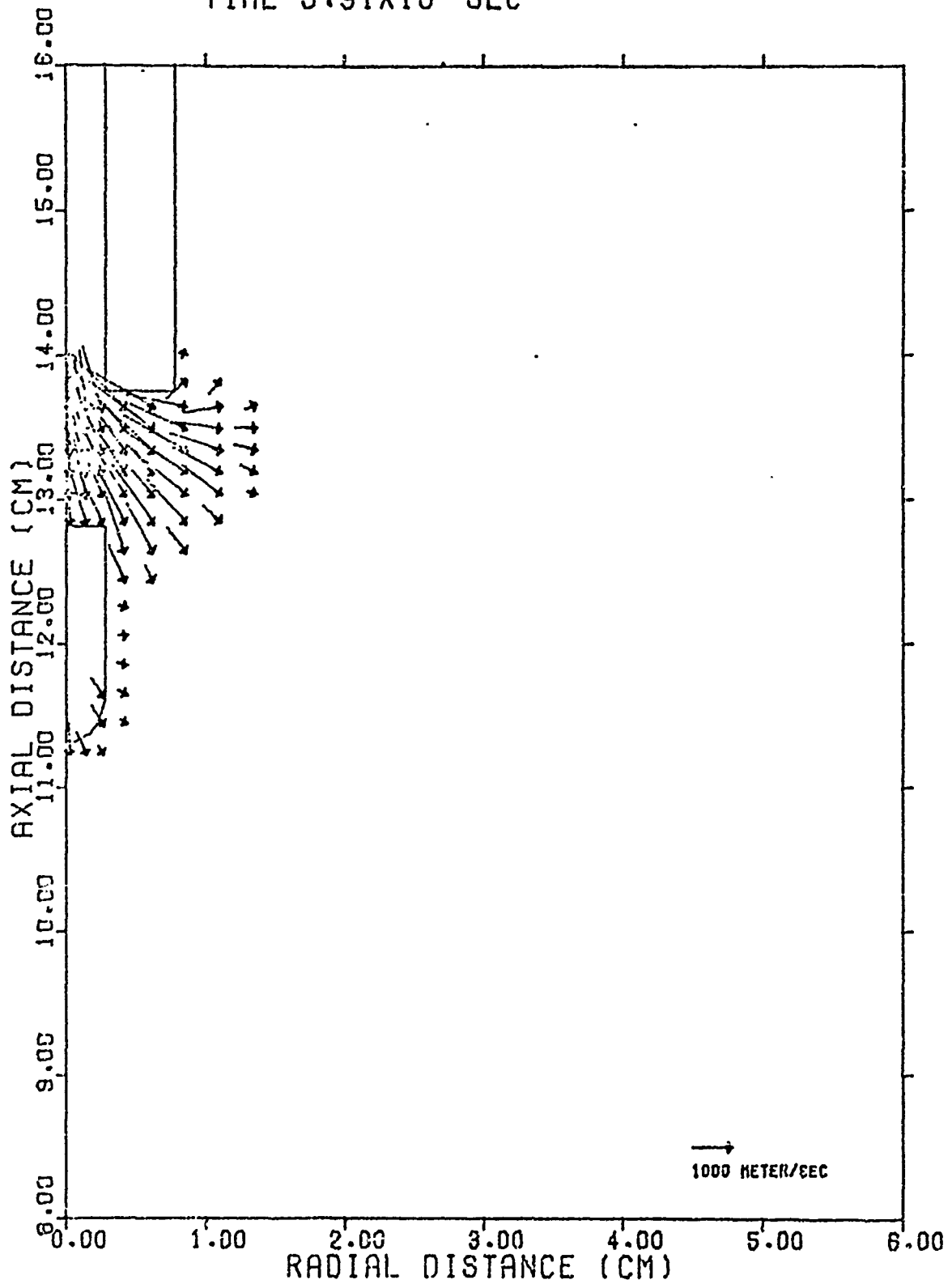


FIGURE 14. VELOCITY VECTOR PLOT: 11-16 RIFLE

VELOCITY VECTOR PLOT  
PROB. NO. 1.0  
CYCLE 200  
TIME  $10.93 \times 10^{-6}$  SEC

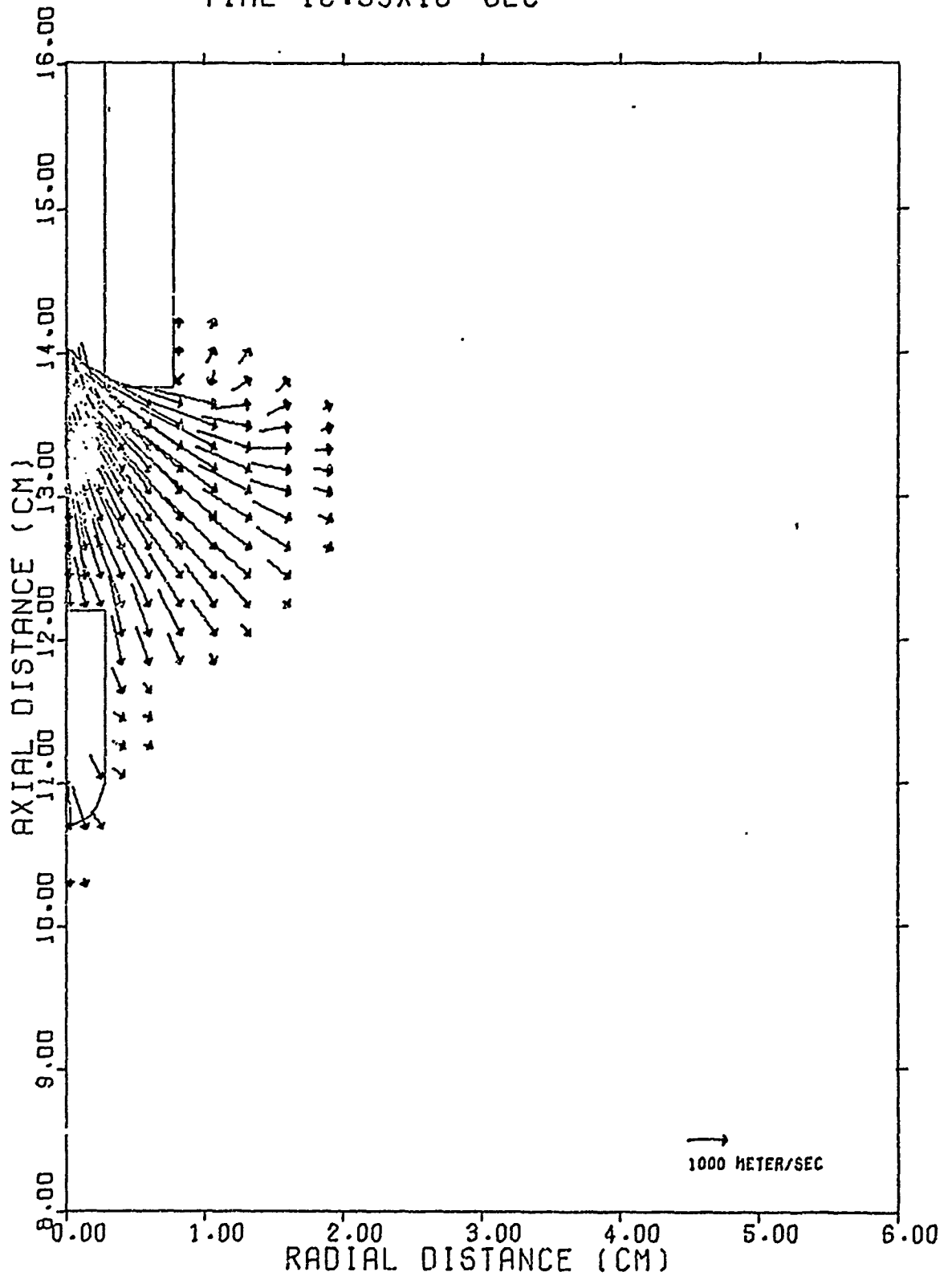


FIGURE 15. VELOCITY VECTOR PLOT: 11-16 RIFLE



VELOCITY VECTOR PLOT  
PROB. NO. 1.0  
CYCLE 300  
TIME  $15.73 \times 10^{-8}$  SEC

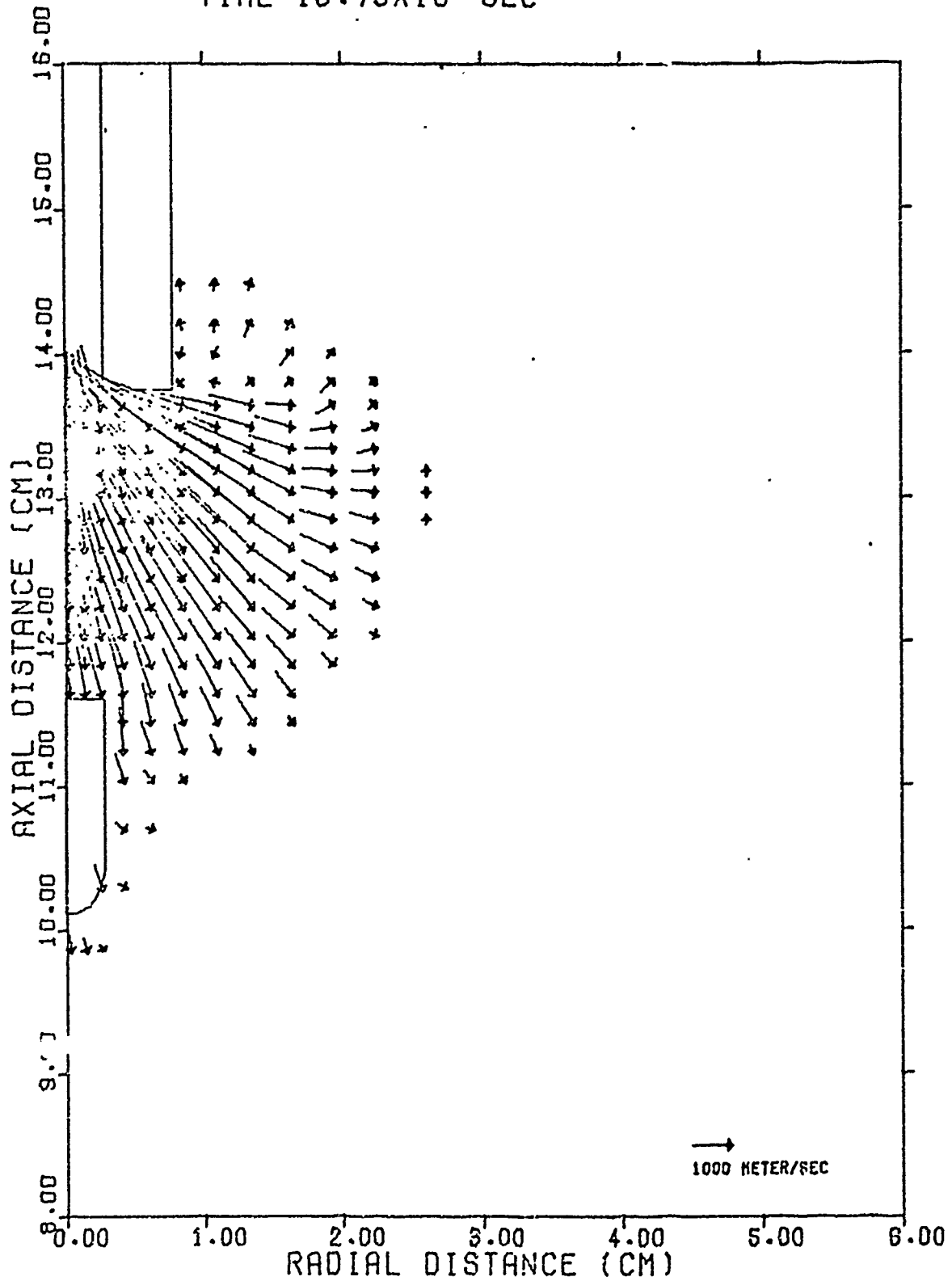


FIGURE 16. VELOCITY VECTOR PLOT: M-16 RIFLE

VELOCITY VECTOR PLOT  
PROB. NO. 1.0  
CYCLE 400  
TIME  $20.46 \times 10^{-6}$  SEC

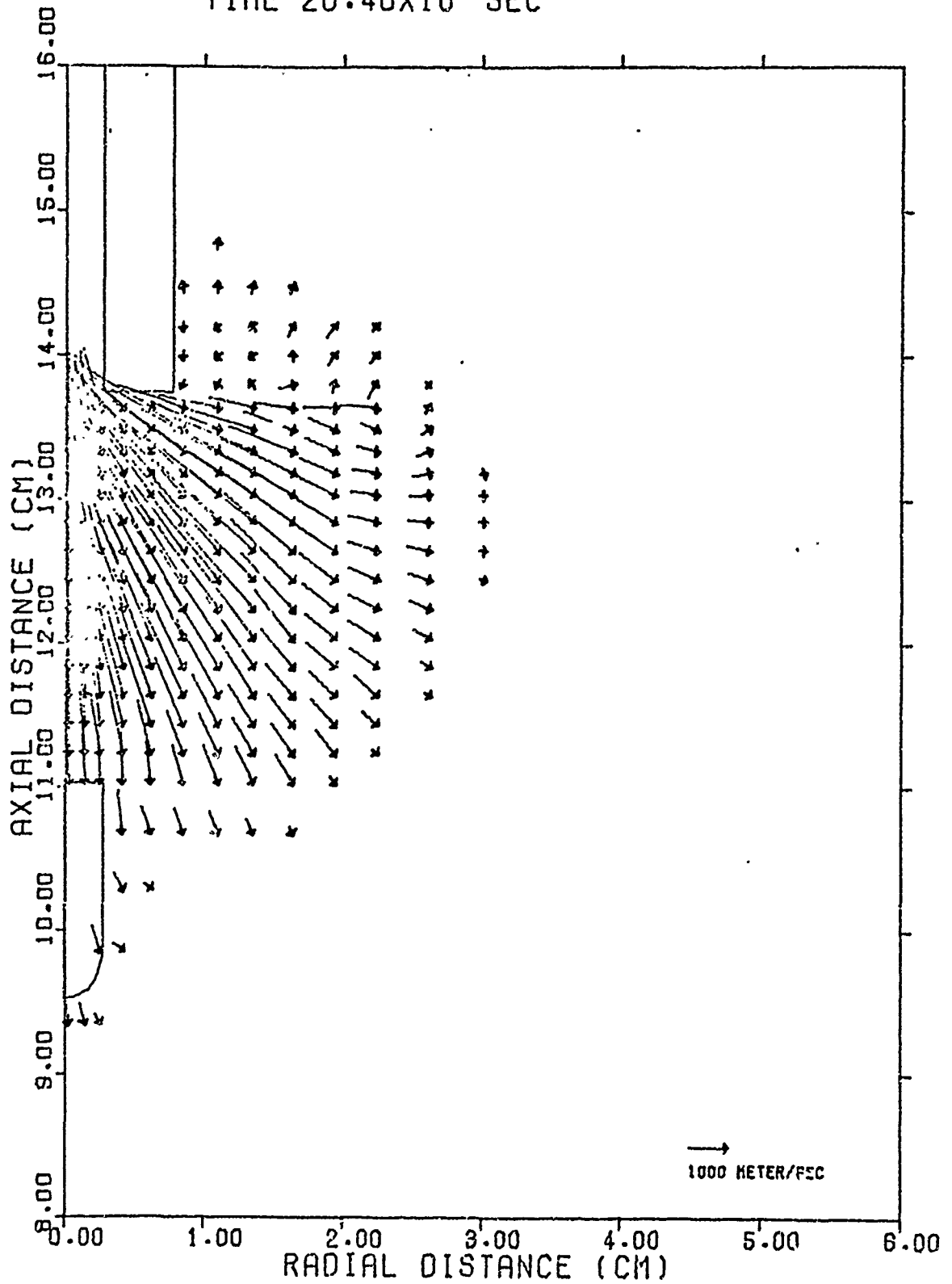


FIGURE 17. VELOCITY VECTOR PLOT: M-16 RIFLE

VELOCITY VECTOR PLOT  
PROB. NO. 1.0  
CYCLE 500  
TIME  $25.18 \times 10^{-6}$  SEC

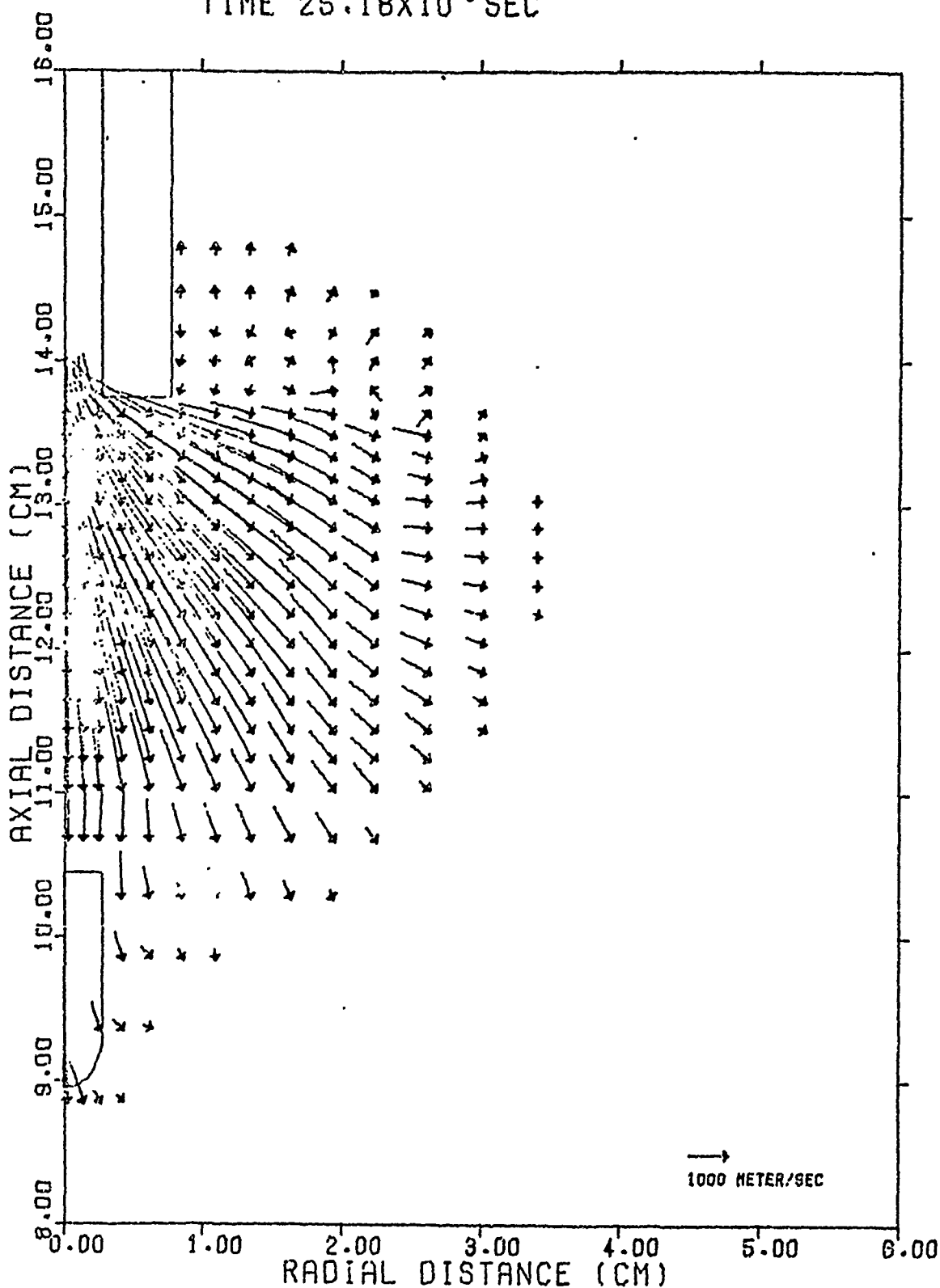


FIGURE 18. VELOCITY VECTOR PLOT: M-16 RIFLE

PRESSURE CONTOUR PLOT  
 PROB. NO. 1.0  
 CYCLE 100  
 TIME  $5.91 \times 10^{-8}$  SEC

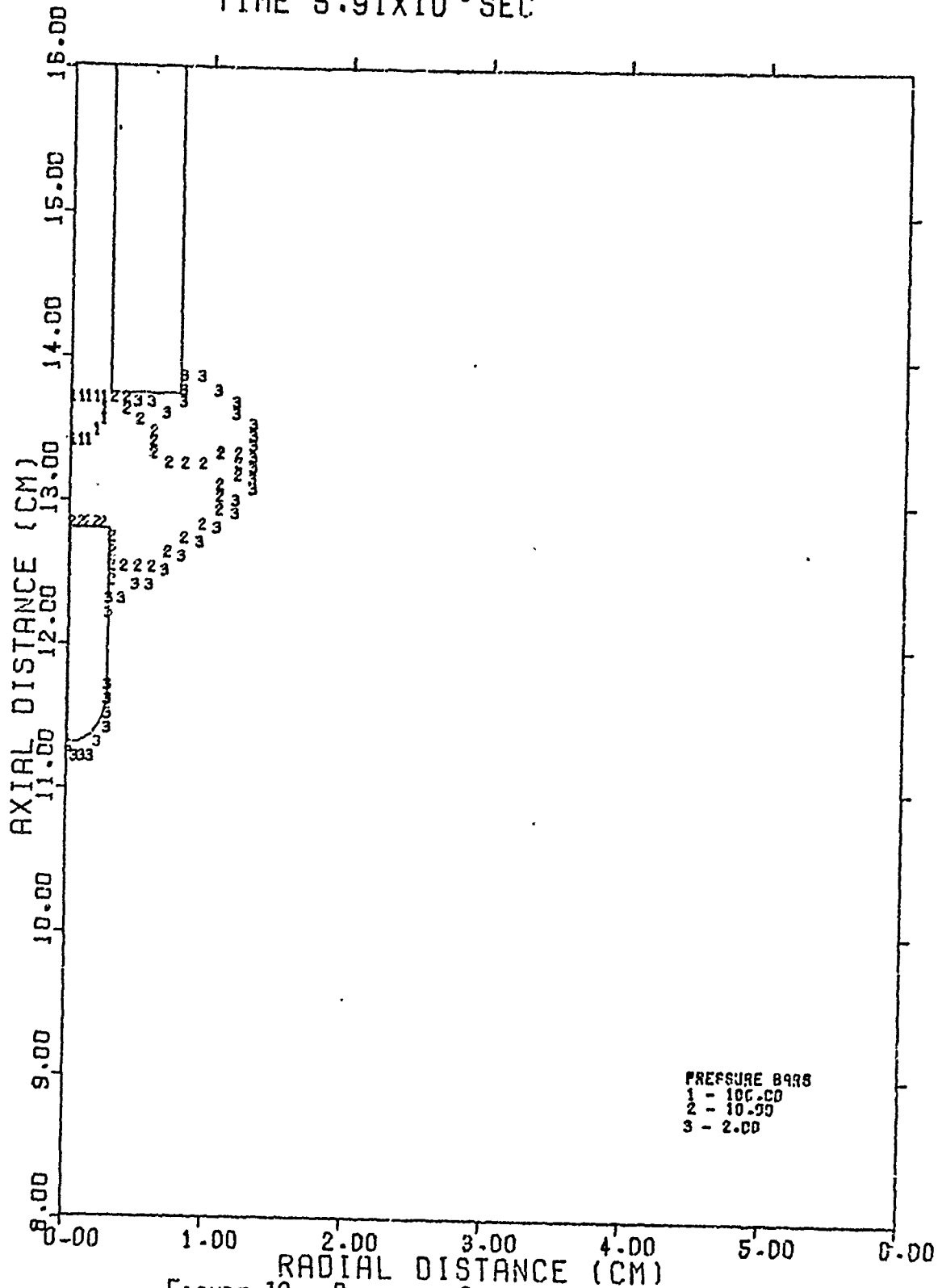


FIGURE 19. PRESSURE CONTOUR PLOT: M-16 RIFLE

PRESSURE CONTOUR PLOT  
 PROB. NO. 1.0  
 CYCLE 200  
 TIME  $10.93 \times 10^{-6}$  SEC

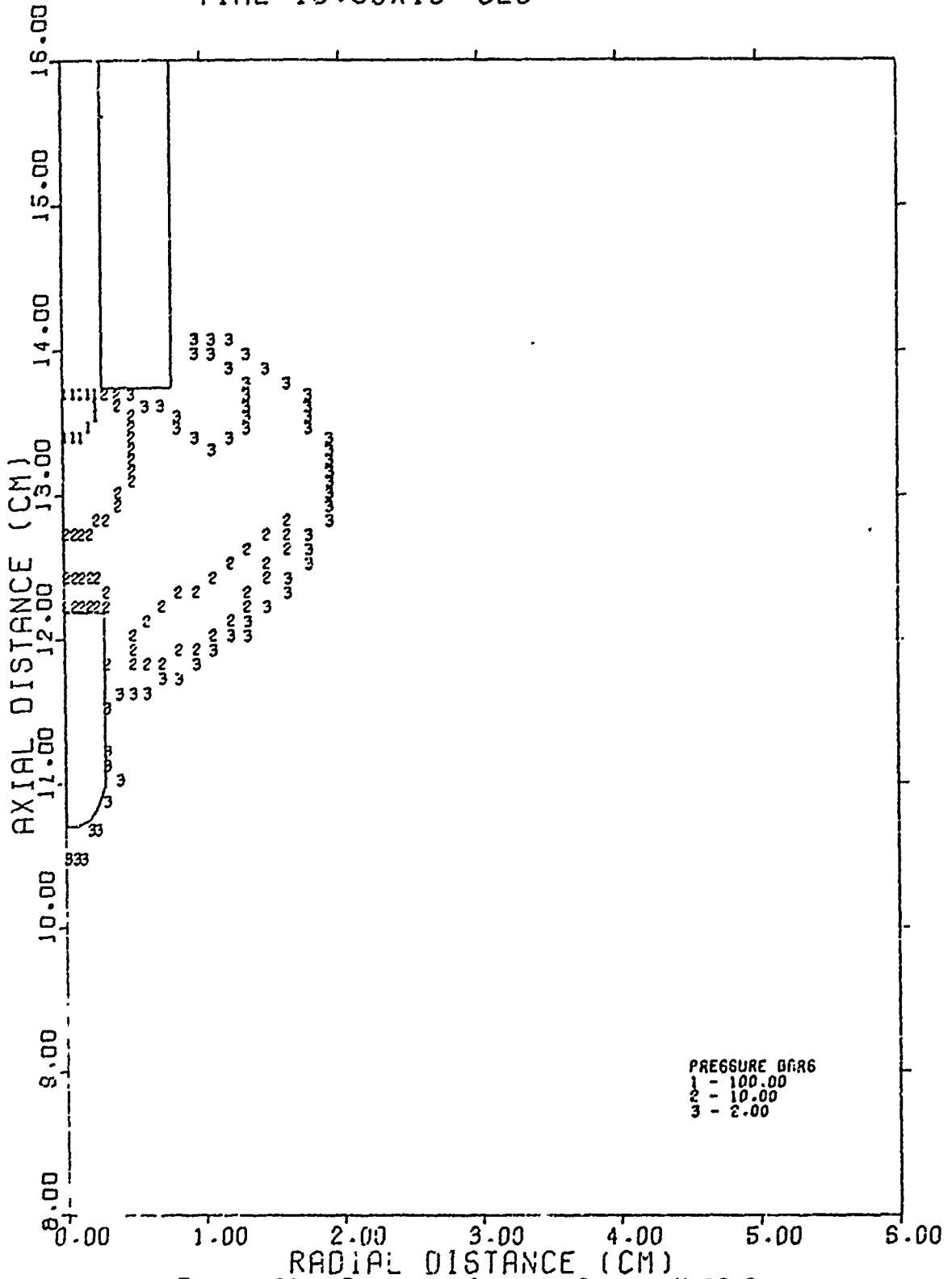


FIGURE 20. PRESSURE CONTOUR PLOT: M-16 RIFLE

PRESSURE CONTOUR PLOT  
 PROB. NO. 1.0  
 CYCLE 300  
 TIME  $15.73 \times 10^{-6}$  SEC

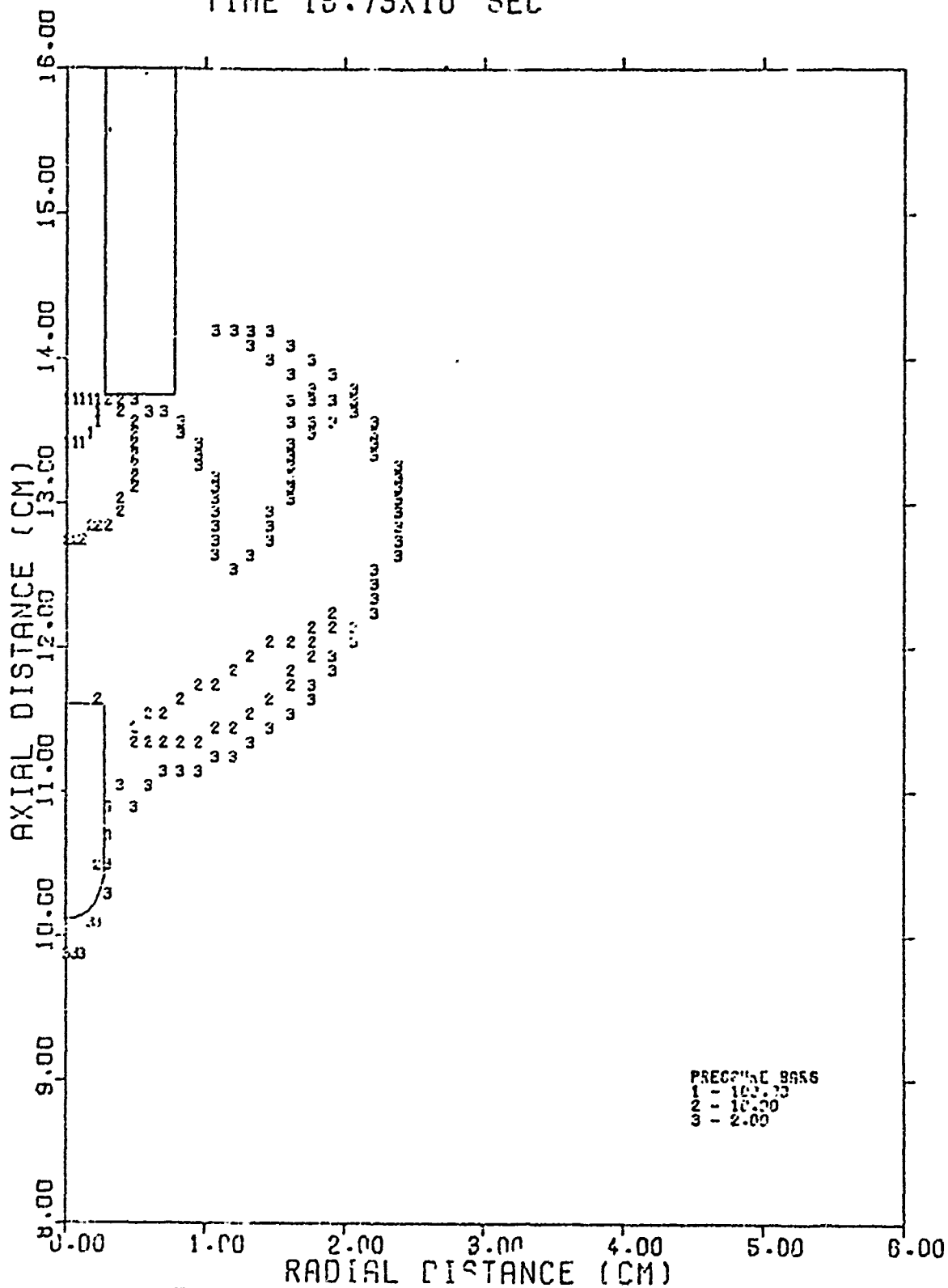


FIGURE 21. PRESSURE CONTOUR PLOT: M-16 RIFLE

PRESSURE CONTOUR PLOT  
 PROB. NO. 1.0  
 CYCLE 400  
 TIME  $20.46 \times 10^{-6}$  SEC

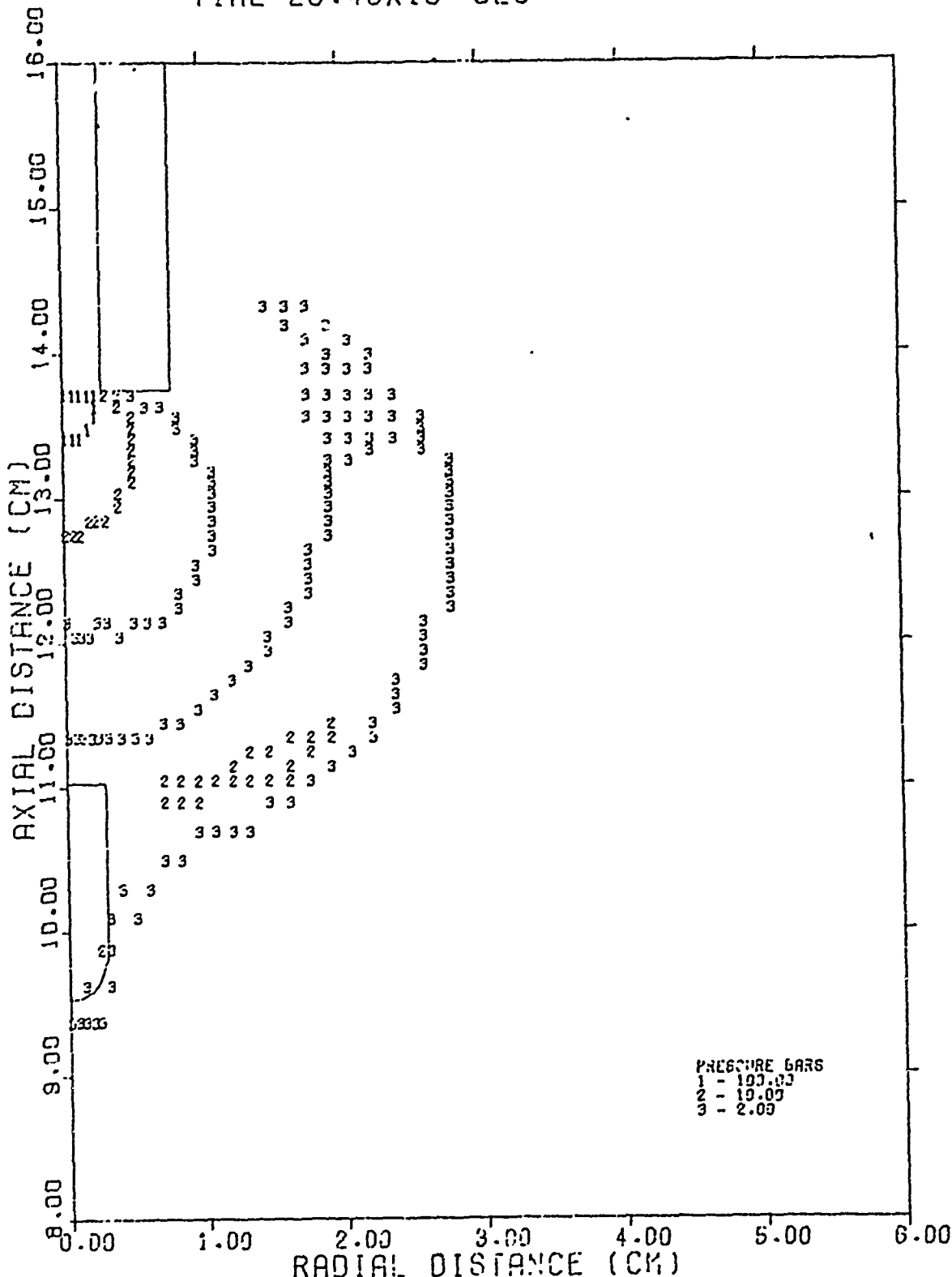


FIGURE 22. PRESSURE CONTOUR PLOT: M-16 RIFLE

PRESSURE CONTOUR PLOT  
 PROB. NO. 1.0  
 CYCLE 500  
 TIME  $25.18 \times 10^{-6}$  SEC

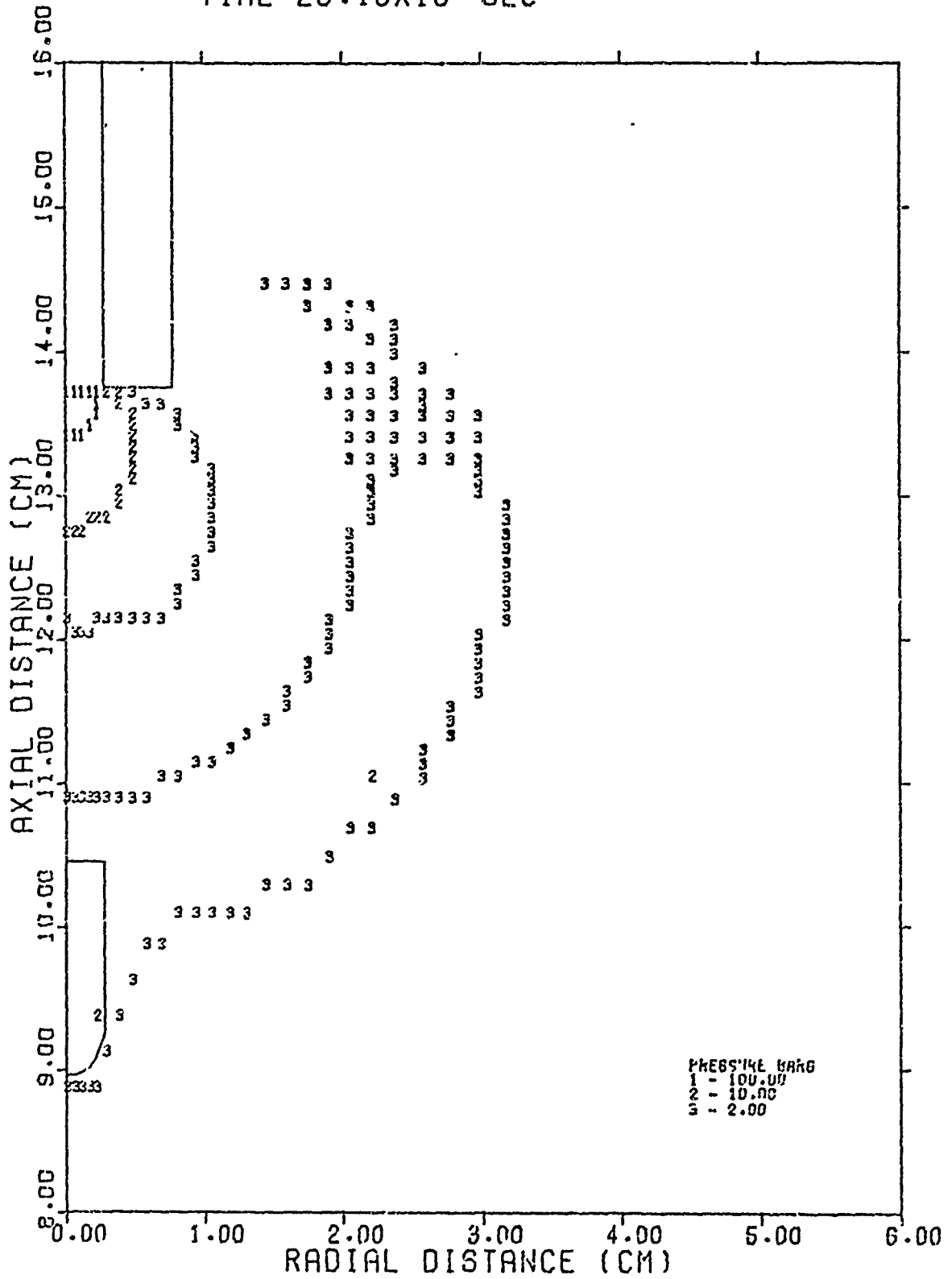


FIGURE 23. PRESSURE CONTOUR PLOT: M-16 RIFLE



DENSITY CONTOUR PLOT.  
PROB. NO. 1.0  
CYCLE 200  
TIME  $10.93 \times 10^{-6}$  SEC

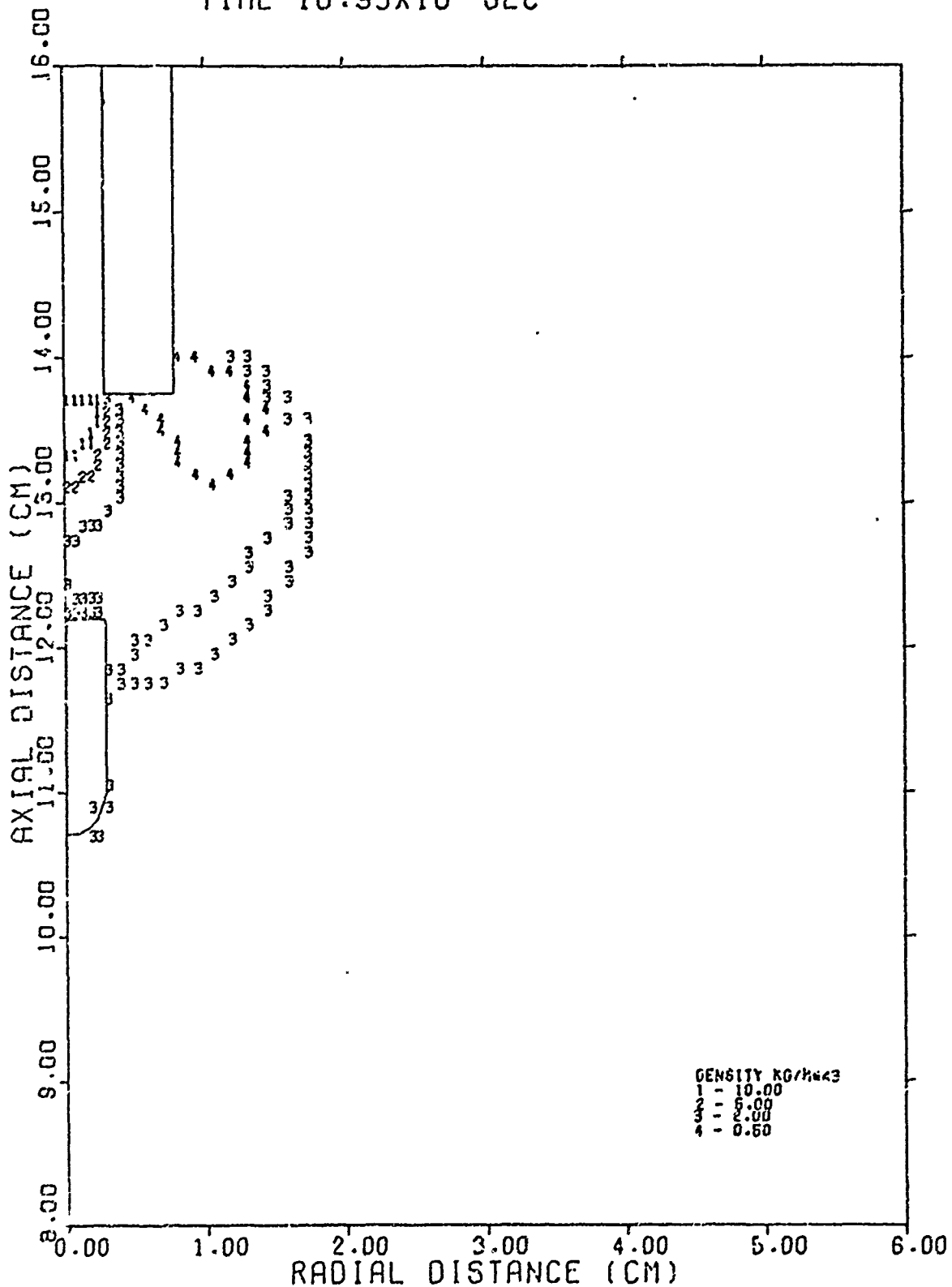


FIGURE 24. DENSITY CONTOUR PLOT: M-16 RIFLE

TEMPERATURE CONTOUR PLOT  
PROB. NO. 1.0  
CYCLE 200  
TIME  $10.93 \times 10^{-6}$  SEC

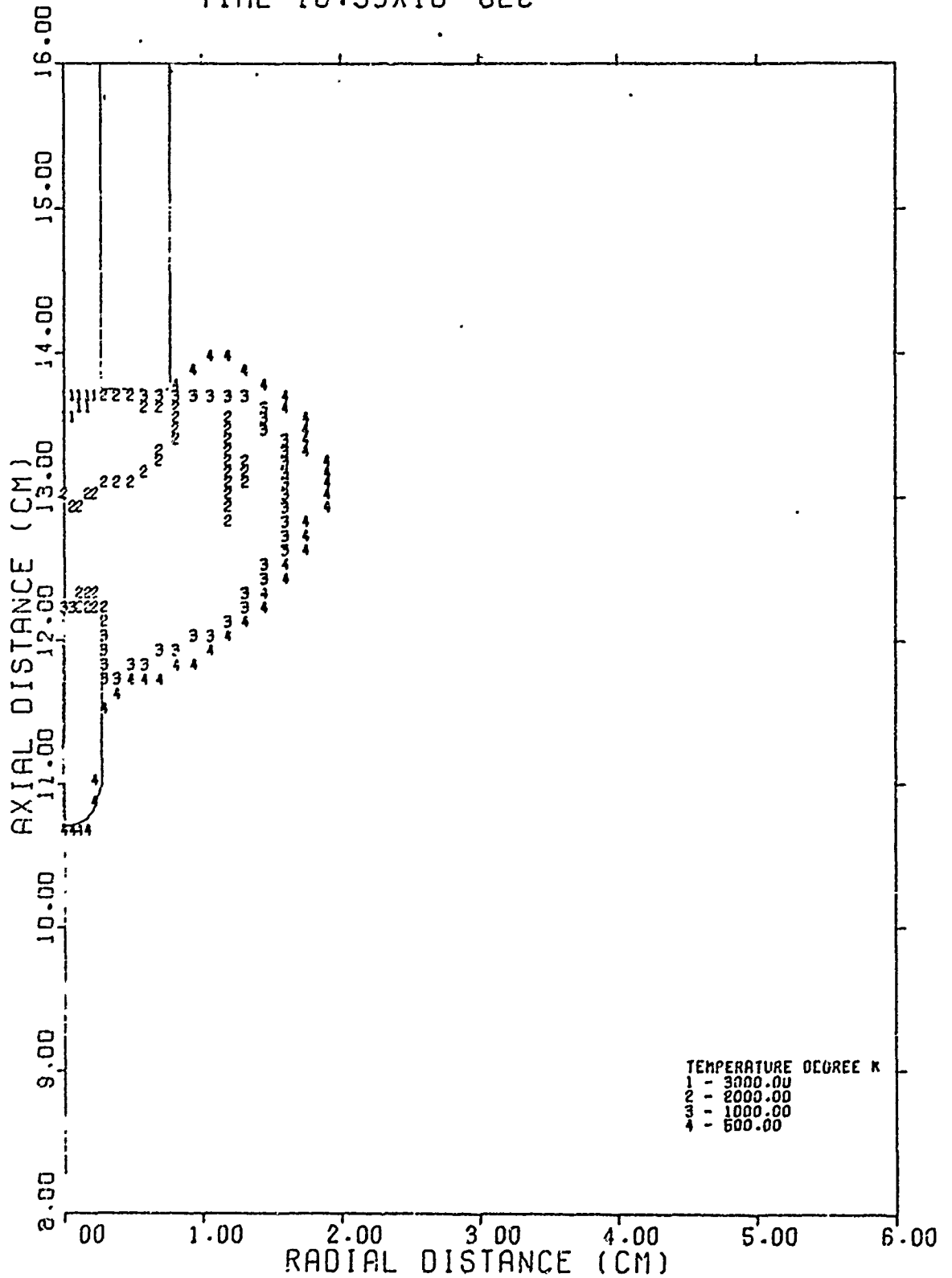


FIGURE 25. TEMPERATURE CONTOUR PLOT: M-16 RIFLE

DENSITY CONTOUR PLOT  
 PROB. NO. 1.0  
 CYCLE 500  
 TIME  $25.18 \times 10^{-6}$  SEC

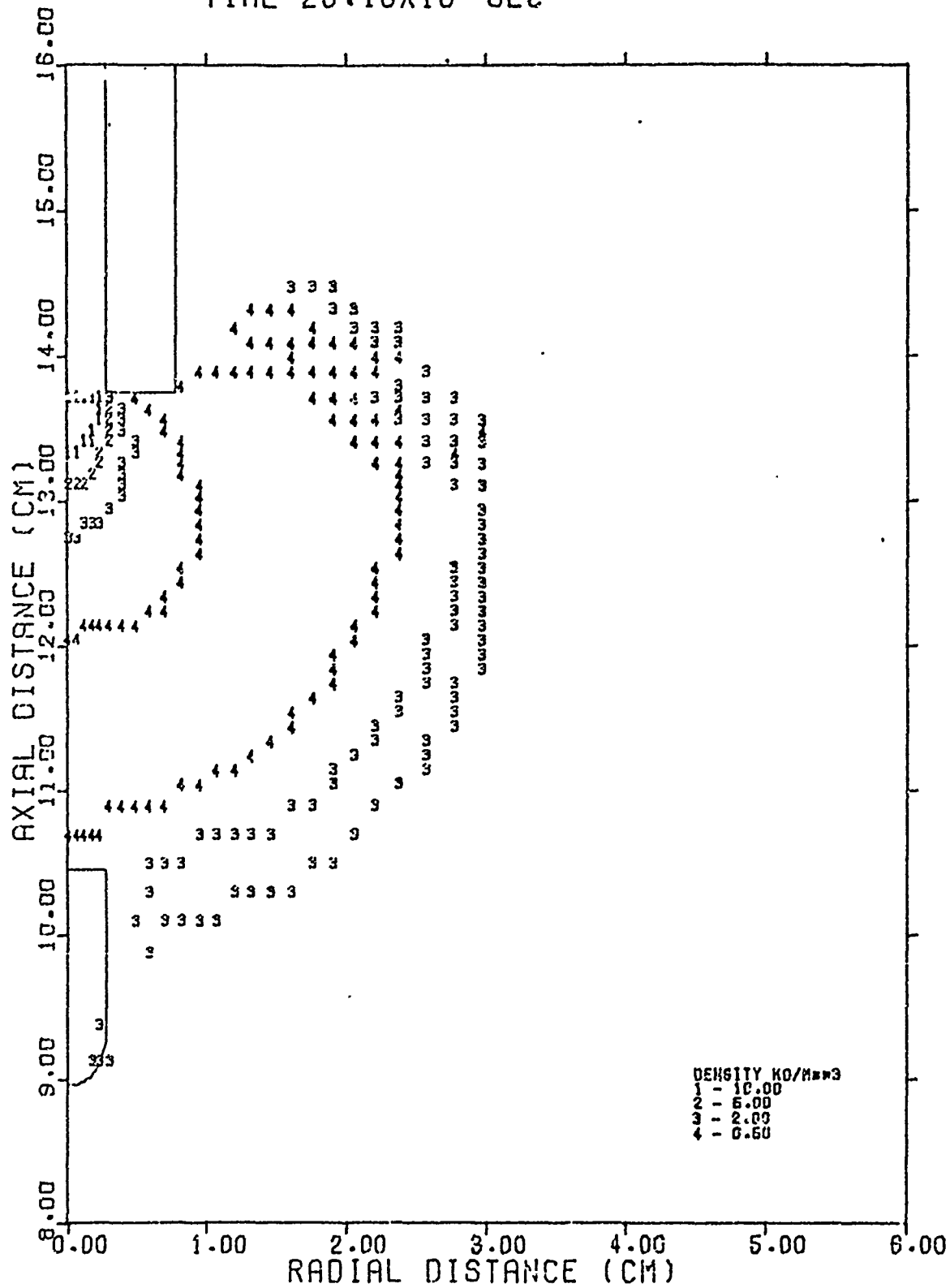


FIGURE 26. DENSITY CONTOUR PLOT: M-16 RIFLE

TEMPERATURE CONTOUR PLOT  
 PROB. 3, 1.0  
 CYCLE 500  
 TIME 25.18X10<sup>-6</sup> SEC

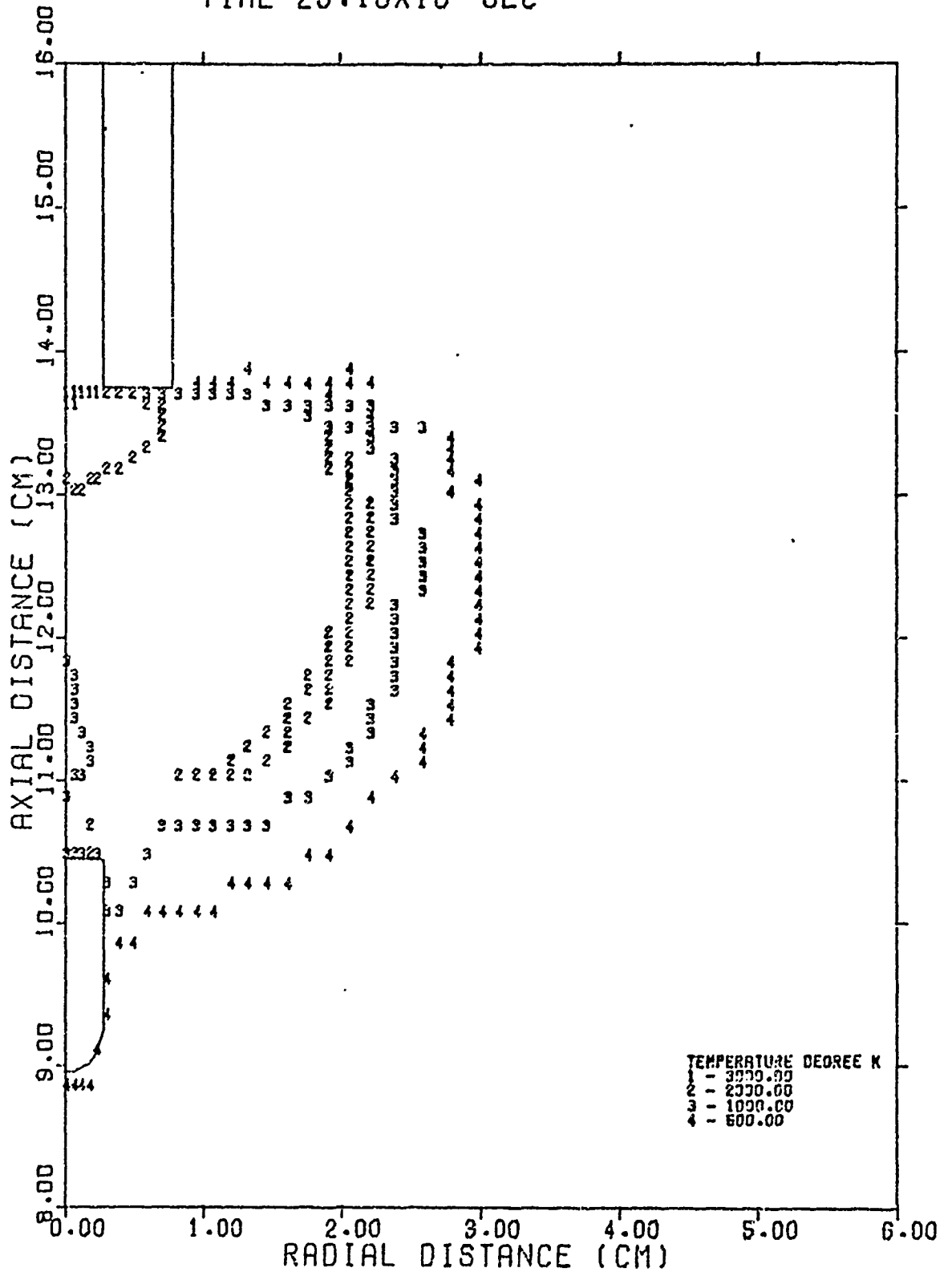


FIGURE 27. TEMPERATURE CONTOUR PLOT: M-16 RIFLE

5.3 M-16 with Simple Muzzle Device

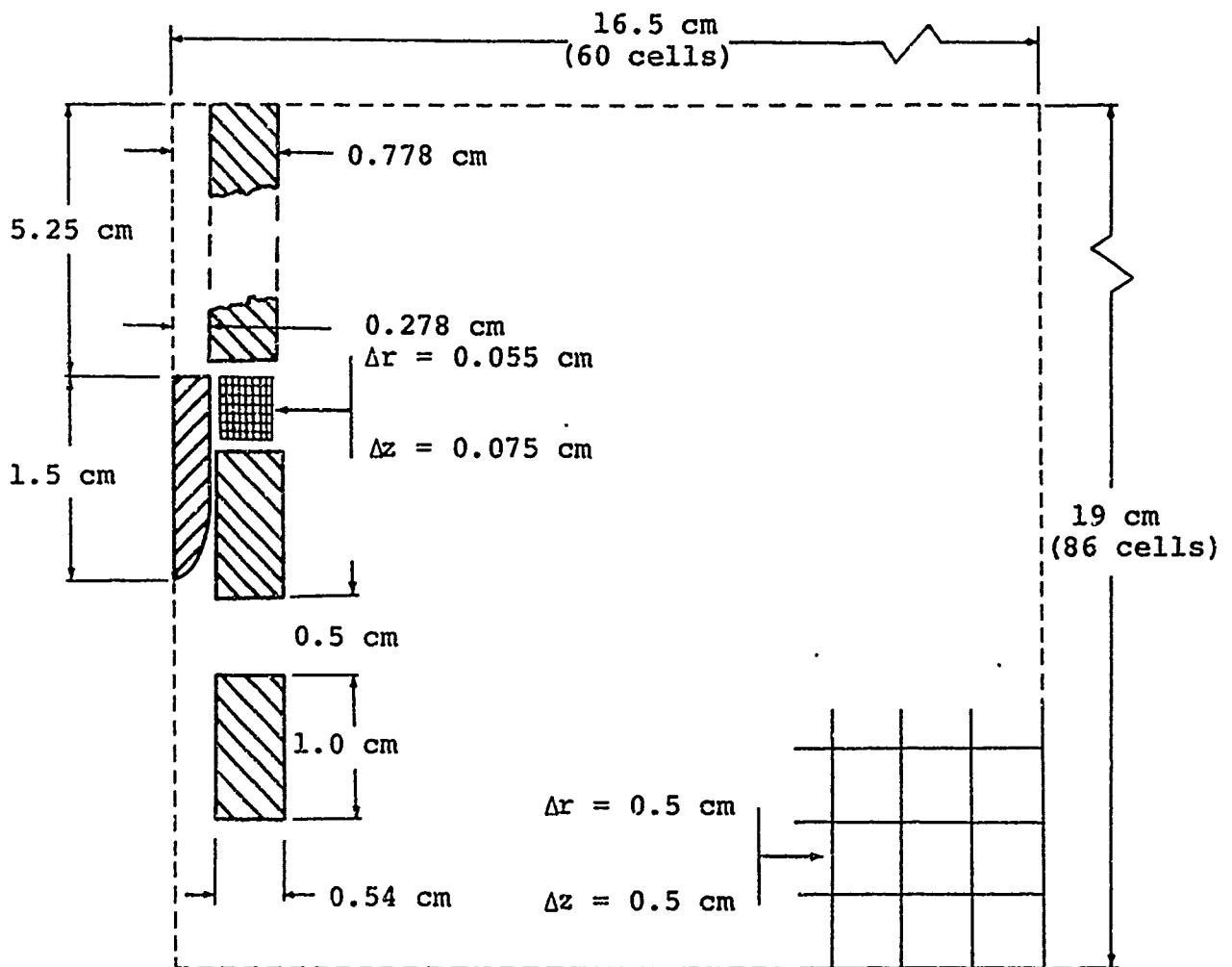


FIGURE 28. SCHEMATIC OF M-16 WITH MUZZLE DEVICE

In this section, the results of a SAMS calculation of the muzzle blast flowfield of an M-16 rifle with a simple muzzle device are presented. The muzzle, muzzle device and projectile geometry and finite difference grid design are shown schematically in Figure 28. The barrel and

projectile are identical to those used in the calculation of the previous section. The muzzle device consists of an extension of the barrel with circumferential slits to permit the flow to expand radially. The equation of state, muzzle jet time history, muzzle velocity and basic finite difference grid, used in this calculation, are identical to those used in the M-16 calculation presented above. The two closed solid boundaries of the muzzle "baffles" were defined by a sequence of fixed beads introduced into the solution field at the positions shown in the figure. The resulting fixed partial cells along the solid boundaries were just slightly smaller than the corresponding rectangular cells in the region.

Computer generated plots of the calculated results are shown in Figures 29 through 42, at the end of this section. Figures 29 through 33 are velocity vector plots of the flowfield at increments of about 5 microseconds ( $\mu$  sec) (every 100 cycles) from  $t = 5.91 \mu$  sec (cycle 100) to  $t = 25.77 \mu$  sec (cycle 500). Figures 34 through 38 are pressure contour plots for corresponding times. Again pressure contours of 2, 10 and 100 bars are plotted. Finally, Figures 39 and 40 are density and temperature contour plots at  $t = 10.95 \mu$  sec and Figures 41 and 42 are the corresponding plots at  $t = 25.77 \mu$  sec.

The figures show the details of the time development of the flow which in this case is much more complicated than the basic M-16 calculation of the previous section. The most notable feature of the flow is the expected strong radial jet of flow between the barrel and the first baffle. The flow is turned by a strong shock resting on the inside corner of the baffle and which extends into the jet and ultimately weakens to a compression, due to its interaction with expansion waves from the corner of the barrel and the outside corner of the baffle. As in the previous calculation, the flow separates at the face of the barrel and also at the outside corner of the baffle. Based on the strong radial diversion of the flow in this calculation as compared to the previous calculation, it is expected that the simple muzzle device used here would significantly decrease recoil forces on the barrel.

The velocity vector plots also show the development of a second radial jet flowing through the space between the first and second baffle. The jet begins to develop at about  $15 \mu$  sec and is considerably weaker than the jet described above. Also of note is the flow inside the muzzle device which is seen to be very close to one dimensional

throughout the calculation. The jet of muzzle gases expands to about 10 bars then recompresses behind the projectile. The flow in the region around the barrel exit and inside the first baffle is shown to be approximately steady from about 15  $\mu$  sec to the end of the calculation. Also of note is the fact that the pressure at the base of the projectile remains above 10 bars throughout the calculation, whereas in the previous calculation the base pressure was less than 10 bars from 15  $\mu$  sec on. Thus the projectile is continuing to accelerate through the muzzle device.

As with the previous results, the results of this calculation are physically reasonable and numerically smooth with the exception of the localized flow oscillations which develop in the same region (mixing layer at barrel exit) as described in Section 5.2. A particularly pleasing result is the flow around the baffles which again is physically reasonable and numerically smooth. This provides some evidence that the treatment of fixed solid boundaries, developed in this study, is accurate. Finally, it is noted that the present calculation was also performed in less than 16 minutes of CPU time on a CDC 6600.

VELOCITY VECTOR PLOT  
PROB. NO. 2.0  
CYCLE 100  
TIME  $5.91 \times 10^{-8}$  SEC

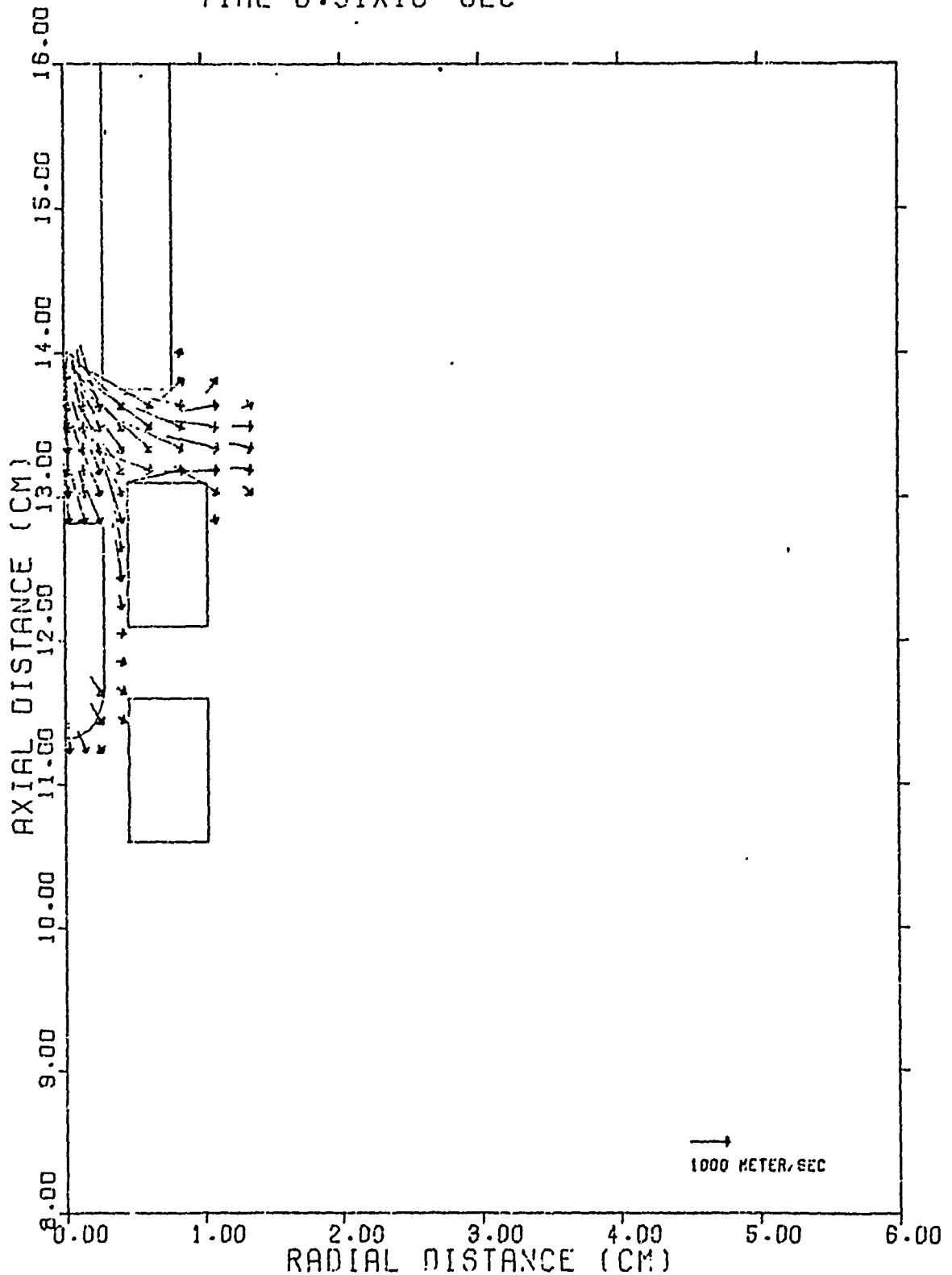


FIGURE 29. VELOCITY VECTOR PLOT: M-16 RIFLE WITH MUZZLE DEVICE



VELOCITY VECTOR PLOT  
PROB. NO. 2.0  
CYCLE 200  
TIME  $10.95 \times 10^{-8}$  SEC

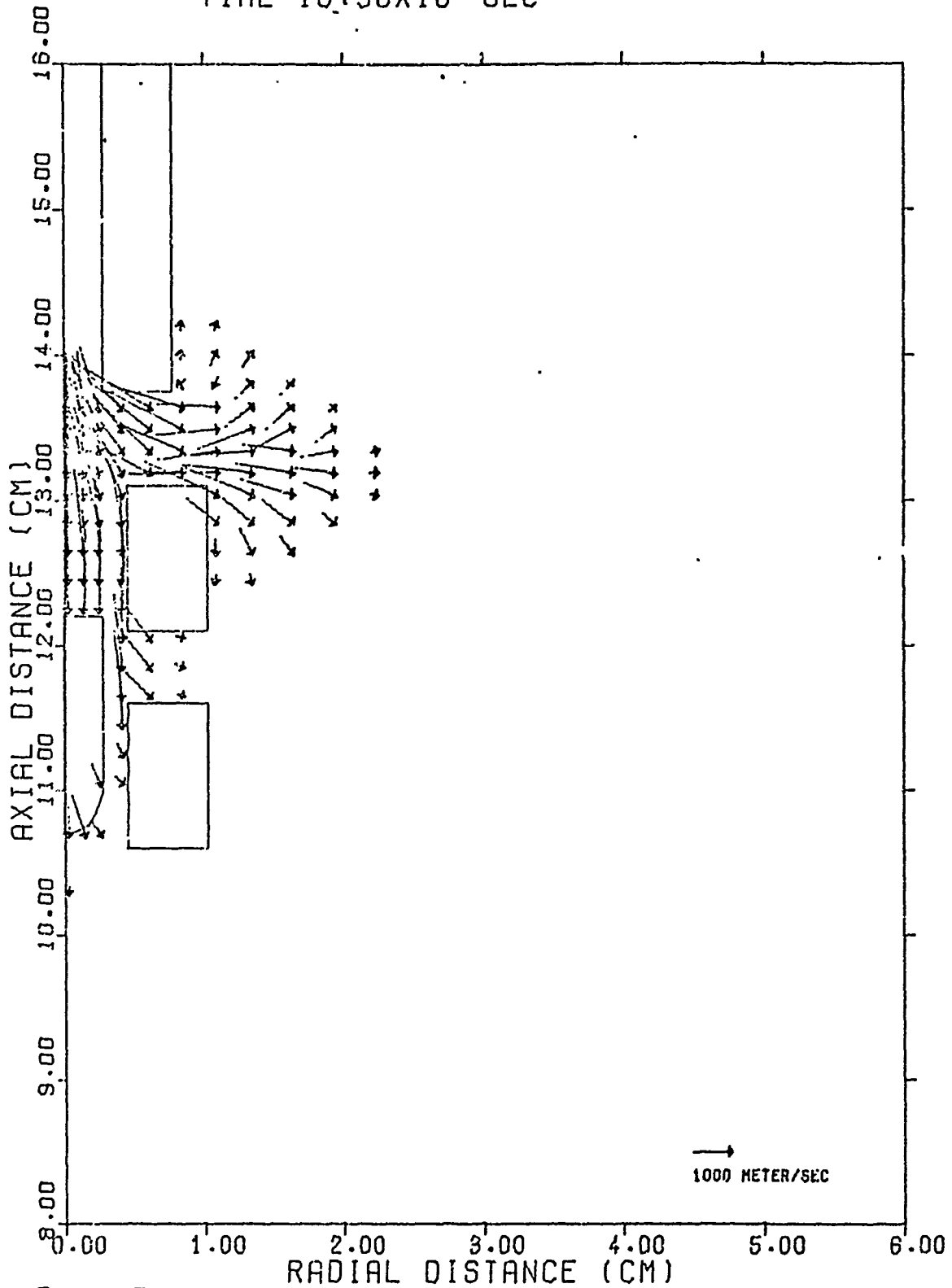


FIGURE 30. VELOCITY VECTOR PLOT: M-16 RIFLE WITH MUZZLE DEVICE

VELOCITY VECTOR PLOT  
PROB. NO. 2.0  
CYCLE 300  
TIME  $15.87 \times 10^{-6}$  SEC

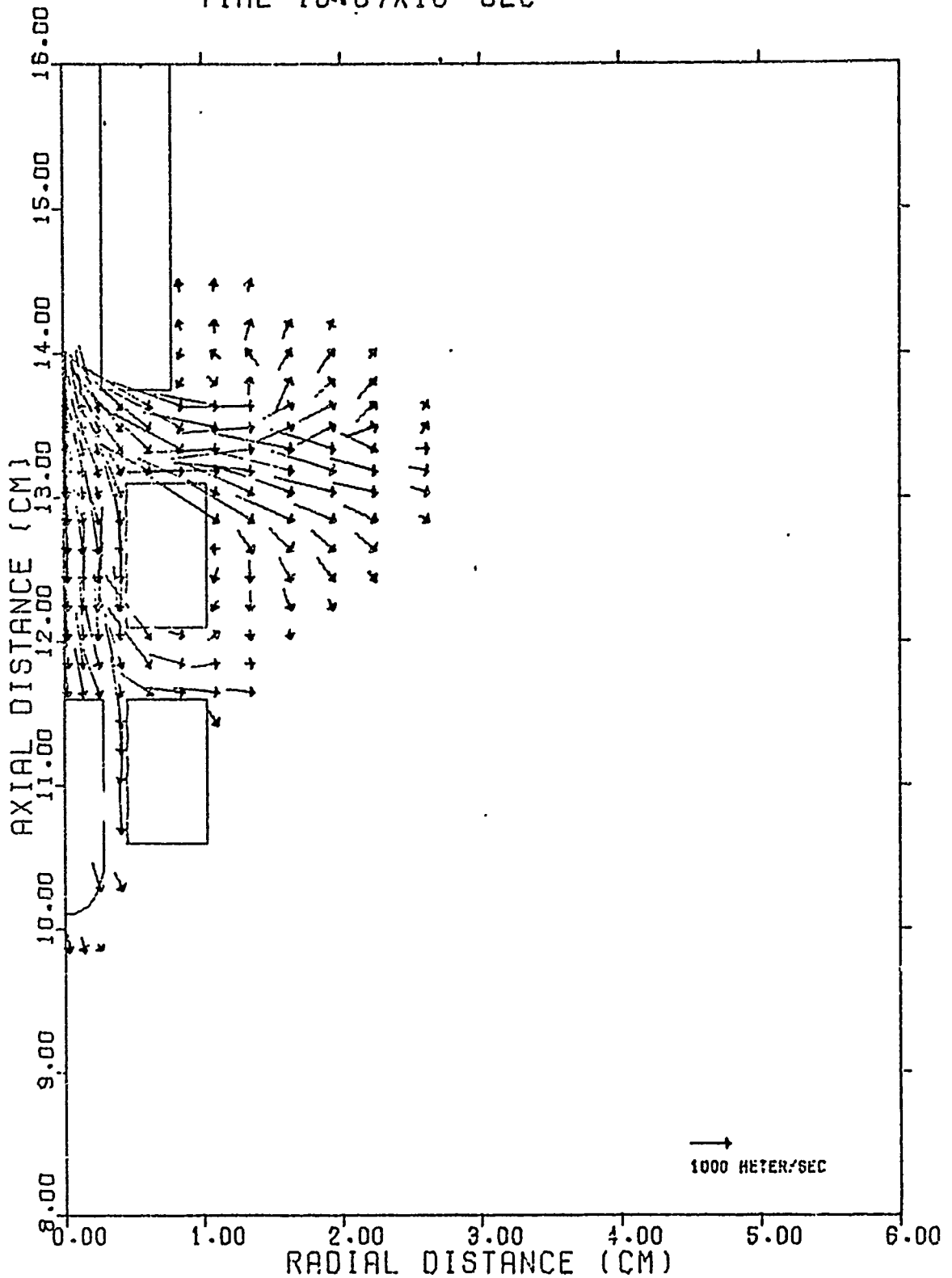


FIGURE 31. VELOCITY VECTOR PLOT: M-16 RIFLE WITH MUZZLE DEVICE

VELOCITY VECTOR PLOT  
PROB. NO. 2.0  
CYCLE 400  
TIME  $20.81 \times 10^{-6}$  SEC

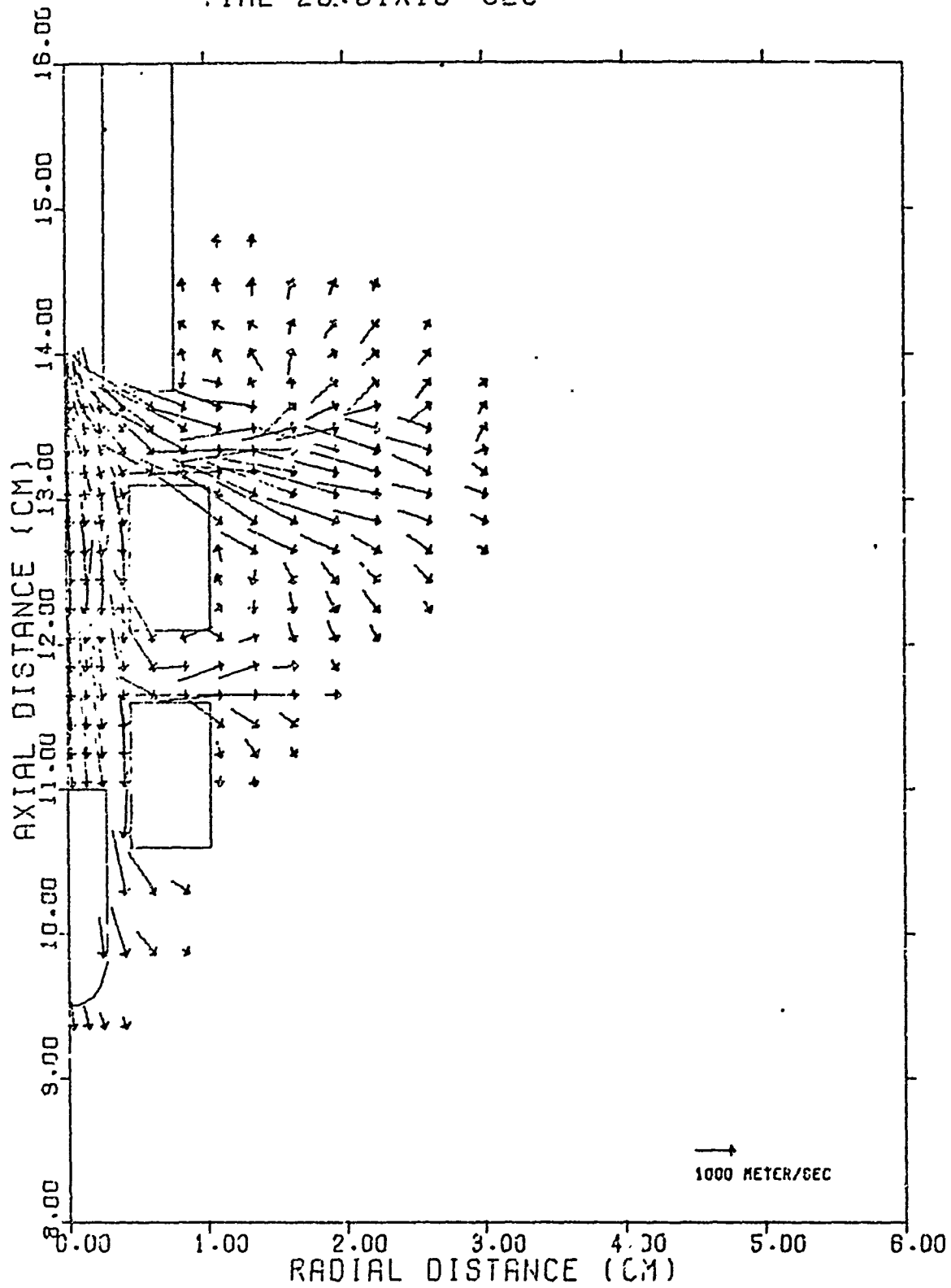


FIGURE 32. VELOCITY VECTOR PLOT: M-16 RIFLE WITH MUZZLE DEVICE

VELOCITY VECTOR PLOT  
PROB. NO. 2.0  
CYCLE 500  
TIME  $25.77 \times 10^{-8}$  SEC

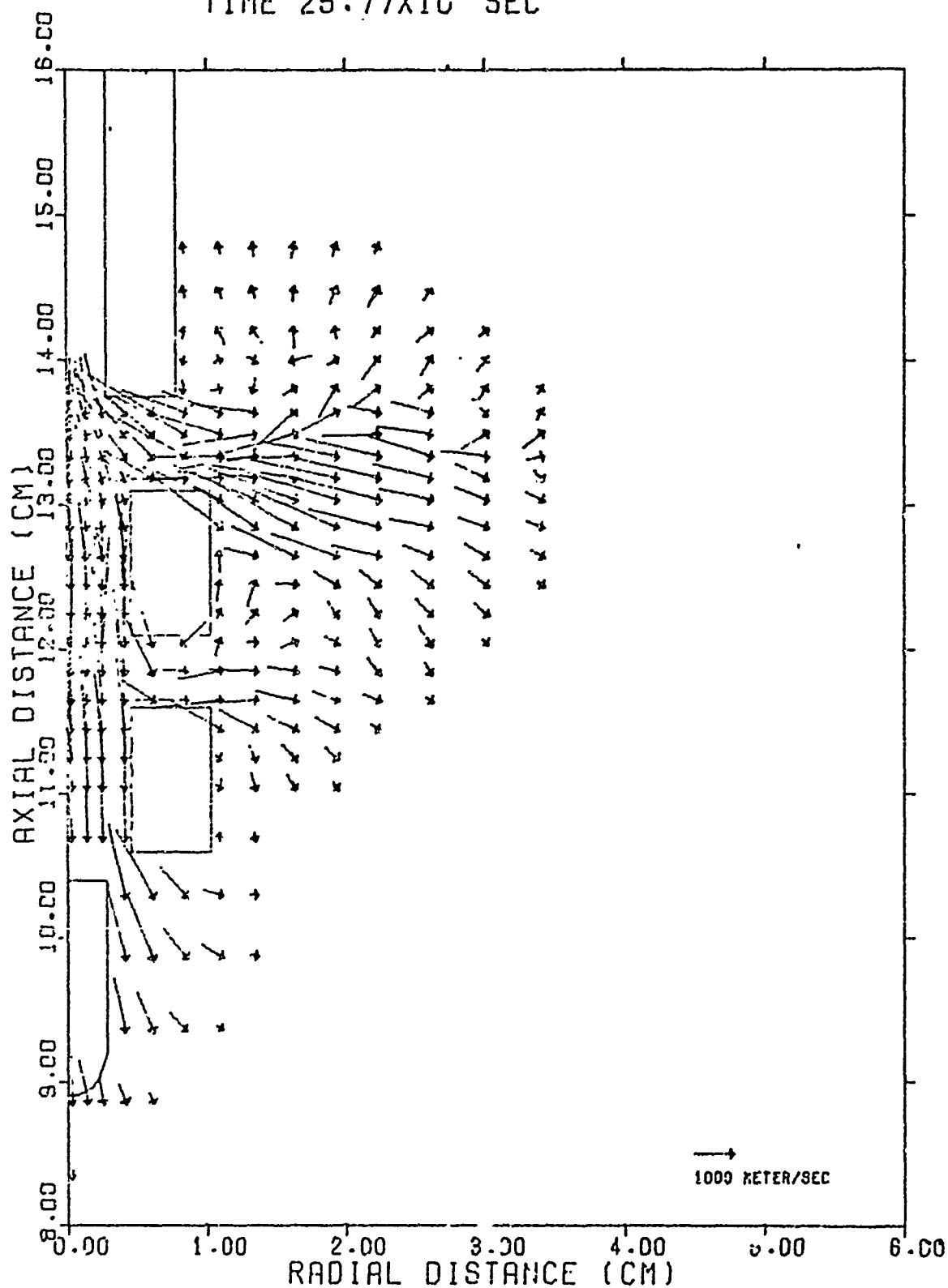


FIGURE 33. VELOCITY VECTOR PLOT: M-16 RIFLE WITH MUZZLE DEVICE

PRESSURE CONTOUR PLOT  
 PROB. NO. 2.0  
 CYCLE 100  
 TIME  $5.91 \times 10^{-6}$  SEC

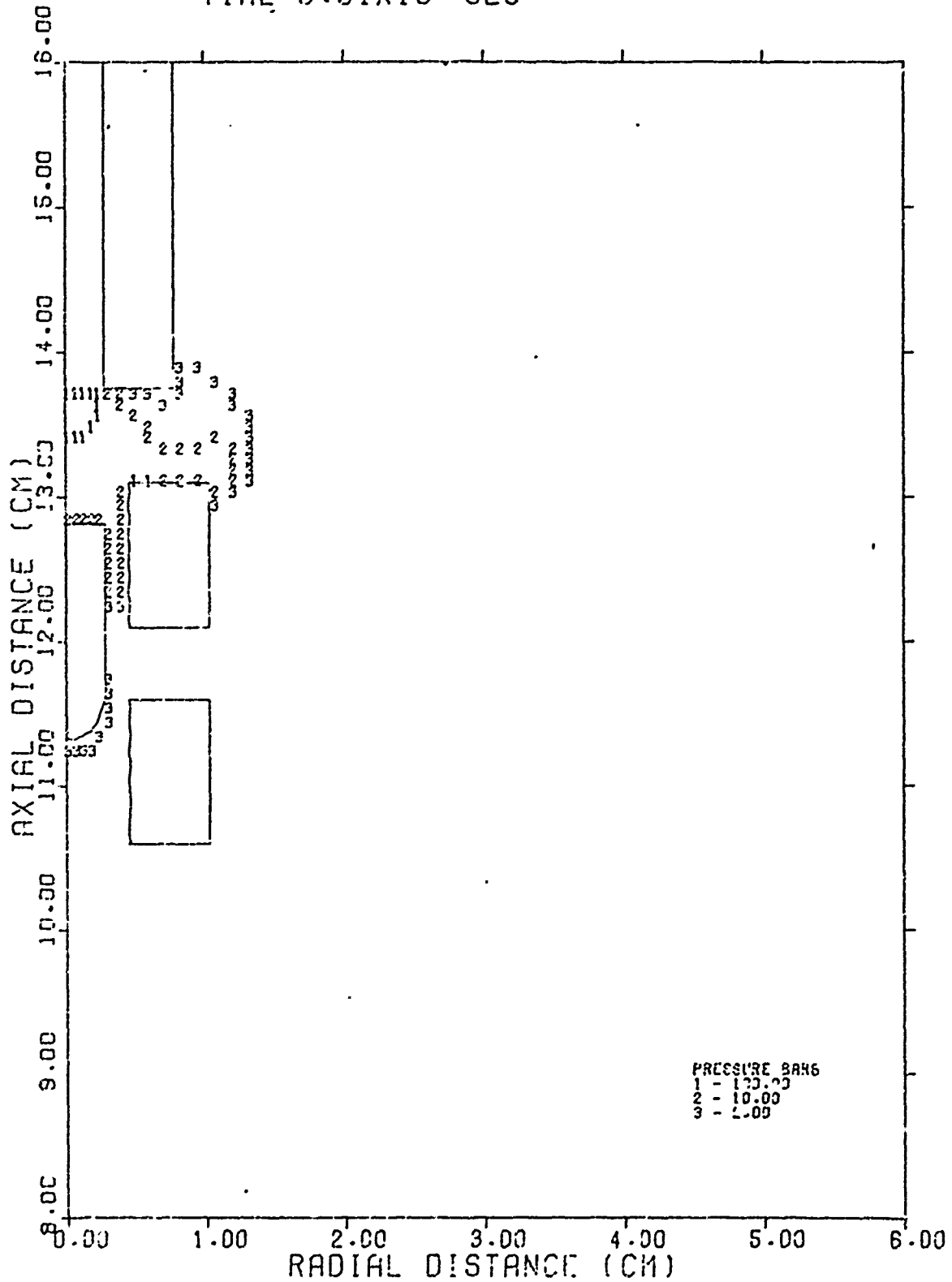


FIGURE 34. PRESSURE CONTOUR PLOT: M-16 RIFLE WITH MUZZLE DEVICE

PRESSURE CONTOUR PLOT  
 PROB. NO. 2.0  
 CYCLE 200  
 TIME  $10.95 \times 10^{-6}$  SEC

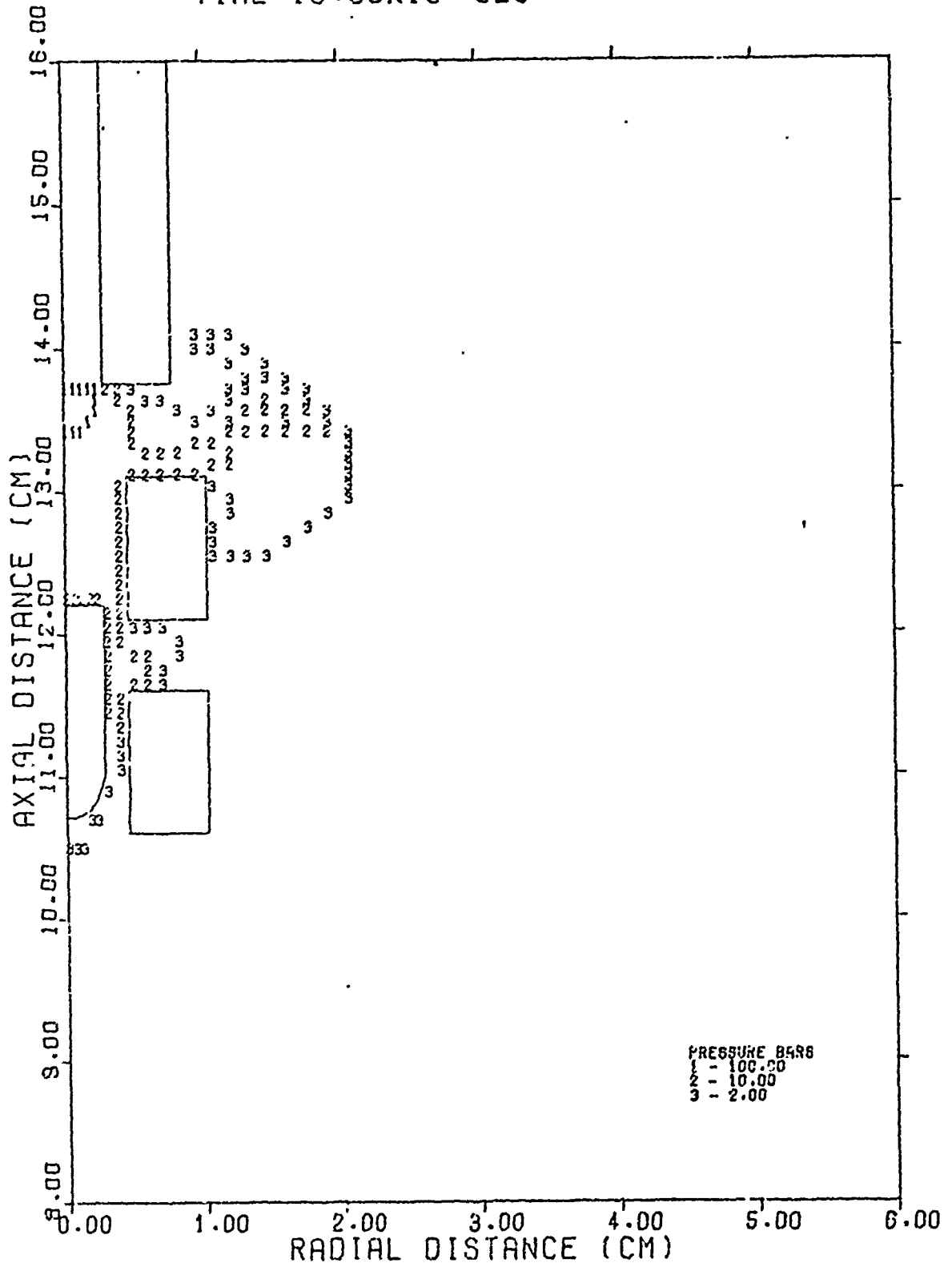


FIGURE 35. PRESSURE CONTOUR PLOT: M-16 RIFLE WITH MUZZLE DEVICE

PRESSURE CONTOUR PLOT  
 PROB. NO. 2.0  
 CYCLE 300  
 TIME  $15.87 \times 10^{-6}$  SEC

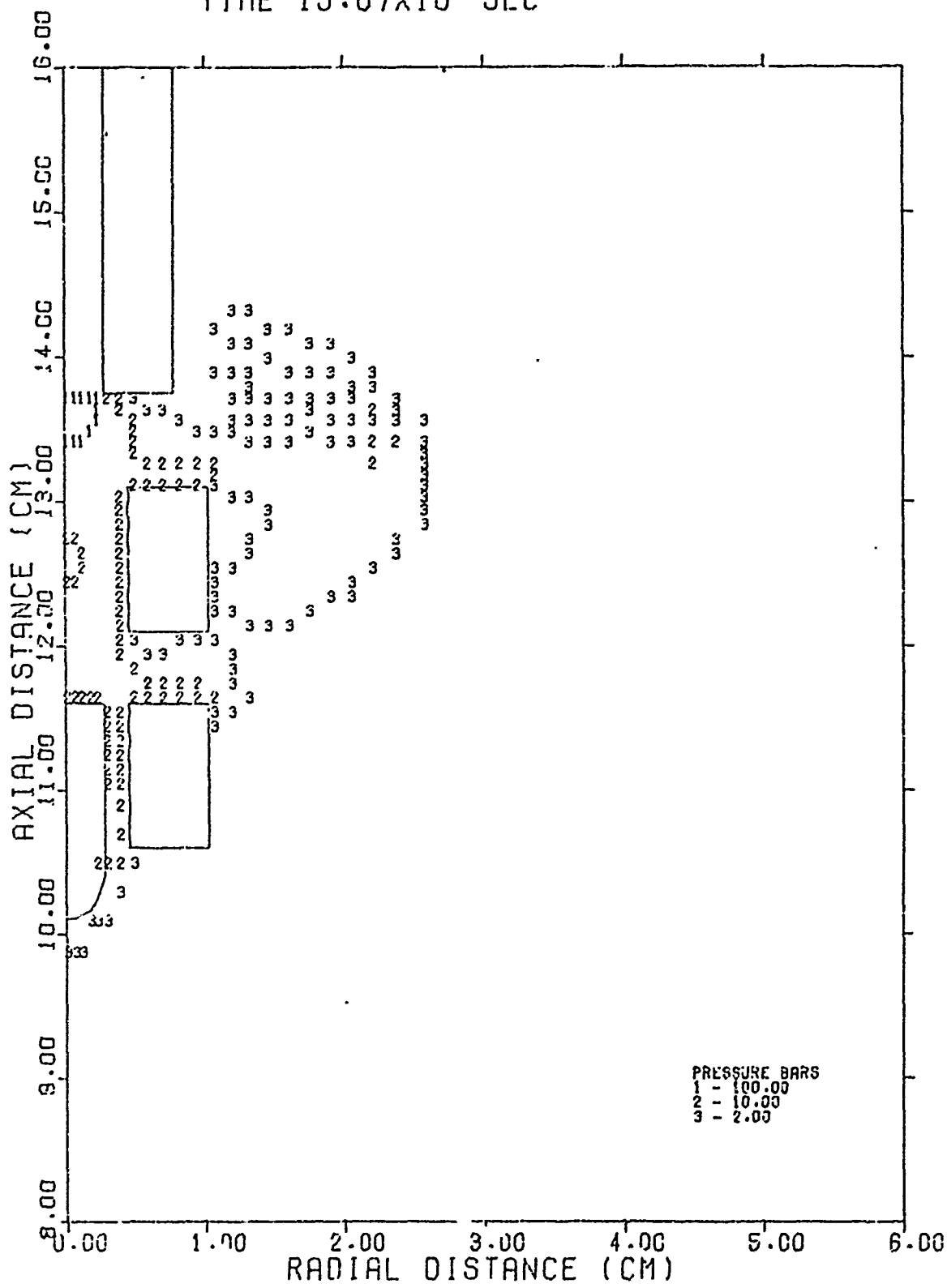


FIGURE 35. PRESSURE CONTOUR PLOT: M-16 RIFLE WITH MUZZLE DEVICE

PRESSURE CONTOUR PLOT  
 PROB. NO. 2.0  
 CYCLE 400  
 TIME  $20.81 \times 10^{-8}$  SEC

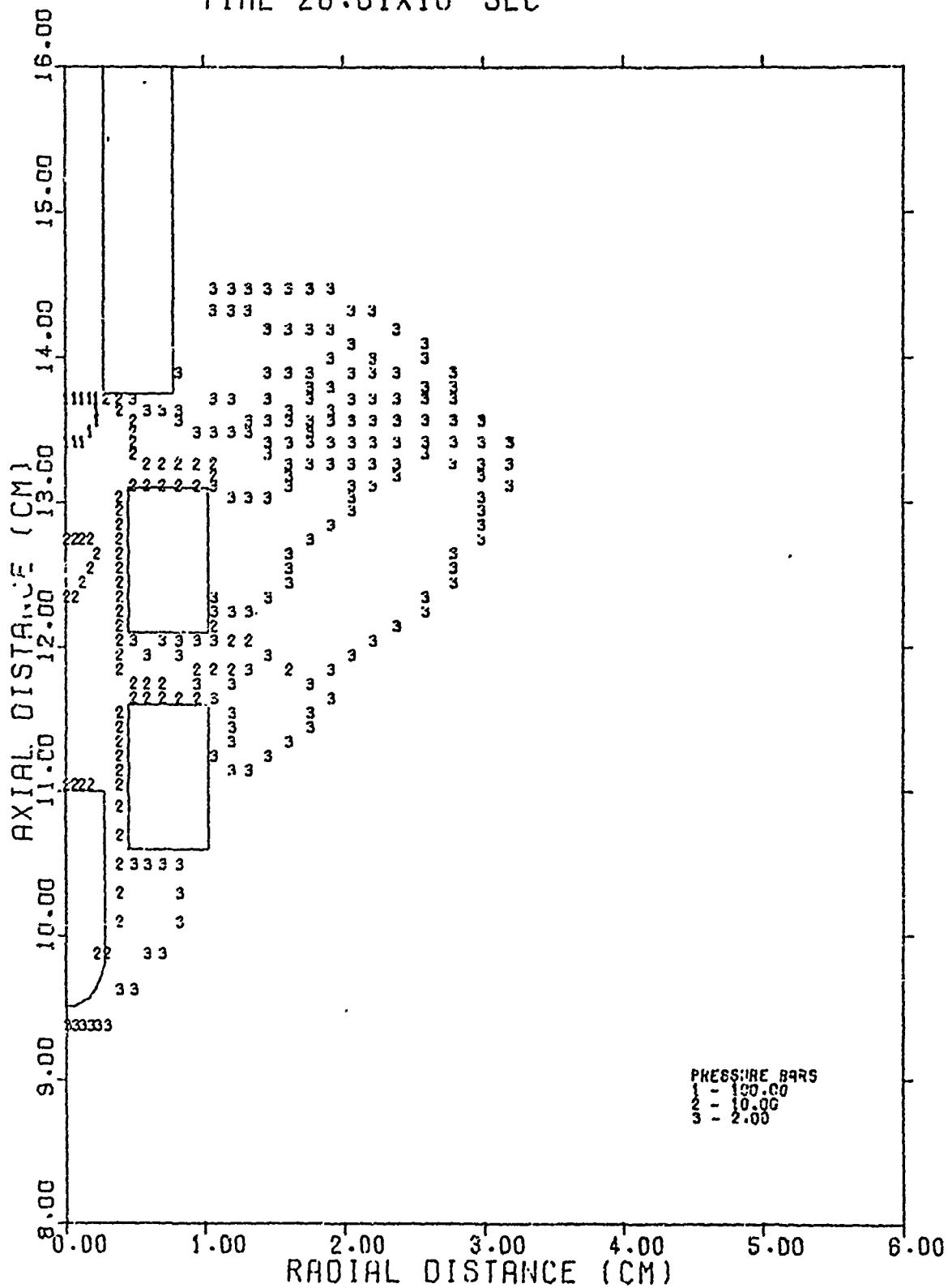


FIGURE 37. PRESSURE CONTOUR PLOT: M-16 RIFLE WITH MUZZLE DEVICE



FRESSURE CONTOUR PLOT  
 PROB. NO. 2.0  
 CYCLE 500  
 TIME 25.77X10<sup>-8</sup> SEC

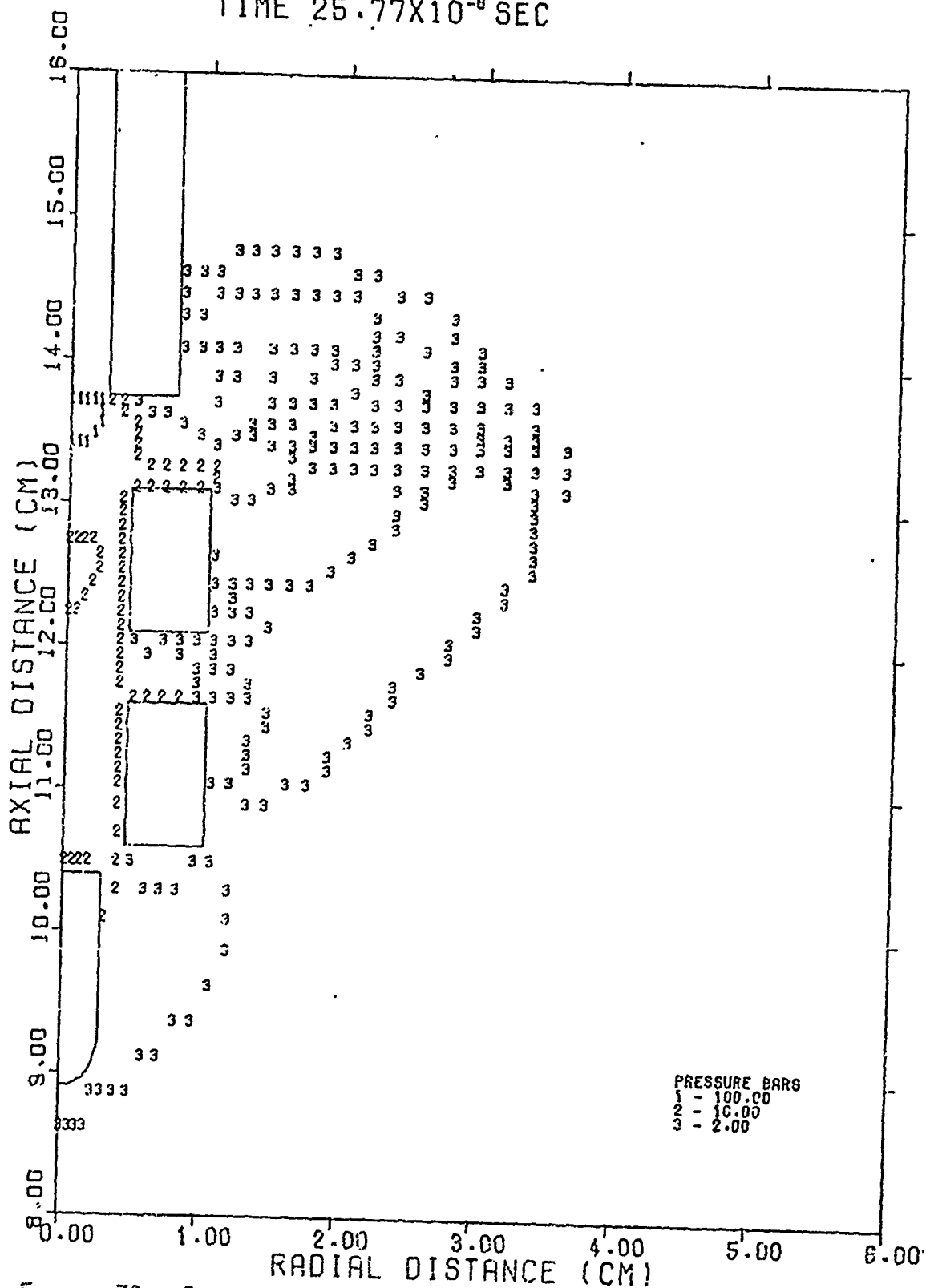


FIGURE 38. PRESSURE CONTOUR PLOT: M-16 RIFLE WITH MUZZLE DEVICE

DENSITY CONTOUR PLOT  
 PROB. NO. 2.0  
 CYCLE 200  
 TIME  $10.95 \times 10^{-6}$  SEC

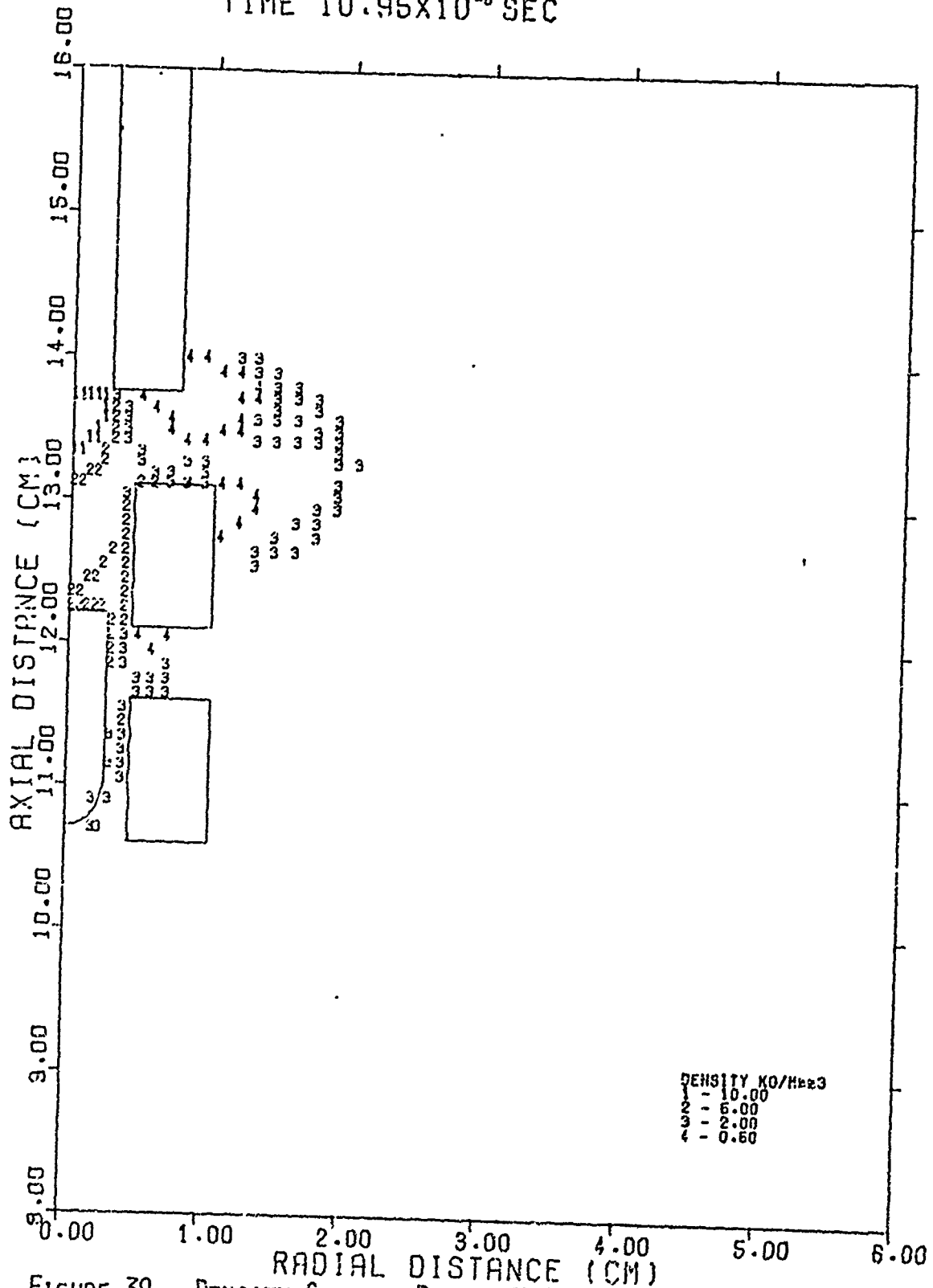


FIGURE 39. DENSITY CONTOUR PLOT: M-16 RIFLE WITH MUZZLE DEVICE

TEMPERATURE CONTOUR PLOT  
 PROB. NO. 2.0  
 CYCLE 200  
 TIME  $10.95 \times 10^{-6}$  SEC

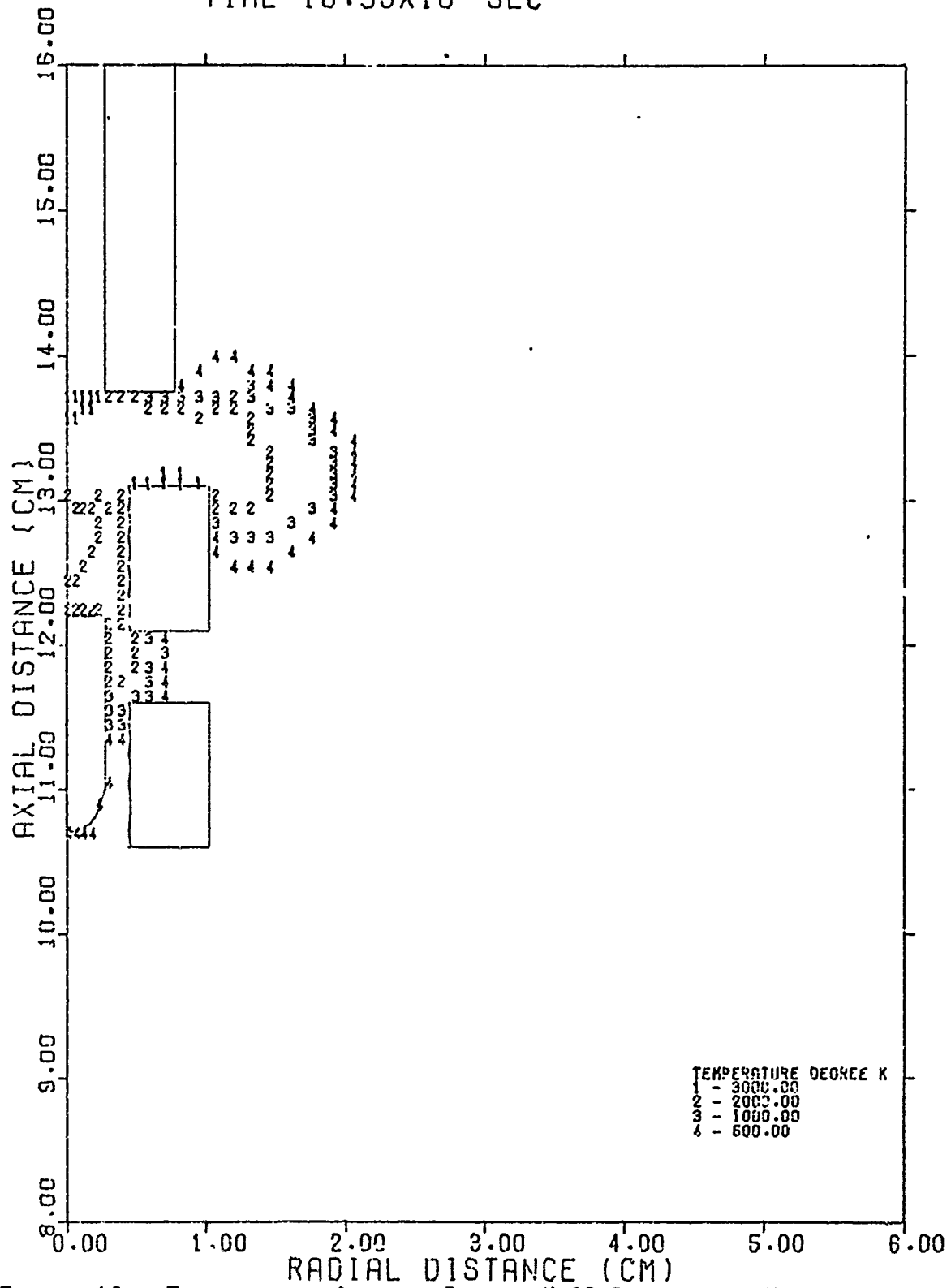


FIGURE 40. TEMPERATURE CONTOUR PLOT: M-16 RIFLE WITH MUZZLE DEVICE

DENSITY CONTOUR PLOT  
 PROB. NO. 2.0  
 CYCLE 500  
 TIME  $25.77 \times 10^{-8}$  SEC

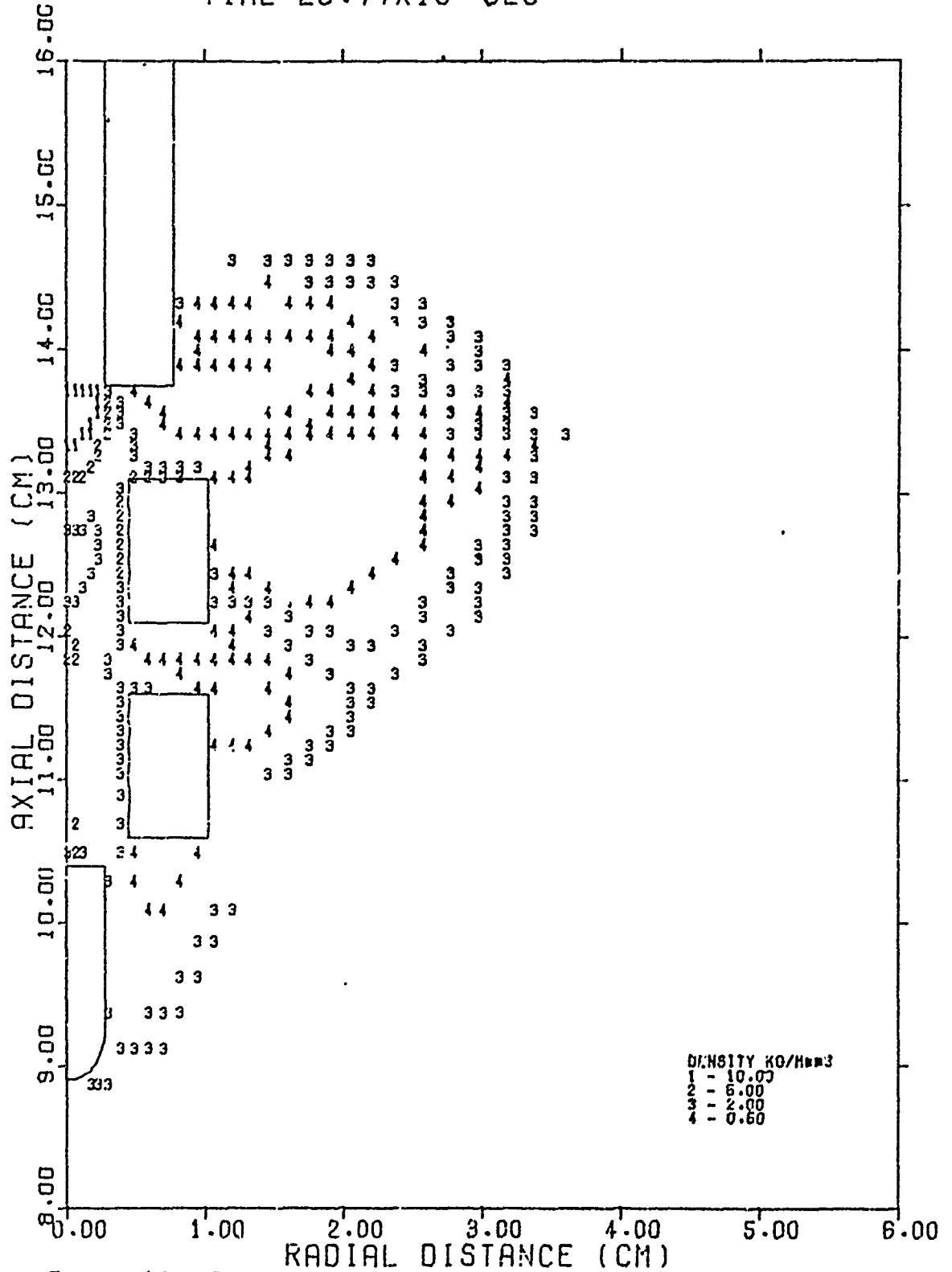


FIGURE 41. DENSITY CONTOUR PLOT: M-16 RIFLE WITH MUZZLE DEVICE

TEMPERATURE CONTOUR PLOT  
 PROB. NO. 2.0  
 CYCLE 500  
 TIME 25.77X10<sup>-6</sup> SEC

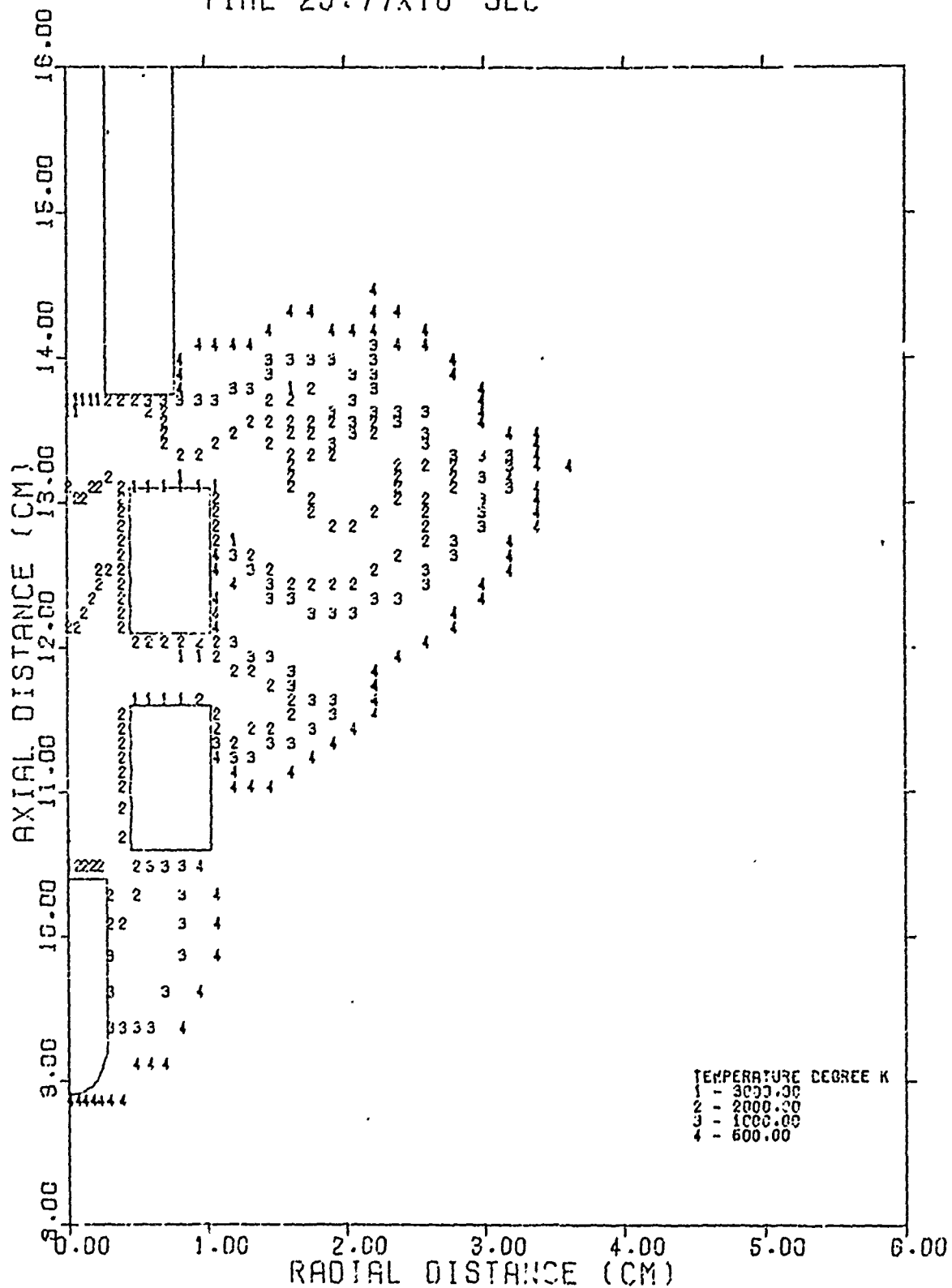


FIGURE 42. TEMPERATURE CONTOUR PLOT: M-16 RIFLE WITH MUZZLE DEVICE

## 6.0 CONCLUSIONS AND RECOMMENDATIONS

The main result of this study is the generalization of the fluid-in-cell finite difference technique to account for arbitrary fixed and moving boundaries in the Eulerian grid. The technique has been developed in general but applied specifically to the muzzle blast flowfield problem in the SAMS computer program. The results presented in this report indicate that the treatment of fixed and moving boundaries is valid and that the overall numerical technique is a good approach to the simulation of muzzle blast flowfields which include a moving projectile and fixed muzzle device boundary. The results indicate that the SAMS code could be a useful tool for muzzle device studies since it is relatively easy to set up and run and it makes relatively efficient use of computer time. Useful muzzle flow simulations can be performed in approximately 15 minutes of CPU time on a CDC 6600.

The numerical technique developed during the study could be improved in a number of ways, some of which have been mentioned in previous sections. For example, the treatment of boundary conditions could be improved. The displaced center of mass of the partial boundary cells could be accounted for in the Lagrangian phase of the computational cycle and also in extrapolating flow quantities to the solid boundary. Also an improved treatment of the farfield boundaries to absorb the air shock and trailing flow with minimum reflection would allow moving the computational boundaries closer to the muzzle. This would result in more accurate resolution of the flow in the muzzle device, through an increased concentration of grid points near the muzzle. In a related vein, the accuracy, stability and efficiency of the overall numerical technique should be investigated to a greater degree than was possible in this study. Accuracy could be verified by comparison to experimental data or exact solutions for special cases (1-D projectile motion, etc.). The stability of the technique could be enhanced by the use of an artificial viscosity to damp out flow oscillations such as those which develop in the unstable mixing layer discussed in the test case calculations. Finally, the efficiency of the numerical technique for application to muzzle blast problems could be "fine tuned" through more extensive experimentation with grid spacing and distribution and Courant numbers. All of the above developments would require numerical experimentation to optimize and build confidence in the numerical technique.

Certain generalizations to the present technique would both enhance the simulation and permit the study of more detailed phenomena. As noted in Section 4.1, the present single equation of state can be made quite accurate for describing both the muzzle gas and air. However, the addition of a two equation of state capability would increase the accuracy and also permit a more detailed study of the mixing of the muzzle gases and air. For modern high velocity weapons, two phase flow effects in the muzzle jet can be quite important. That is, burning propellant particles will very likely accompany the combustion products out of the muzzle. Such effects could be studied by introducing particles into the flow which couple to the flow through mass (products), momentum (drag) and energy (heat deposition) exchange. This could be accomplished to varying degrees of accuracy, as is commonly done in two phase flow computations.

In summary, it is believed that the present numerical technique, incorporated in the SAMS code, can be quite useful in the study of muzzle gas flows. Certain improvements to and generalizations of the technique, discussed here, would enhance both its utility, accuracy and flexibility.

## 7.0 REFERENCES

1. Rich, M., "A Method for Eulerian Fluid Dynamics," Los Alamos Scientific Laboratory Report No. IAMS-2826, Dec. 1962.
2. Johnson, W. E., "OIL, A Continuous Two-Dimensional Eulerian Hydrodynamic Code," GAMD-5580, AD-477-240, General Atomic Division, General Dynamics, San Diego, CA., June 1965.
3. Farr, J. L., Traci, R. M., "A Users Manual for SAMS (Small Arms Muzzle Simulator)," SAI Report No. SAI-74-514-LA, March 1974.
4. Roache, P. J., "Computational Fluid Dynamics," Hermosa Publishers, Albuquerque, NM, 1972
5. Numerical Methods in Fluid Dynamics, ed. by J. J. Smolderen, AGARD Lecture Series No. 48, May 1972.
6. Noh, W. F., "CEL: Coupled Eulerian-Lagrangian Code," Methods in Computational Physics, Vol. 3, Academic Press, N.Y., 1973.
7. Hirt, C. W. and Amsden, A. A., "An Arbitrary Lagrangian-Eulerian Computing Method for all Flow Speeds," to be published in the Journal of Computational Physics.
8. Gentry, R. A., Martin, R. E., Daly, B. J., "An Eulerian Differencing Method for Unsteady Compressible Flow Problems," Journal of Computational Physics, 1, p. 87, 1966.
9. Harlow, F. H., "Two-Dimensional Hydrodynamic Calculations," LA-2301, Los Alamos Scientific Laboratory, April 1959.
10. Johnson, W. E., "Code Correlation Study," Air Force Weapons Lab. Technical Report, TK-70-144, April 1971.
11. Hageman, L. J. and Walsh, J. M., "HELP, A Multi-Material Eulerian Program for Compressible Fluid and Elastic-Plastic Flows in Two Space Dimensions and Time," Vol. 1, Systems, Sciences and Software, Report 3SR-350, Aug. 1970.



12. Private communication from Dr. Celmins, Chief, Fluid Dynamics Branch, Ballistic Research Laboratory.
13. Leipman and Roshko, Elements of Gas Dynamics, John Wiley & Sons, New York, 1957.
14. Probststein, R. F., "Inviscid Flow in the Stagnation Region of Very Blunt-Nosed Bodies at Hypersonic Flight Speeds," Brown University Report, WADC TN 56-395, September 1956.
15. Schlichting, H., Boundary Layer Theory, translated by J. Kesten, McGraw-Hill Book Co., New York, 1955.

## APPENDIX A

### GEOMETRICAL DESCRIPTION OF PARTIAL CELLS

The numerical technique for treatment of solid boundaries within the Eulerian grid, given above, requires certain geometrical factors which define the partial cells formed by intersections of the boundary curve with the rectangular grid lines. These factors are the fractions of the cell sides open to the flow ( $A_k$ ,  $k = 1, 2, 3, 4$ ), the fraction of the rectangular cell volume ( $F$ ) occupied by fluid and an angle ( $\theta'$ ) defining the local normal to the boundary. The details of the procedure for calculating these factors are given in this appendix. The discussion applies for any fixed boundary, or for a moving boundary defined at any time ( $t$ ) by the locations of a sequence of boundary points.

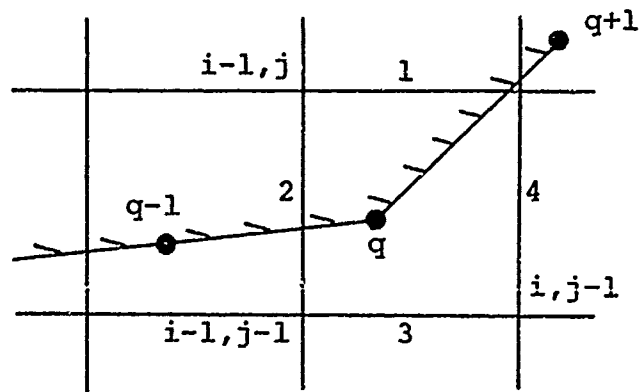


FIGURE A.1. SCHEMATIC OF PARTIAL CELL

A general fixed or moving boundary is described by a string of beads fixed to the boundary and numbered from 1 to  $N$  in ascending order in a counterclockwise fashion. Only one bead is allowed to reside in a fixed Eulerian cell. In the event of more than one bead located in a cell, the leading bead is used to represent the boundary. Hence the density of beads is related directly to the spatial resolution of the numerical solution.

Each cell is defined by the position of the four corners as indicated in Figure A.1. In other words, the coordinates of  $(r_i, z_j)$ ,  $(r_{i-1}, z_j)$ ,  $(r_{i-1}, z_{j-1})$ ,  $(r_i, z_{j-1})$  are known for each cell. The four sides of each cell are labeled 1, 2, 3 and 4 in a counterclockwise manner as also depicted in the figure. The partial cell occupied by bead  $q$  is characterized by five quantities:  $A_1(q)$ ,  $A_2(q)$ ,  $A_3(q)$ ,  $A_4(q)$  which signify the percentage of open area at surface 1, 2, 3 and 4, respectively, and  $F(q)$  representing the percentage of the volume open. For the purpose of this appendix, these quantities are associated with bead  $q$  which resides in the partial cell being considered.

In order to arrive at the above set of quantities, we must have some additional information for each partial cell. The nature of the partial cell is characterized by the two indices that denote the two partially open surfaces. For example, the partial cell occupied by bead  $q$  in Figure A.1 is type 1-2 cell, because surfaces 1 and 2 are partially opened but surfaces 3 and 4 are completely open. Hence  $A_1(q) < 1$ ,  $A_2(q) < 1$  and  $A_3(q) = A_4(q) = 1$  while the percentage of the volume open,  $F(q)$ , is less than unity. One can readily count that there are six types of partial cells: 1-2, 1-3, 1-4, 2-3, 2-4, and 3-4.

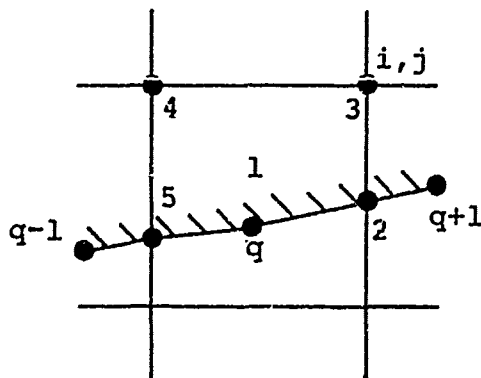


FIGURE A.2. INDEXING OF PARTIAL CELL BOUNDARY POINTS

To evaluate  $A_1(q), \dots, A_4(q), F(q)$ , we must have the coordinates of the five points marked 1, 2, 3, 4, 5 shown in Figure A.2 above. Namely, we must have  $r_1(q), z_1(q), \dots, r_5(q), z_5(q)$ . Point 1 always refers to bead  $q$ , point 2 signifies the intersection of the boundary with the surface denoted by the leading index, point 5 represents the intersection of the boundary with the surface denoted by the trailing index. It should be noted that points 3 and 4 might coincide, depending on the character of the partial cell, for example, in the case of the type 1-2 cell.

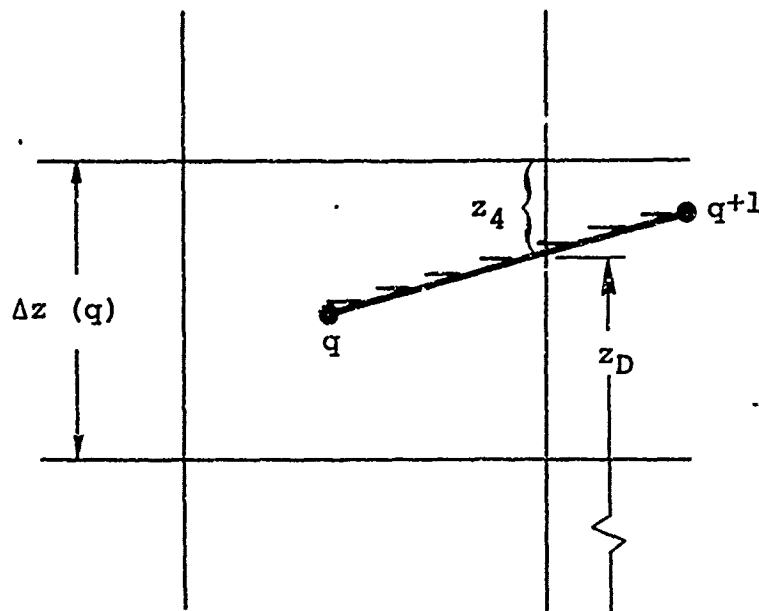


FIGURE A.3. DEFINITION OF CELL INTERSECTION

The procedure for classifying the partial cells at any time,  $t$ , depends on the relative magnitudes of  $i(q+1), j(q+1), i(q)$  and  $j(q)$ . For example, take the following case:  $i(q+1) > i(q), j(q+1) = j(q)$  as shown in Figure A.3.

The line joining beads  $q$  and  $q+1$  is of the form:

$$z = F_z(r; z(q), r(q), z(q+1), r(q+1)) \quad (A.1)$$

where the function  $F_z$  is given by:

$$F_z = \frac{z(q)-z(q+1)}{r(q)-r(q+1)} r + [z(q) - \frac{z(q)-z(q+1)}{r(q)-r(q+1)} r(q)] \quad (A.2)$$

then

$$z_4 = z[j(q)] - z_D \quad (A.3)$$

where

$$z_D = F_z(r[i(q)]; z(q), r(q), z(q+1), r(q+1))$$

and the fractional areas are:

$$A_4(q) = 1 - \frac{z_4}{\Delta z(q)} = A_2(q+1) \quad (A.4)$$

with  $\Delta z(q)$  signifying the size of the cell in the  $z$ -direction. Coordinates of the intersection with the cell side are:

$$r_2(q) = r[i(q)] = r_5(q+1) \quad (A.5)$$

$$z_2(q) = z_D = z_5(q+1)$$

Bead  $q+1$ , and all successive beads, moving counter-clockwise around the boundary, are treated in the same manner. To sum up the computational procedure in graphical form, without the detailed formulae, Table A.1 is presented at the end of this section.

After the preceding treatment has been applied to each bead on the boundary, the leading (first) index for bead  $q$ , as well as the trailing (second) index for the bead  $q+1$  is known. The location of the leading cut for bead  $q$  and the location of the trailing cut for bead  $q+1$  are also known. Each partial cell is assigned two indices, two of the four  $A_k(q)$ 's,  $k = 1, 2, 3, 4$ , and the location of points 1, 2 and 5. In order to complete the description of the partial cell, the remaining two  $A_k(q)$ 's,  $k = 1, 2, 3, 4$  must be obtained, and the fraction of the volume open,  $F(q)$ , must be computed. That is, the locations of points 3 and 4 for each cell must be given. This is done according to Table A.2 at the end of this section.

Once the position of the five key points are found, namely,  $r_1(q), z_1(q) \dots r_5(q), z_5(q)$ , the percentage of the volume open  $F(q)$  can be obtained from the following formula.

$$F(q) = \begin{cases} 1 - f(q) & \text{if } f(q) > 0 \\ -f(q) & \text{if } f(q) < 0 \end{cases}$$

(A.6)

where

$$f(q) = \frac{1}{4} \frac{\sum_{k=1}^5 [z_{k+1}(q) - z_k(q)] [r_{k+1}(q) + r_k(q)]^2}{[r^2(i(q)) - r^2(i(q)-1)] [z(j(q)) - z(j(q)-1)]}$$

The expression  $f(q)$  can easily be obtained by integrating the cylindrical volume enclosed by the five points. To complete the geometrical definition of the partial boundary cells, the direction cosines of the outward directed normal to the solid boundary is defined in the following approximate manner (see Figure A.4).

$$(\sin \theta')_q = \frac{z_2(q) - z_5(q)}{\sqrt{[z_2(q) - z_5(q)]^2 + [r_2(q) - r_5(q)]^2}} \quad (\text{A.7})$$

$$(\cos \theta')_q = \frac{r_5(q) - r_2(q)}{\sqrt{[z_2(q) - z_5(q)]^2 + [r_2(q) - r_5(q)]^2}} \quad (\text{A.8})$$

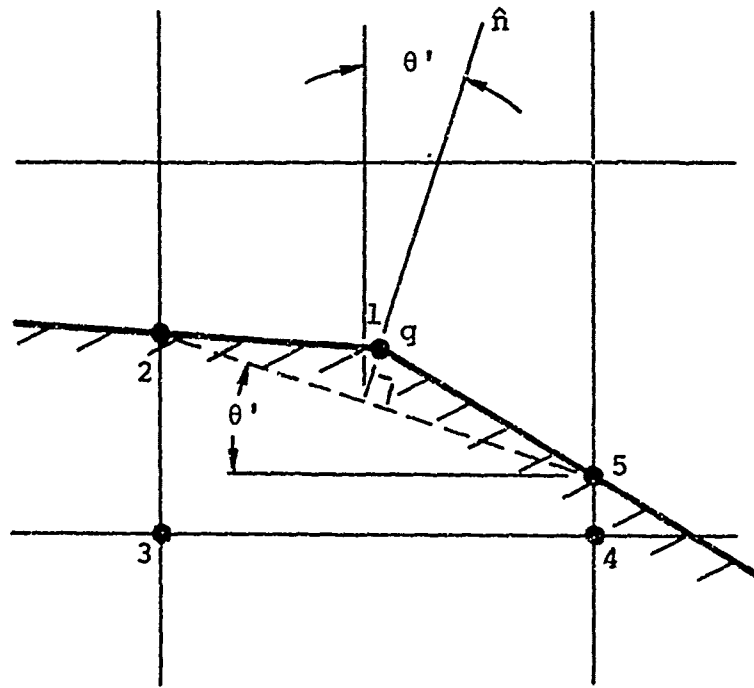


FIGURE A.4. DEFINITION OF NORMAL TO SOLID SURFACE

This completes the definition of all geometrical quantities required for the numerical treatment of partial cells. The scheme is used in computer program SAMS to define the partial cells associated with the fixed muzzle boundaries and the moving projectile boundaries.

		<ul style="list-style-type: none"> <li>● q</li> <li>■ q+1</li> </ul>	1st index of bead q	2nd index of bead q+1	
$i(q+1) > i(q)$	$j(q+1) = j(q)$		4	2	
	$j(q+1) > j(q)$	If $z_4 \geq 0$		4	3
		If $z_4 < 0$		1	2
	$j(q+1) < j(q)$	If $z_4 \leq \Delta z(q)$		4	1
		If $z_4 > \Delta z(q)$		3	2
$i(q+1) < i(q)$	$j(q+1) = j(q)$		2	4	
	$j(q+1) > j(q)$	If $z_2 \geq 0$		2	3
		If $z_2 < 0$		1	4
	$j(q+1) < j(q)$	If $z_2 \leq \Delta z(q)$		2	1
		If $z_2 > \Delta z(q)$		3	4
$i(q+1) = i(q)$	$j(q+1) > j(q)$		1	2	
	$j(q+1) < j(q)$		3	1	

TABLE A.1. DEFINITION OF BOUNDARY INTERSECTIONS WITH CELL SIDES






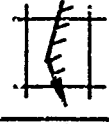








Type 1-2	$j(q+1) > j(q)$	 $A_3=1$ $A_4=1$	$r_3(q) = r(i(q) - 1)$ $z_3(q) = z(j(q))$
	$j(q+1) \leq j(q)$	 $A_3=0$ $A_4=0$	$r_4(q) = r_3(q)$ $z_4(q) = z_3(q)$
Type 1-3	$j(q+1) > j(q)$	 $A_2=0$ $A_4=1$	$r_3(q) = r(i(q) - 1), z_3(q) = z(j(q))$ $r_4(q) = r_3(q), z_4(q) = z(j(q) - 1)$
	$j(q+1) \leq j(q)$	 $A_2=1$ $A_4=0$	$r_3(q) = r(i(q)), z_3(q) = z(j(q) - 1)$ $r_4(q) = r_3(q), z_4(q) = z(j(q))$
Type 1-4	$j(q+1) > j(q)$	 $A_2=0$ $A_3=0$	$r_3(q) = r(i(q))$ $z_3(q) = z(j(q))$
	$j(q+1) \leq j(q)$	 $A_2=1$ $A_3=1$	$r_4(q) = r_3(q)$ $z_4(q) = z_3(q)$
Type 2-3	$i(q+1) < i(q)$	 $A_1=1$ $A_4=1$	$r_3(q) = r(i(q) - 1)$ $z_3(q) = z(j(q) - 1)$
	$i(q+1) \geq i(q)$	 $A_1=0$ $A_4=0$	$r_4(q) = r_3(q)$ $z_4(q) = z_3(q)$
Type 2-4	$i(q+1) < i(q)$	 $A_1=1$ $A_3=0$	$r_3(q) = r(i(q) - 1), z_3(q) = z(j(q) - 1)$ $r_4(q) = r_3(i(q)), z_4(q) = z_3(q)$
	$i(q+1) \geq i(q)$	 $A_1=0$ $A_3=1$	$r_3(q) = r(i(q) - 1), z_3(q) = z(j(q))$ $r_4(q) = r(i(q)), z_4(q) = z_3(q)$
Type 3-4	$i(q+1) > i(q)$	 $A_1=0$ $A_2=0$	$r_3(q) = r(i(q))$ $z_3(q) = z(j(q) - 1)$
	$i(q+1) \leq i(q)$	 $A_1=1$ $A_2=1$	$r_4(q) = r_3(q)$ $z_4(q) = z_3(q)$

TABLE A.2. FINAL DEFINITION OF PARTIAL CELL GEOMETRY

## APPENDIX B

### M-16 MUZZLE FLOW TIME HISTORIES

The present version of the SAMS code requires the specification of the time dependent muzzle flow properties ( $\rho$ ,  $P$ ,  $v$ ) as an inflow boundary condition at some location in the barrel "upstream" of the muzzle device. In the calculations presented above for the M-16 rifle these were determined by curvefits to the calculated results of Dr. Celmins of BRL<sup>1,2</sup>. The curvefits are accurate to  $\pm 5$  percent for  $0 \leq t \leq 100$  microseconds and are given by:

$$V(\text{m/sec}) = 1210 - 110 \times \frac{t}{82} \quad (\text{B.1})$$

$$P(\text{N/m}^2) = (486 - 48.8 \times \frac{t}{87}) \times 10^5 \quad (\text{B.2})$$

$$\rho(\text{kg/m}^3) = 40.95 + 7 \times \frac{t}{75.5} \quad (\text{B.3})$$

where  $t$  is given in microseconds.